

AD622552

DASA-13. 161

CLEARINGHOUSE FOR FEDERAL SCIENTIFIC AND TECHNICAL INFORMATION			
Hardcopy	Microfiche	133	pp
\$ 4.00	\$ 1.00		65
ARCHIVE COPY			

R 375

Technical Report

SHALLOW-BURIED MODEL ARCHES
SUBJECTED TO A TRAVELING-WAVE
LOAD

October 1965

DDC
OCT 18 1965
DDC-IRA E



U. S. NAVAL CIVIL ENGINEERING LABORATORY
Port Hueneme, California

This document is subject to export controls and each transmittal to foreign government or foreign nationals may be made only with prior approval of the U. S. Naval Civil Engineering Laboratory

CONTENTS

	page
INTRODUCTION	1
THEORY	3
EXPERIMENTAL WORK	4
Test Program and Description of Arch Models	4
Instrumentation	11
Test Procedures	11
Introduction	11
Sequence of Events	13
Backfilling and Soils Control	16
RESULTS AND DISCUSSIONS	17
General Observations	17
Uncovered Natural Period Tests	20
Effects of Overburden	20
Covered Natural Period	20
Blast Loading	23
Arch Behavior	23
Deflection	23
Moments and Thrusts	26
Footing Behavior	31
Deflection	31
Velocity and Acceleration	38
Free-Field Motion	38
Tie Rod and Floor Behavior	42
Soil Arching	42
Recapitulation	43
Computer Analysis	43
Computer Program	43
Computer Input	43
Computer Output	46
Theoretical versus Experimental Results	46
Consequences of Observations	51
Deficiencies of Work	51

	page
FINDINGS AND CONCLUSIONS	52
ACKNOWLEDGEMENTS	53
REFERENCES	53
LIST OF SYMBOLS	54
APPENDICES	
A - Body Motion Theory	58
B - Backfill Soil	85
C - Instrumentation	98
D - Oscillograms and Scratch Traces	107

INTRODUCTION

This report describes an experiment on small, shallow-buried arches of sheet steel tested in Operation Snowball under Project 3.4 and correlates the results with a previously derived theory. The prime objective of the work was to check the adequacy of the theory in predicting body motions. Secondary objectives were to measure shock input and shell response.

The investigation was concerned with shelter systems of the type shown in Figure 1, which constitutes the Navy's standard personnel shelter. The project was sponsored by the Defense Atomic Support Agency through the Bureau of Yards and Docks.

Soil-Structure interaction research has been conducted at the Naval Civil Engineering Laboratory (NCEL) over the past several years in an effort to gain information which will provide guides in the design of underground structures. Most of this work, due to the limitations of available equipment, has been on systems subjected to plane-wave loading. Nuclear explosions produce a traveling-wave loading. Such loading may evoke quite a different response in some modes of behavior, including the body motions.



Figure 1. Navy standard shelter.

Acquiring an understanding and a means of analyzing the body motion eventually will permit the achievement of an optimum design where the motion is sufficient to develop arching in the covering soil and yet is small enough to insure against rupturing water seals or damaging equipment and personnel. Obtaining data on the shell behavior will permit an evaluation of the influence of the traveling wave in inducing antisymmetrical mode response. In addition, there is a need for shock-input data to permit the design of proper isolators for equipment and personnel and to determine when such isolators are required. The shock input data, however, is not expected to scale to prototype situations although it should provide an idea of the character of the shock input function.

Data from the Operation Plumbbob structures 3.3 showed that the blastward footings deflected considerably more than the leeward footings.¹ Thus, it appears that a buried arch may undergo both rotational and translational body motions. Subsequent experiments in the NCEL blast simulator have shown that the translational body motion of a buried arch is likely to be the dominant mode of response under both static and plane wave blast loading.^{2,3} These tests also showed that considerable arching is developed in the soil bridge over the structure. Similar tests on buried cylinders (where the deflection of the structure with respect to the soil field was small) showed, by contrast, that very little arching was developed. From the tests in the blast simulator, it became evident that the percentage of surface load transmitted to a buried arch is a function of the footing width. Wide footings reduce the body motion but result in relatively large interface pressures. Narrow footings permit an arch to punch into the soil, thus enabling a large portion of the surface load to be transmitted through the soil bridge across the structure.

Under static loads, arching provides considerable added capacity; however, under dynamic loads there remains a question as to whether or not permitting appreciable relative deflections between the structure and the surrounding soil is desirable. No doubt the shear forces, termed arching, are developed if sufficiently large relative displacements occur. Unfortunately, these same motions permit the soil over the arch to achieve a momentum, and subsequent dissipation of the momentum loads the structure.

Based on these observations, a theory was developed for estimating the magnitude of relative deflection necessary to develop the maximum possible arching and to approximate the maximum percentage of the surface loading which could be carried by arching for a given depth of soil cover. A more elaborate theory of arching for a trapdoor system has been completed, based on the assumption that the soil field acts as an elastic material in compression but is not capable of resisting tensile stress.⁴ The latter work provides curves which show the influence of the various parameters involved.

The trapdoor system is analogous to the buried arch if the span of the structure is taken as the width of the trapdoor and the arch deflection relative to the adjacent soil is taken as the displacement of the trapdoor. The buried arch problem represents the greater difficulty because of the footings which influence deflection.

Footing behavior is in itself a perplexing problem. Only recently has an explanation been offered for surface footings on granular soil reconciling what was previously thought to be conflicting data.⁵ This work illustrates that:

...If, on the surface of a dense sand, a dynamically loaded footing is forced into the sand very rapidly, it will fail in the punching shear mode. A slow rate of settlement of the same footing will cause it to fail in the general shear mode. The peak dynamic load carried by the footing subjected to rapid settlements may be three times the static bearing capacity of the footing, while slow settlements may result in peak dynamic loads of about 1.0 to 1.2 times the static bearing capacity of the same footing.

Even with this step forward in understanding, paradoxes remain. Dynamic footing tests with surcharge pressure⁶ do not appear to behave the same as the footings of buried arches. Further, for buried structures, arching and footing effects are interdependent, thus complicating interpretation of behavior.

In an effort to account for arching and footing action, a theory has been derived for predicting the body motions of a shallow-buried arch. This theory served as the hypothesis for the Project 3.4 experiment. Field tests were chosen as a means of checking the theory rather than attempting to get the required data in a shock tube or similar facility for several reasons

the main ones being: (1) to obtain reliable results, it was desirable to use a larger model than could be accommodated in any existing shock tube, and (2) field testing reduces adverse boundary effects inherent in soil test bins.

Model studies and testing experience led the authors to believe that arches with a minimum span of about 30 inches were desirable to achieve confidence in initial experiments. This is one-tenth the span of the Plumbbob Project 3.3 arches. Limitations of instrumentation and funds dictated that only four models of this size could be included. Eight 12-inch diameter models also were incorporated in the program in an effort to get some idea of the influence of footing width, depth of burial, and the failure load.

In subsequent paragraphs the theory which formed the basis for the experimental plan and the tests is outlined.

THEORY

A theory for predicting the body motions of a thin metal arch of shallow burial is given in Appendix A. The basic assumption of this theory is that a soil-stress wave enveloping the arch is equivalent to an impulse which imparts an initial translational and angular velocity to the structure. It is presumed that there is sufficient load to induce failure planes in the soil. The structure is assumed to undergo purely rigid-body motions insofar as finding the deflection of the footings is concerned. With these and certain other assumptions, the equations are written for the initial angular and translational velocities. Thereafter, the arch and its covering soil are treated as a simple model.

Writing the equation of vertical motion for the model provides the maximum displacements of the two footings which, for long-duration loading, becomes

$$y_{\max} = \frac{\bar{p}r - V_1}{bk_z} + \frac{\dot{y}_0}{e\omega} \pm \frac{r\dot{\theta}_0}{e\omega_\theta} \quad (1)$$

where \bar{p} = average surface side-on overpressure above structure

r = arch radius

V_1 = arching shear

k_z = coefficient of subgrade reaction

b = footing width

\dot{y}_0 = initial translational velocity

$\dot{\theta}_0$ = initial angular velocity

ω = natural translational frequency

ω_θ = natural rotational frequency

e = Napierian constant

and

$$V_1 = (\bar{c} + \bar{k} \bar{p} \tan \phi) (r + d_0)$$

where ϕ = angle of friction of soil

\bar{c} = coefficient of cohesion

\bar{k} = at rest coefficient of lateral earth pressure

\bar{p} = average surface pressure over arch

d_0 = depth of soil cover over crown

The preceding equations show that determination of the footing deflection requires four soil terms, three geometric dimensions, and the surface pressure. The first term on the right-hand side of Equation 1 is the deflection due to static load while the second and third terms represent the deflection due to the initial translational velocity and initial angular velocity. These latter two terms are usually relatively small compared with the deflection from static loading.

For short-duration loads, the solution for the body deflections is much more complex than Equation 1; therefore, the solution was programmed for a digital computer. Preshot predictions were made with this program for the input values given at the bottom of Table I. These input values are close to the actual measured quantities except that the properties of the soil as placed were somewhat different (see Appendix A). Predicted peak values of deflections, velocities, and accelerations also are given in Table I. Peak deflections predicted at the 60-pai overpressure level were just over 1 inch. Little rotation was predicted for the conditions of the 500-ton trial.

It can be concluded from solutions of Equation 1 that, except for the applied load, the arching term, V_1 , and the foundation modulus, k_z , are of dominant importance in governing the body motion of the structure.

As previously mentioned, an equation has been developed elsewhere⁷ for the maximum percentage of the surface load which can be carried by arching for any given depth of soil cover. An approximate relation also is given for the deflection required to develop this arching. Thus, the means are available for judging whether or not deflections are tolerable. For estimating purposes, the shear term could be set to zero and the static deflection component merely taken as the product of the surface pressure times the radius divided by the foundation modulus. Neglecting arching shear would tend to compensate for the angular and translational velocity terms. This could be used as a first-approximation check on deflections from long-duration load experiments.

In the paragraphs that follow, the Operation Snowball Project 3.4 experiment is described and the results are compared with the theory.

EXPERIMENTAL WORK

Test Program and Description of Arch Models

In implementing the objectives of Project 3.4, four 39-inch span and eight 12-inch span buried arches were loaded in the 500-ton high-explosive shot. A plan view of the project is shown in Figure 2. Basic information on the physical dimensions of the arches, the depth of burial, and loading conditions are included in Figure 2 and Table II. A bottom view of one of the four large arches, CA-1 through CA-4, is shown in Figure 3. The four arches had an identical geometry, except that CA-4 had its longitudinal axis normal to a radius from ground zero. The large arches were intended to provide information on the body motion and the response of the shell.

Of the small arches, CA-5, CA-6, and CA-7 were to provide information on the effect of footing width; CA-5, CA-8, and CA-9 were to provide information on the influence of the depth of burial; CA-10, CA-11, and CA-12 were to provide information on the mode of failure of the buried arches.

Table I. Preshot Footing Response Predictions*

Parameter	Overpressure (psi) →	45	60	85
	Pressure Duration → (msec)	118	97	82
Deflection (in.)	Leeward	0.88	1.12	1.50
	Blastward	0.92	1.13	1.50
Velocity (in./sec)	Leeward	36.10	47.44	66.30
	Blastward	36.50	47.81	66.43
Acceleration (g)	Leeward	17.7	23.2	32.9
	Blastward	16.0	22.1	32.5

*For:

Depth of cover over crown	= 6 in.
Arch radius	= 15 in.
Footing width	= 1.20 in.
Footing depth	= 1.92 in.
Soil density	= 110 lb/ft ³
Mass of arch and footing	= 0.46 slug
Foundation modulus	= 300 lb/ft ³
Cohesion	= 0
Angle of internal friction	= 35 degrees
Coefficient of lateral earth pressure	= 0.32
Velocity of stress wave in soil	= 1,300 fps

Footings for the large arches were fabricated from steel angles welded together to form a rectangular box section. These footings were fastened to the arch shell by piano hinges brazed to the footings and riveted to the arch shell. The footings were held apart by rectangular struts sharpened on the bottom to minimize resistance as they were forced into the soil. A sketch of the footings and braces is shown in Figure 4. The end walls, of 1-1/2-inch thick plywood, were designed to act independently of the arch. This was accomplished by mounting the end walls on an internal 4-inch diameter aluminum pipe strut extending the length of the arch as shown in Figure 5. A strip of 8-mil plastic was attached with fabric tape around the semicircular perimeter of the end walls and fastened to the arch to prevent sand from sifting through the 1/4-inch void between the ends of the arch and the end walls.

When the arches were placed, soil was filled to within 1/4 inch of the top of the inside of the footings. A 1/4-inch plywood sheet was laid upon the soil (simulating a floating floor slab) so that the top of the plywood was flush with the top of the footings. The floor acted free of the arch and footings.

The physical arrangement for the small arches was identical to that for the large ones except that the footing for arch CA-7 was solid steel.

Table II. Dimensions of Soil-Arch System

Arch No.	Radius of Arch (in.)	Length of Arch (in.)	Footing Width (in.)	Footing Height (in.)	Thickness of Arch (gage)*	Depth of Burial (Crown) (in.)
CA-1	15	57.6	1.25	1.875	14	6
CA-2	15	57.6	1.25	1.875	14	6
CA-3	15	57.6	1.25	1.875	14	6
CA-4	15	57.6	1.25	1.875	14	6
CA-5	6	24	0.5	0.7	28	6
CA-6	6	24	1.0	0.7	28	6
CA-7	6	24	0.25	0.7	28	6
CA-8	6	24	0.5	0.7	28	9
CA-9	6	24	0.5	0.7	28	4
CA-10	6	24	0.5	0.7	28	6
CA-11	6	24	0.5	0.7	28	8
CA-12	6	24	0.5	0.7	28	6

* 14 gage Birmingham sheet is 0.0785 in. thick; 28 gage Birmingham sheet is 0.0156 in. thick.

Models CA-1 through CA-3 were placed in a sand backfill in an excavation of the shape indicated in Figure 6. The other models were in similar pits. Careful consideration was given to how large the pit should be to avoid deleterious boundary effects. Judgment and experience indicate that the soil within a few footing widths of the footing is of dominant influence in governing the footing deflection relative to the soil field since this is the region of high stress concentration. Since body motions were the main concern, there was no apparent need for a large pit providing one could supply logic to support the tenet that arching across the pit would not be large.

Heuristic reasoning can be advanced to evince the improbability of significant effects from arching across the pit as follows: (1) It has been shown that development of large arching requires sizable relative deformations; (2) the difference in the vertical soil modulus of the sand and the clay are not sufficient to develop relative deformations of the magnitude required for significant arching to occur.

Because of the impedance mismatch between the sand fill and the silty clay of the free field, reflected waves might be expected from the bottom and the back of the pit. These reflections occur within a very short time as compared with the fundamental period of the structure and, therefore, would not have any appreciable effects on the arch velocities or deflections. For the preceding reasons, the size of the pit used was considered quite adequate for purposes of the Project 3.4 experiment.

A description of the soil used, a delineation of its properties, and briefs of the methods employed in the main soil tests are given in Appendix B.

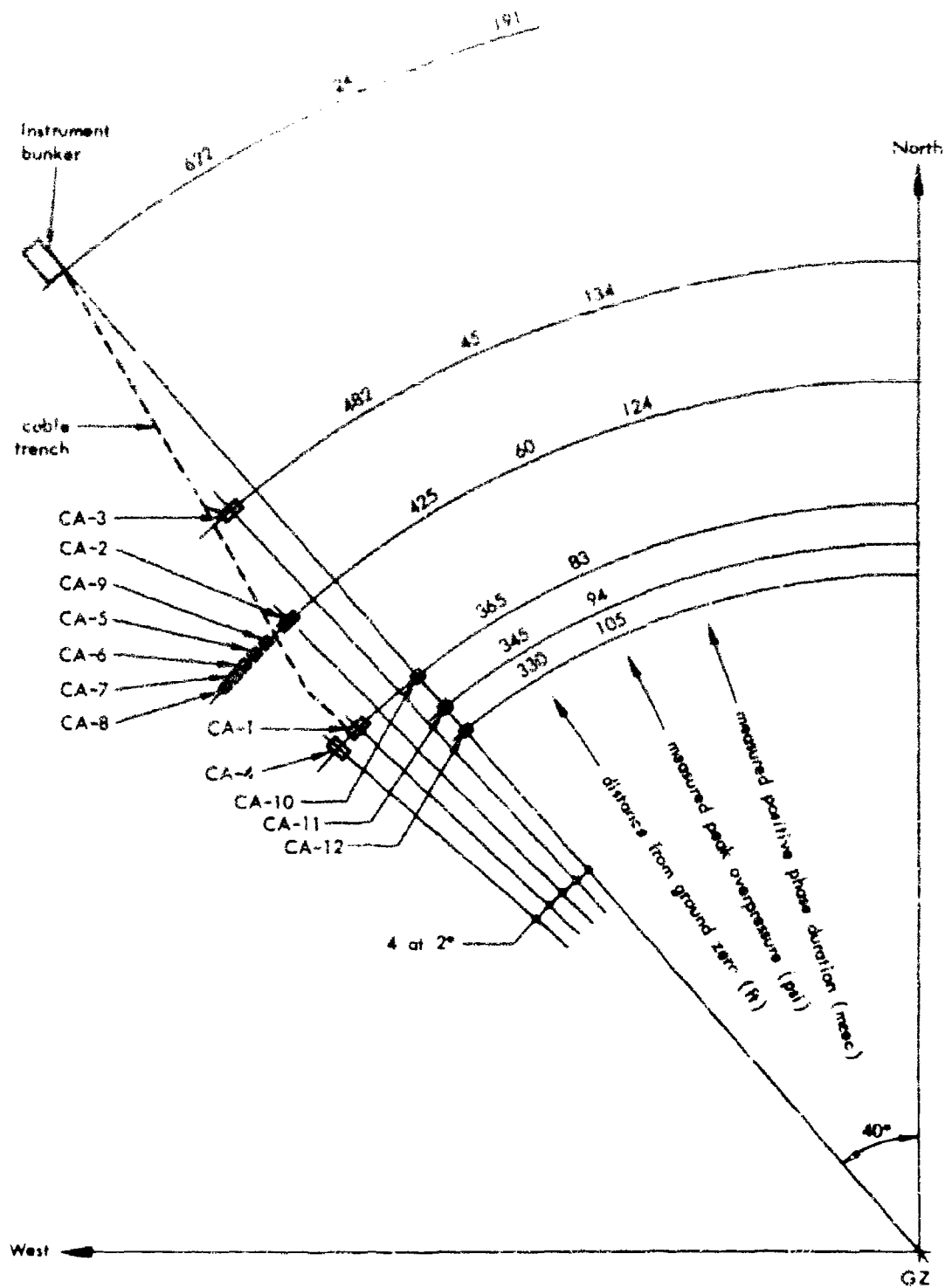


Figure 2. Plan view of Project 3.4.

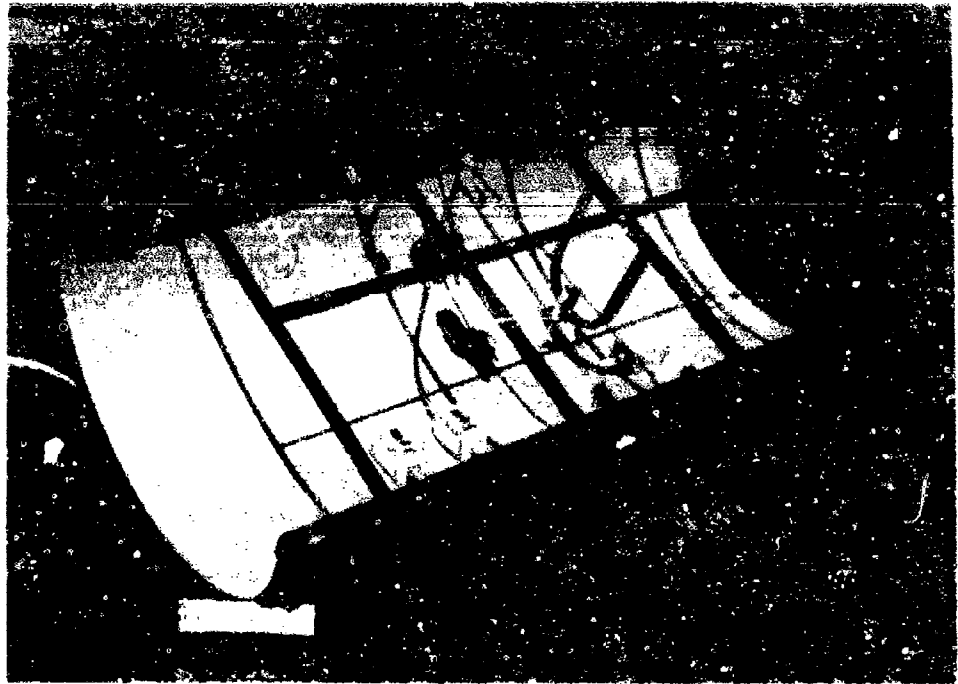


Figure 3. Bottom view of arch.

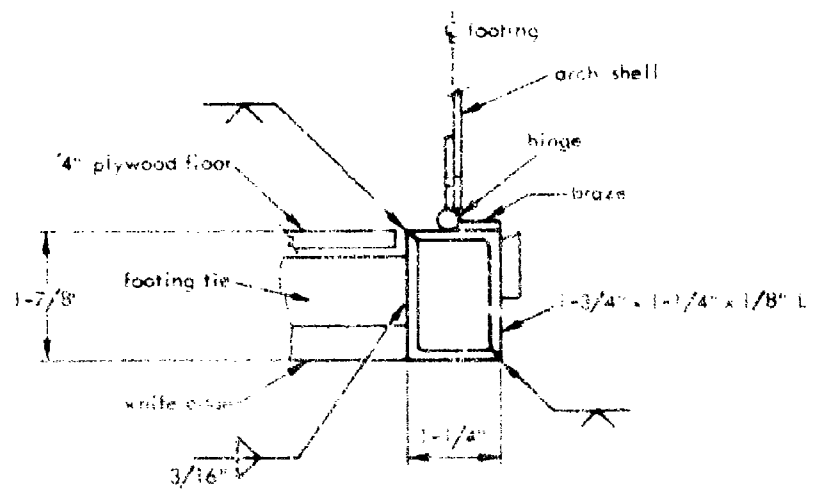


Figure 4. Section through footing.

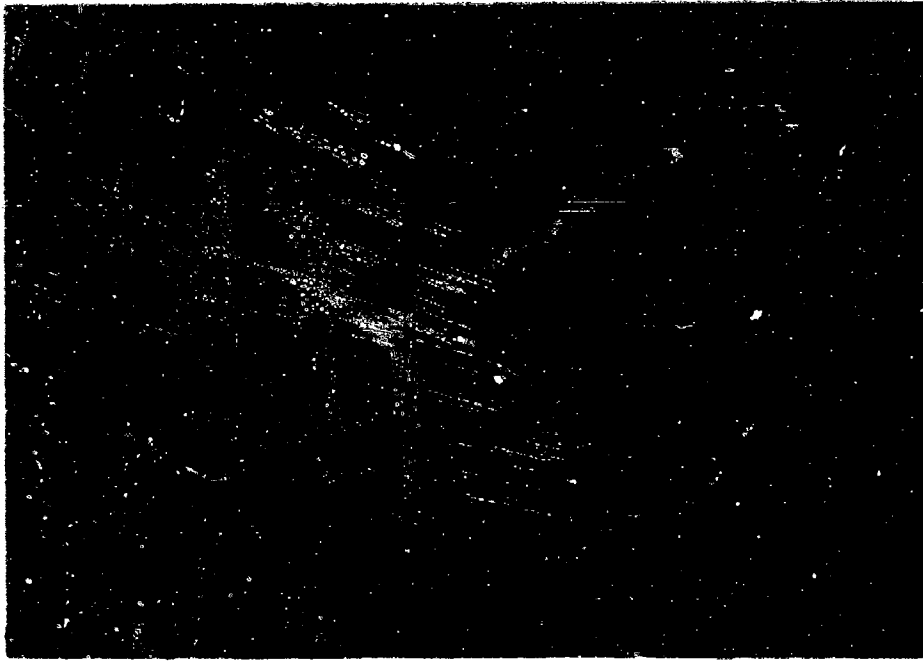


Figure 5. End wall and pipe strut.

There is good reason for using a granular backfill in the model installations as well as in prototype structures. Some of the main reasons are as follows:

1. Large shear strengths can be developed; a lesser portion of the strength is lost with wetting than occurs in cohesive soils.
2. Granular materials can be compacted much more easily and uniformly than cohesive soils.
3. Granular materials provide tremendous strength from passive resistance that is not always available with clays.

Good compaction of backfill soils is exceedingly important in gaining large active and passive pressures at small deflections. This is especially true if moisture is present (as it usually would be in practical situations) introducing an "apparent cohesion" in the soil.

30-mil plastic sheets were placed 2 inches below the surface of the soil to impair the transmission of pore pressure through the soil as indicated in Figure 6. The intent was that only intergranular pressures should be sensed by the arch during the initial period of response to maximum deflection. In prototype arches, the larger depth of soil cover would serve as a filter to the pore pressures. In models, a plastic sheet is needed for this purpose to gain similarity.

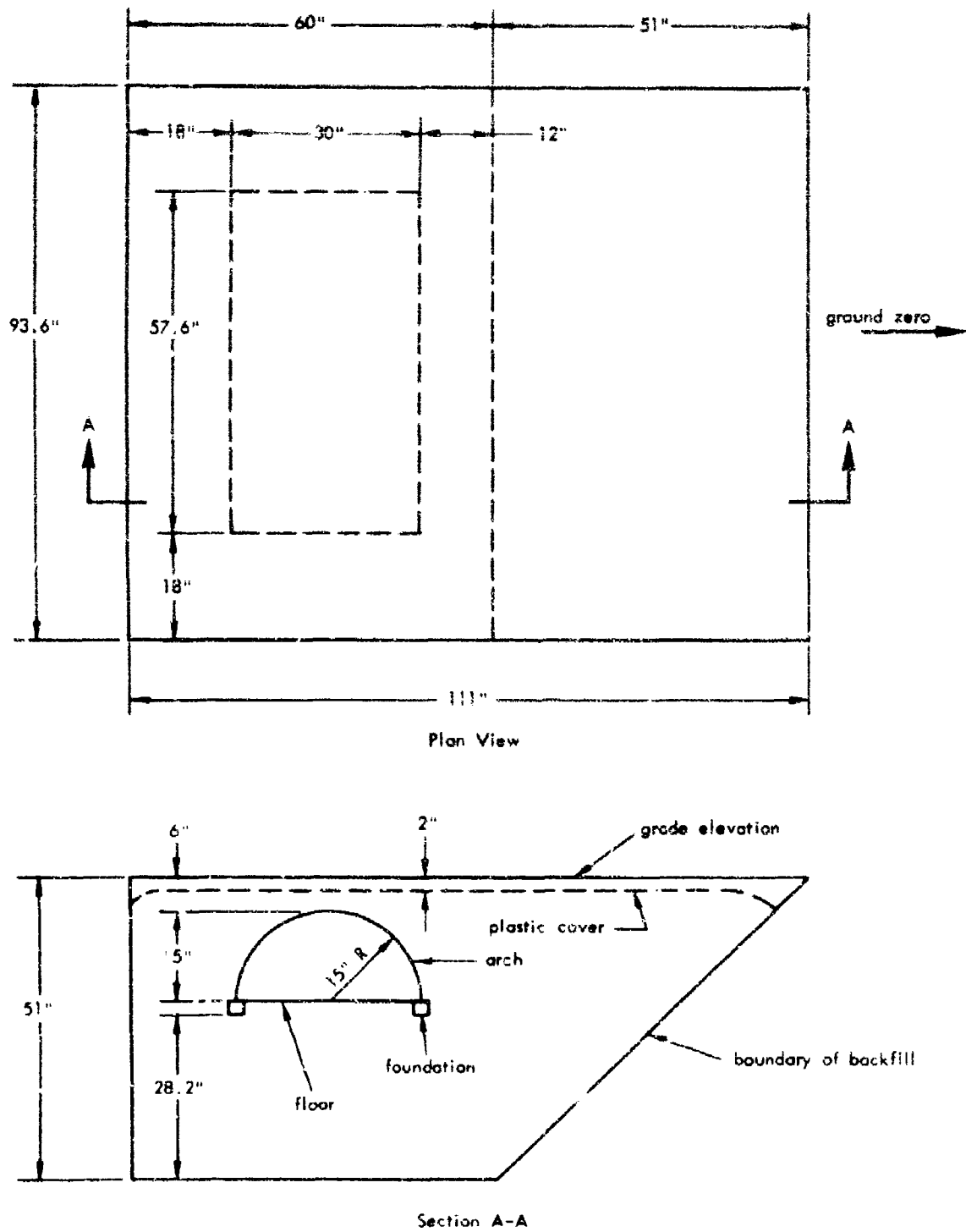


Figure 6. Arch-soil system.

Instrumentation

A total of 36 channels of electronic measurements were made. Twenty-nine of these were on arch CA-2 as indicated in Figure 7. In addition, there were velocity gages on the blastward and leeward footings and a surface pressure gage at each of arches CA-1 and CA-3. The 36th channel was a velocity gage on the southeast corner of the instrument bunker.

Besides the electronic measurements, two plastic scratch boards were employed in each arch to define the maximum deflections of various points on the arch with respect to the footings and the floor. To accomplish this, the plastic scratch boards were placed back-to-back, one being attached to the floor and the other attached to the footings. Scribes for the scratch boards were attached to the shell at 7, 20, 40, 90, 140, 160, and 173 degrees around the large arches and at 7, 90, and 173 degrees on the small arches. Deflections of the arch with respect to the footings were not expected to be sufficiently large to be detectable for the small arches. Three vertical rods, one attached to the crown and one attached to each footing, provided reference points for survey measurements.

The intended purposes of the measurements were as follows:

1. Free-Field Deflections. These measurements were to determine the angle of the soil stress wave front with the horizontal, to define the seismic velocity of the stress wave, and to measure the free-field deflections for comparison with the body motions of the arch.
2. Deflections. Footing deflection measurements were primarily for defining the body motions of the structures. The scratch gages, however, were for determining the maximum displacements of the intrados with respect to the floor and footings. The welding rods were simply a backup for the electronic measurements and were to supply information on maximum deflections even if the electronic measurements were lost. Velocity gages were used in lieu of deflection gages on the footings, because of the inaccessibility of a fixed reference point. The velocities are integrated to obtain deflections. Arch deflection measurements were for determining the predominant mode of vibration and the movement of the arch with respect to the footings.
3. Strains. Strains measured around the arch were used to define the thrust and moment distribution. In addition to permitting definition of stresses, these measurements prove useful in a study of arching. Strains in the tie rod were used to measure the horizontal thrust in the footings.
4. Accelerations. Accelerometers were included primarily for getting some idea of the shock input; however, these records also were integrated for velocity and deflection. Such integrations are not always successful.
5. Surface Pressure. These gages were for defining the loading. All of the electronic gages on the structure were employed in defining the natural periods of vibration of the system.

No electronic instruments were used with the 12-inch diameter models; however, measurements of rotation and relative downward displacements were attempted using a precision level. The models were exhumed after the shot to observe their condition.

A more detailed description of the transducers and electronic instruments employed is given in Appendix C. Further information on the instrumentation setup is given in the Test Procedures Section.

Test Procedures

Introduction. This section summarizes the procedure followed in completing preparations for the tests and the precautionary measures taken to assure adequate control in order to achieve good results.

Sequence of Events. After the locations of the pits were established, a trencher was used to obtain vertical walls along the back and sides. A backhoe was used to scoop out the soil and to form the sloping front wall and the horizontal bottom. The pit was trimmed by hand to the final dimensions (see Figures 6, 8, and 9).

Cable trenches, 4-feet deep, were dug from the bunker to the pits. Thirty-six cables were laid in these trenches plus two extra cables to each instrumented location. The extra cables were included as a safety factor in case of cable failure and also to provide spares for additional use such as the detonation circuit in the covered vibration test.

Elevations for the grade line, plastic sheet, crown of the model, and bottom of the footing were established with respect to a bench mark on the bunker. Four wooden stakes were driven into the bottom of each pit juxtaposed to the side walls, and the elevation markings were established using a surveyor's level.

Since the sand-drop method was used for backfilling the pits with dry sand, densities corresponding to drop height and rate of flow had to be determined before any sand could be placed. The density was determined with a test box using a drop height of 30 inches and a rate of flow corresponding to a full-open valve. The drop height and rate of flow were carefully maintained during backfilling. See Appendix B for a discussion of the method and a description of the equipment and test box.

Work performed in the pits consisted of the following primary steps:

1. Backfilling to the footing elevation.
2. Leveling the sand at the footing elevation.
3. Conducting plate bearing tests to determine the foundation modulus.
4. Preparing the models for placing.
5. Placing the models.
6. Backfilling from the bottom of footing elevation to the floor elevation (4 large 30 inch-diameter models only).
7. Setting scratch gages and completing model assembly.
8. Continuing backfilling to plastic sheet elevation.
9. Placing plastic sheet.
10. Completing backfilling.
11. Measuring the change in crown height with respect to the footing height (change in roundness), using the leveling rods attached to each model, and resetting the rods.

The secondary, more detailed, procedural steps varied with the size of the models and also the amount and type of instrumentation on the models. The following detailed procedure was used for Model CA-2, the arch with the most instruments. After the pit was backfilled to the footing elevation to provide a sand layer of controlled density beneath the arch, the soil was leveled to insure good uniform contact between sand and footing, and four plate bearing tests were conducted to determine the foundation modulus. Figure 9 shows the vertical wooden elevation markers, the horizontal steel rods for leveling the soil surface, and the plate bearing testing device with its frame, dial gage, and weights. The ends of the leveling rods were attached to short vertical angles. A hammer and carpenter's level were used to tap the angles into position and to check the level. Low spots on the sand surface were filled by the sand-drop method, and a special screeder was used to cut away the high spots. Sand was never pushed with the screeder; instead, it was lifted to insure undisturbed density control.

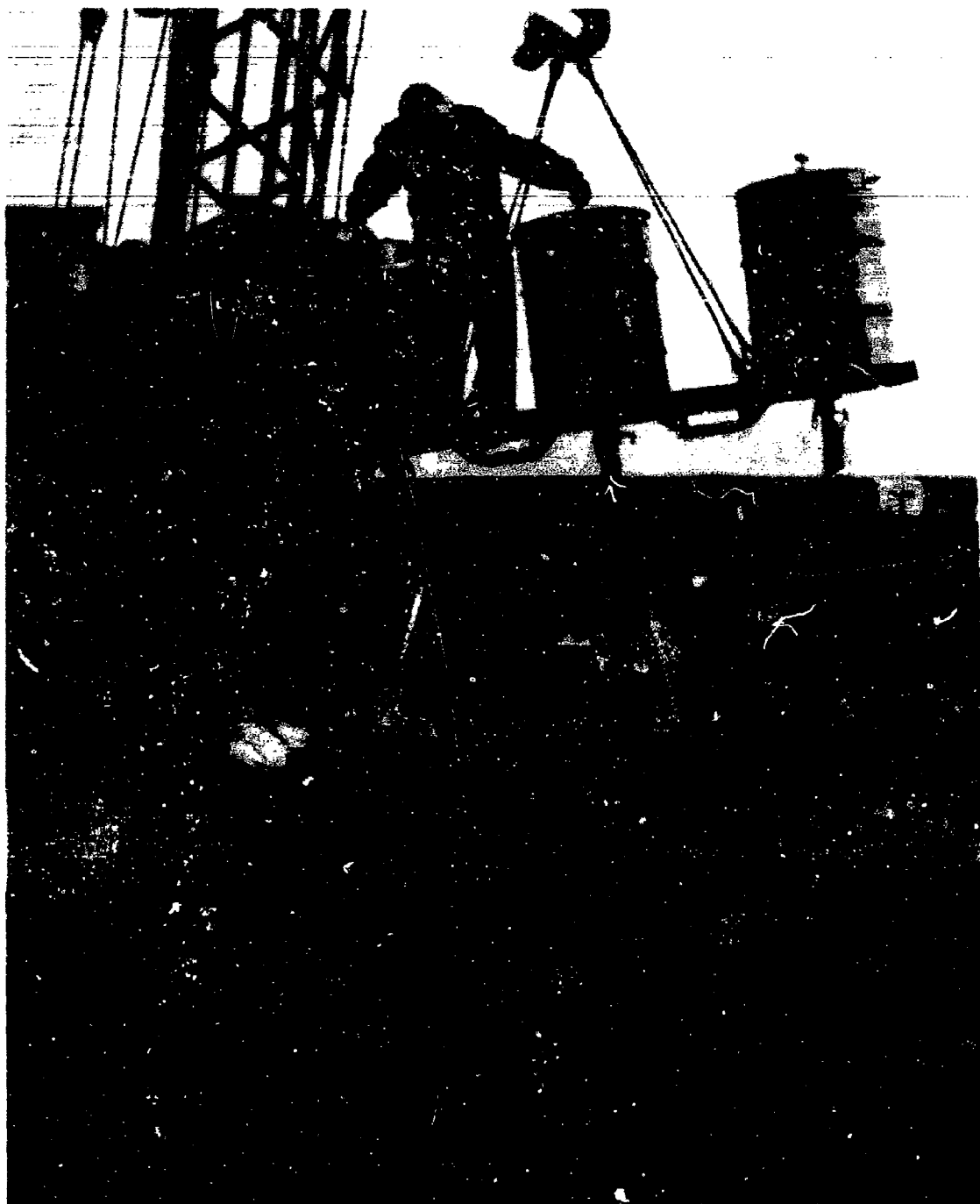


Figure 8. Backfilling equipment.



Figure 9. Device for plate bearing tests and setup for trimming sand.

Next, the arch was prepared for placement. The instruments were installed and calibrated, the initial out-of-roundness of the arch was recorded, and the elevation rods were set level. All recording instruments were checked for correct sign and direction of trace deflections. A series of static loads and impact loads were then applied to recheck the direction and relative magnitudes of the trace deflections and to determine the unburied natural period of the arch. Next, the arch was placed in the pit with the cables disconnected for ease of handling. Backfilling from the footing elevation to the floor elevation was done by hand; then the floor was placed. The scratch gages were set, the cables connected, the instruments checked, a no-load measurement taken, the cannon plugs waterproofed, and the end walls assembled. Eventually, the model was backfilled and a layer of plastic was placed 2 inches below grade as was done with all the models. Last, the effects of the overburden were measured using the electronic instruments and the vertical rods. The rods were adjusted to protrude 2 inches above grade.

Subsequently, a natural period test was performed on the covered arch. The first nonextensional symmetrical mode period was excited by exploding a small charge over arch CA-2. The charge consisted of two 2-gram tetro pellets taped to a blasting cap. A hemispherical mud cap was placed over the upper portion of the charge to direct the shock downward. The assembly was suspended from the apex of a tripod about 10 inches above the soil surface and directly over the center of the arch.

To complete the test, a blasting cap connected to an initiation circuit was detonated while output from the various transducers was recorded on the oscillographic equipment. During this time, all attenuations were decreased by a factor of five over the corresponding settings for the trial.

A postburial, preshot survey was made to measure the elevation of each model (accuracy ± 0.003 ft) with respect to the bench mark on the bunker and the bench mark in the Canadian Sector of the blast range. The elevation of the center rod of each arch was recorded and the rods on each side then were adjusted to the level of the center rod. These measurements were repeated after the blast as backup measurements to determine the permanent translational and rotational body motions. A velocity gage was mounted on the bunker near the bench mark to measure the movement of the bench mark.

Finally, the models were subjected to the 500-ton high explosive shot, a postshot survey was taken, and the models were recovered.

Backfilling and Soil Control. Since the arch response theory (Appendix A) contains several soil parameters to which the maximum deflections are sensitive, it was necessary to maintain close control over the soil parameters in the experiment. For that reason, special sand was procured from Kimmitt Concrete Limited, Medicine Hat, Alberta. Sand with satisfactory gradation was delivered to the blast range at less than 1-percent moisture content and was stored under a plastic sheet to prevent contamination.

Tests were performed to determine the basic properties of the material as subsequently described. These included a special test for density employing a segmented box and plate bearing tests for determining the foundation modulus.

The device shown in Figure 8 was used to backfill all of the pits. It was lifted and positioned by a truck-type crane. The device consisted of a steel frame, three steel barrels, three flexible hoses, and three inverted funnels containing sieves. The sand containers were the steel barrels, open at the top, with orifices and valves at the bottom. The barrels could be used individually, two at a time, or all three simultaneously by placing them in the steel frame. Cables were provided for lifting a barrel singly or for lifting the frame with its 3-barrel load. A flexible hose, 3 feet long, was attached over the orifice on the bottom of each barrel by a fire hose coupling. At the lower end of each hose, there was an inverted sheet metal funnel containing three sieves.

A five-man crew was used during most of the backfilling operation: crane operator, frame rider to operate valves, and three hose handlers to direct the flow of sand. The following procedure was used:

1. The sand was hand shoveled into the barrels with the valves closed. If three barrels were being used, they were mounted on the frame.
2. The crane was used to move the device to a position beside the pit.
3. The rider mounted the frame.
4. The device was lifted about 5 feet.
5. The flexible hoses were attached.
6. The device was positioned over the pit to achieve a drop height of 30 inches. The drop height was measured from the lowermost point on the inverted funnel to the backfill surface.
7. The rider opened the valves and the hose handlers slowly moved the hose and funnels to and fro to direct the flow of sand.
8. The sand flowed from the barrels through the hoses and sieves, out of the inverse funnels, and dropped 30 inches.
9. The sand was built up evenly - the surface kept as level as possible.
10. The drop height was corrected periodically as the sand surface level raised in the pit.

11. The rider regulated the flow with the valves and then closed the valves at the conclusion of the operation
12. The device was moved away from the pit.
13. The flexible hoses were disconnected.
14. The device was lowered.
15. The rider dismounted.
16. The device was returned to the sandpile for loading.

After the pits were backfilled, they were covered with plywood roofs and 6-mil plastic to prevent water and dust contamination.

Subsequent checkout of the instrumentation readied the project for the shot.

RESULTS AND DISCUSSIONS

General Observations

Data obtained during the Project 3.4 experiment was, in general, quite good. It showed that the characteristics of the response of the four large arches were about as expected, although the magnitudes of the various measurements were larger than predicted. The larger models withstood the overpressure, however moderate damage was inflicted on two of them by large, hard clods of clay in the ejecta. These unanticipated clay bombs did not obscure achievement of the prime objectives of the experiment.

The ejecta from the shot deposited a layer of material of varying thickness over the arches which averaged from about 6 inches at the arches furthest from ground zero to about 12 inches at the closest arches. Fortunately, steel rods which projected several inches above the surface were located in the corner of each pit prior to the shot. These rods were relatively easy to find and greatly facilitated postshot recovery of the structures. Immediately after the postshot survey, the structures were exhumed and carefully examined for damage. At this time, the scratch boards and transducers were removed.

Deleterious effects of the ejecta precluded accomplishment of the tertiary objectives of learning something of the influence of footing width and depth of cover. This information was to be obtained from preshot and postshot measurements on the eight small arches. Unfortunately, most of these arches were smashed by the impact of the large clods. The postshot condition of the arches, as observed after being exhumed, is listed in Table III. Postshot views of arches CA-10 and CA-2, illustrating typical damage, are shown in Figures 10 and 11. Ironically, the arch which had the least damage was CA-13, the one closest to ground zero and subjected to the highest overpressure. Examination of the surface showed that no large clods fell immediately above this structure.

As indicated in Table III, the large arches were not grossly damaged. From the nature of the dents in the arches, there is no doubt they were due to the ejecta. The multiple pounding by the large clods is clearly observable on the oscillograms starting at about 7 seconds from detonation zero. This pounding left some of the scratch gage records complexly scribbled, although the complete motion is clearly defined on many of the scratch boards.

Direct monetary loss from the destruction of the smaller models was small since they were cheap to build, inexpensive to install, and involved no costly instrumentation. The loss of time was more serious; it may be several years before another shot or a suitable simulator is available for duplicating these tests.

Fortunately, all electronic equipment performed well during the trial and records were obtained for all transducers as shown in the oscillograms, Figures D-1 through D-13 of Appendix D. All transducers functioned properly except the velocity gage on the bunker and two of the surface pressure gages. Backup self-recording pressure gages provided the needed data; consequently, malfunction of the two electronic pressure gages did not result in loss of required data. Time of arrival of the surface pressure wave and duration of this wave were obtainable from the pressure records. All other electronic instrumentation functioned properly.

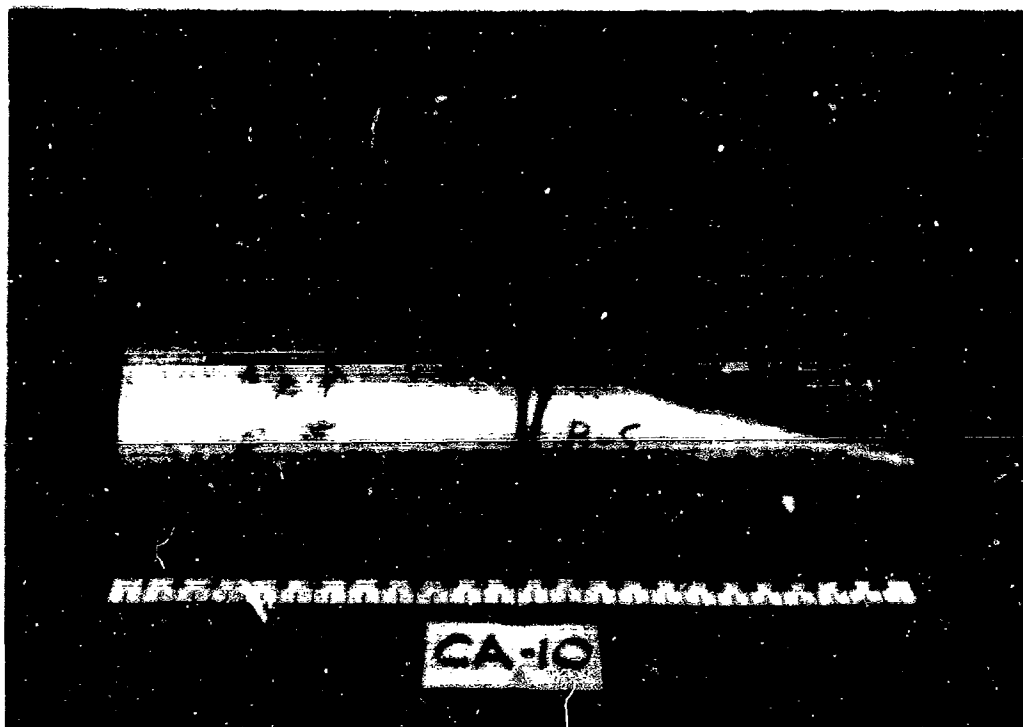


Figure 10. Postshot view of arch CA-10.

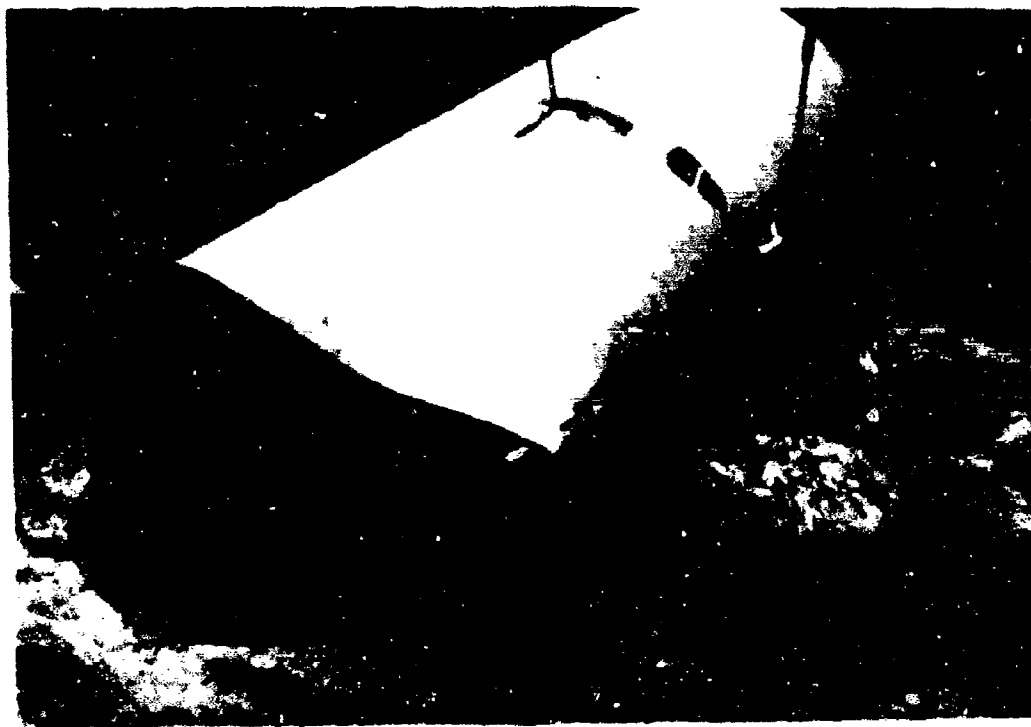


Figure 11. Postshot view of arch CA-2.

Table III. Postshot Condition of Arches

Arch No.	Postshot Condition
CA-1	The right end (facing the arch from the blast side) was dished downward 2-1/2 inches; the left end was dished downward 5/8 inches; the center of the crown was resting on the plastic scratch boards, and the plastic had pushed down the floor.
CA-2	The right end (facing the arch from the blast side) was dished in along the back (lee) side about 4 inches. This damage extended about 10 inches from the end of the arch. Otherwise, the model was in good condition.
CA-3	Good condition; permanent displacement of the crown at the ends was 5/16 and 3/16 inch.
CA-4	Both ends were dished downward; the leeward end was worse than the blastward end; the center of the arch contacted the plastic scratch boards but did not break them.
CA-5	Fairly good condition; crimped slightly in on the blastward side and out on the leeward side near the spring line.
CA-6	One end was in good condition, the other end buckled completely with the end down around the pipe.
CA-7	Flattened.
CA-8	Flattened.
CA-9	Both ends were bent down; the center was held up by the plastic scratch boards.
CA-10	One end was buckled down, the center was resting on the plastic scratch boards, and the other end was in good condition.
CA-11	The leeward side of one end was caved in; the remainder of the arch was in good condition.
CA-12	Good condition; evidence showed that the crown at the center of the arch had struck the plastic scratch boards; the scratch boards were broken.

The records yielded a surprising amount of data including information on ground motion and ejecta. Though not necessarily intended as such, the arches were good ground motion and ejecta sensors. For example, the records clearly show the arrival of a secondary ground wave 200 milliseconds after the arrival of the air blast at the 425-foot distance from ground zero. This wave also was found on the Project 3.6 records of the Waterways Experiment Station. Later in time on the NCEL records, about 7 seconds after arrival of the blast, the large chunks of ejecta impacted on the surface above the buried arches and produced considerable excitation of the various gages. Some of these missiles were quite massive and, judging from the time from blast to impact, must have been thrown to heights upwards of 200 feet.

As a word of caution, it should not be assumed that the behavior of the small arches is representative of what would happen to a prototype at the same overpressure under a nuclear loading. In so extending the results, modeling effects must be taken into consideration.

In this regard, one inescapable deduction from the records is that high-explosive tests are a poor substitute for a large nuclear detonation in conducting soil-structure interaction experiments. Even with the small models employed, the overpressure had decayed to less than one-half of its peak value prior to occurrence of the peak deflection of the arch. A long-duration loading would vastly simplify the comparison of the data with theory and the formation of valid judgments regarding the real problem of concern, namely, providing shelters capable of resisting nuclear weapons effects.

Uncovered Natural Period Tests

When excited, an arch tends to vibrate in the modes indicated in Table IV. Records from tests of striking or pushing and releasing arch CA-2 gave the periods indicated in Table V. Also included are theoretical values of the periods as determined from the equation

$$\omega_n = \frac{2\pi}{T_n} = \frac{C_n}{r^2} \sqrt{\frac{EI}{\gamma}} \quad (2)$$

in which C_n equals a constant corresponding to the various mode shapes as follows:

C_1 (extensional mode)	= 13.7
C_2 (first symmetrical inextensional mode)	= 8.1
C_3 (first antisymmetrical inextensional mode)	= 2.2

and ω_n = natural frequency of mode n (cycles/second)

T_n = natural period of vibration of mode n (seconds/cycle)

r = arch radius (in.)

EI = flexural stiffness of arch (lb-in.²)

γ = mass per unit of arc length (lb-sec²/in.²)

As may be seen in Table V, the experimental values of the period were reasonably close to the computed values in both cases.

Effects of Overburden

Initially, all of the arches were out-of-round to some degree; in most cases, the radius at the crown was less than the design radius. Initial out-of-roundness of arches CA-1, CA-2, and CA-3 is shown in Figure 12. When the overburden was placed, the crowns of eleven of the twelve arches moved upward, thus improving the roundness of the arches. The maximum rise of the crown on any of the arches was 3/32 inch (for arch CA-2, this upward deflection was 0.02 inch).

Moments and thrusts introduced on backfilling were negligibly small.

Covered Natural Period

Detonation of the small charge over arch CA-2 induced vibration with a fundamental period of 19.8 milliseconds. This is appreciably less than the 45-millisecond uncovered period (Table V) which indicates that the stiffening effect of the soil has much more influence on the natural period than the added mass of soil over the structure. This behavior has been observed in other experiments³ and has been explained in a theoretical study.⁷

Table IV. Deflection Modes of an Arch






I. Extensional Mode	
Sometimes called compression mode	
II. Inextensional Modes	
A. Symmetrical	
1. 1st symmetrical (bending - compression)	
2. 2nd symmetrical (bending - compression)	
B. Antisymmetrical	
1. 1st antisymmetrical (lateral bending mode, flexural mode, deflection mode)	
2. 2nd antisymmetrical	

Table V. Natural Periods of Uncovered Arch CA-2

	Natural Period of Uncovered Arch (msec/cycle)	
	Computed	Experimental
T_1 (extensional mode)	22.5	-
T_2 (first inextensional symmetrical mode)	38.1	45
T_3 (first inextensional antisymmetrical mode)	140	126

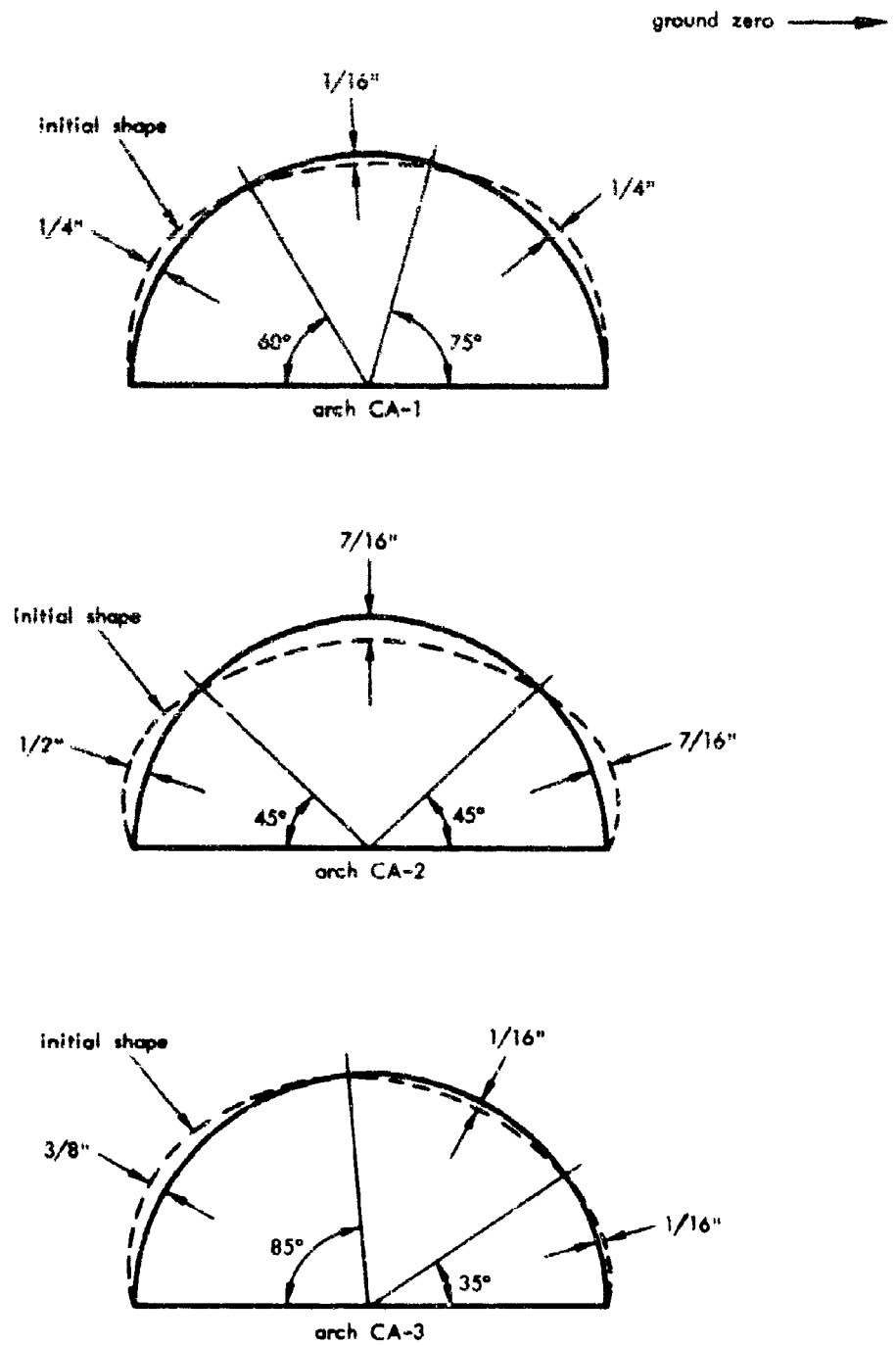


Figure 12. Initial out-of-roundness of the arches.

Blast Loading

Measured peak pressures were almost exactly the same as those predicted (see Table VI). Positive phase durations, by contrast, were 40 percent longer than predicted. The pressure data, for the most part, was taken from the Ballistics Research Laboratory (BRL) self-recording pressure gage. At the location of model CA-1, the positive-phase duration measured by the Wiancko pressure gage was used because the BRL self-recording gage at this location failed part way through the loading history. Arrival times at all locations were determined from the Wiancko gages. The peak pressures from the Wiancko gages were not used because of failure of two of them to respond to the initial pressure spike; apparently dust was entrapped in the orifice holes of these gages. Blast-line data was used to confirm the pressure-time information. The shape of the pressure pulse differed markedly from the theoretical (Friedlander) exponential decay corresponding to the measured peak pressures and durations in that the impulse and, thus, the effective triangular load, was much smaller. This characteristic is apparent in the pressure-time plots of Figures 13 through 15.

Arch Behavior

Deflection. The motions of the structures were greater than predicted. Relative deflections of various points around the perimeter of arch CA-2 at 10, 20, 30, and 43 milliseconds are indicated in Figure 16 together with the residual deflections at 2 seconds. As may be seen, the first antisymmetrical mode deformations were small as compared to the first symmetrical mode deformations. Although the curves are based upon only three electronic measurements, the shape is known to be correct. The shape was determined from the moment diagram and from the scratch gage records. It should be kept in mind that the deflections indicated in Figure 16 were relative to the footings of the structure.

Deflection versus time data for the three gaged points on the perimeter of the structure are shown in Figure 17. The peak deflection at the sides occurred at the time equal to the buried natural period of the structure. Peak deflection at the crown occurred at 26 milliseconds, a time slightly longer than the 19.8 millisecond period. The maximum deflection of the crown with respect to the footing for arch CA-2 was 1.2 inches or about 10 percent of the radius. Significantly, the residual deflection at the crown was less than 1/10 inch.

Considerable insight into the deflection behavior of the arches is derivable from the scratch board traces, Figures D-14 through D-21 of Appendix D. In interpreting these records, it should be pointed out that the plastic scratch boards sheared off at the east footing of arch CA-4 and at the blastward footing of arch CA-1. These failures probably were caused by the crown striking the plastic sheet on its downward excursion. The scratch gage traces were used primarily for checking the deflections determined by other means.

Table VI. Blast Load Parameters

Arch	Range (ft)	Measured or Predicted	Peak Overpressure (psi)		Load Duration (msec)		Impulse* (psi-msec)
			Maximum Value	Effective*	Actual	Effective*	
CA-1	365	Measured	96.7	83	149**	30	1,211
		Predicted	85	-	82	-	-
CA-2	425	Measured	63.1	60	124	39	1,148
		Predicted	60	-	97	-	-
CA-3	428	Measured	50.0	45	134	45	1,005
		Predicted	45	-	118	-	-

*Effective peak overpressure and effective load duration are those values obtained by using an equivalent triangular decaying load, with equal impulse, when the impulse is taken to the time of maximum footing deflection.

**This measurement was taken from Wiancko pressure gage; all other durations are from BRL self-recording gages.

Table VII. Strains in Arch CA-2

Strain Gage			Strain ($\mu\text{in.}/\text{in.}$)				Peak Strain ($\mu\text{in.}/\text{in.}$)	Time to Peak Strain (msec)
Number	Position		At 10 msec	At 20 msec	At 30 msec	At 43 msec		
	Degrees	Inside or Outside						
SG1	7	Outside	+390	+425	+305	+245	+445	21
SG2	7	Inside	-640	-690	-480	-360	-705	21
SG3	20	Outside	+230	+315	+375	+360	+380	31
SG4	20	Inside	-560	-475	-455	-435	-585	7
SG5	40	Outside	+45	+575	+715	+660	+720	31
SG6	40	Inside	-365	-790	-820	-775	-830	26
SG7	90	Outside	-345	+1,740	+820	+670	+1,890	16
SG8	90	Inside	+60	+1,540	+1,150	+1,230	+1,540	21
SG9	105	Outside	-465	-1,080	-1,270	-1,190	-1,290	25
SG10	105	Inside	+215	+1,610	+1,590	+1,460	+1,630	28
SG11	130	Outside	0	+805	+890	+815	+930	28
SG12	130	Inside	-215	-890	-940	-820	-1,000	26
SG13	165	Outside	+225	+645	+780	+790	+815	36
SG14	165	Inside	-695	-875	-970	-825	-1,000	23
SG15	173	Outside	+230	+520	+565	+465	+665	21
SG16	173	Inside	-615	-775	-785	-605	-1,380	8
SG17	---	Brace	+55	-325	-265	-155	-395	19

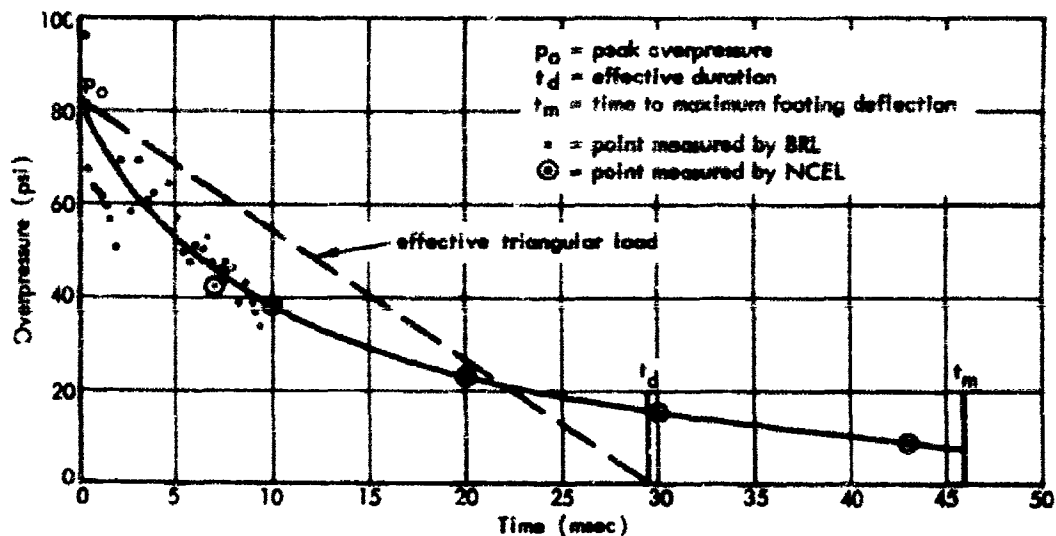


Figure 13. Load-time diagram, arch CA-1.

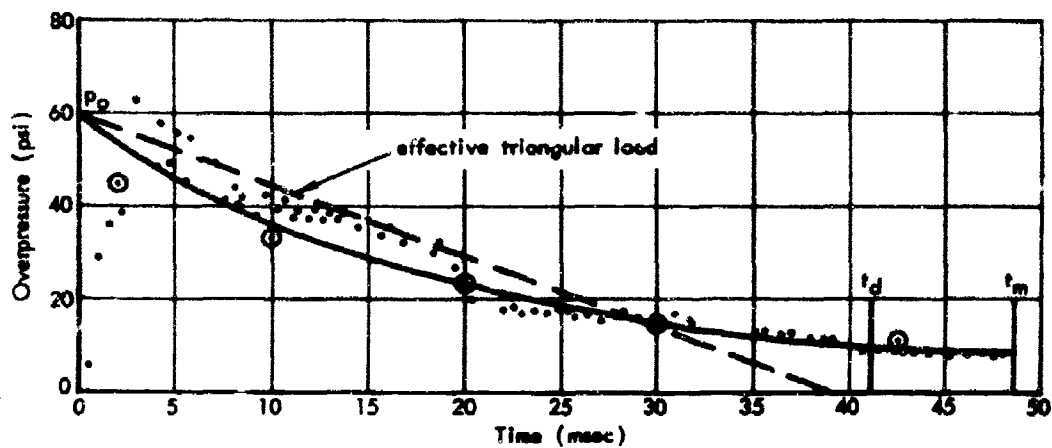


Figure 14. Load-time diagram, arch CA-2.

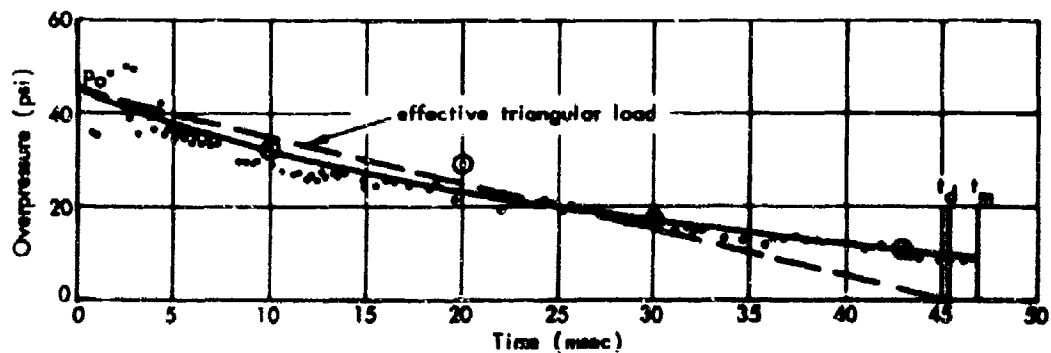


Figure 15. Load-time diagram, arch CA-3.

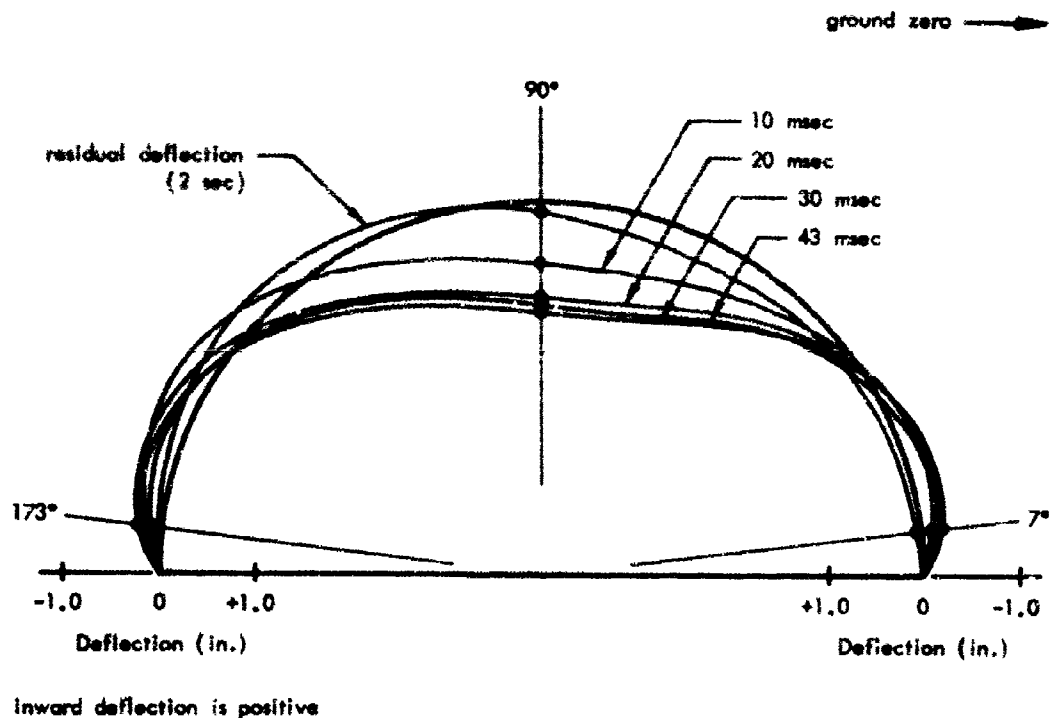


Figure 16. Deflection diagram, arch CA-2.

Moments and Thrusts. Moments and thrusts were determined from the strains given in Table VII. Strain data in general was good, although there was some extraneous strain near the crown imparted by the rotation of the vertical rod employed for determining deflections with the preshot and postshot survey measurements. The rod introduced a moment which influenced the strains within a region of ± 15 degrees of the crown. As a consequence, it was necessary to exercise considerable judgment in interpreting the strain data for determinations of the thrusts and the moments at the crown. Up to 10 milliseconds in time, there was little adverse influence of the vertical rod at the crown. At this and later times, effects of the vertical rod were evident, although the moment was predominantly that corresponding to the first inextensional symmetrical mode of deformation.

A second influence which should be considered in interpreting the data is the accuracy of the moments and thrusts, depending upon whether they were determined from a sum or difference of the strain data. In cases where the magnitudes of the strains are large and the thrust or moment depends on the difference of the strain data, much of the accuracy is lost.

Spatial distribution of moments in arch CA-2, at various times, is given in Figures 18 through 22. Moment distribution differed from that in thinner arches previously tested in the blast simulator.^{2, 3} In the latter arches, the moment distribution was much more irregular and exhibited a large moment about 5 degrees from the spring line. No such behavior was discernible in the Project 3.4 structures.

Moments on the leeward side of arch CA-2 were about 30 percent larger than those on the blastward side at all times. Typical moment-time curves at various points on the perimeter are shown in Figure 23. From this it may be seen that maximum moment at different points occurred at different times. Moment variation was much more irregular than variation in the thrust.

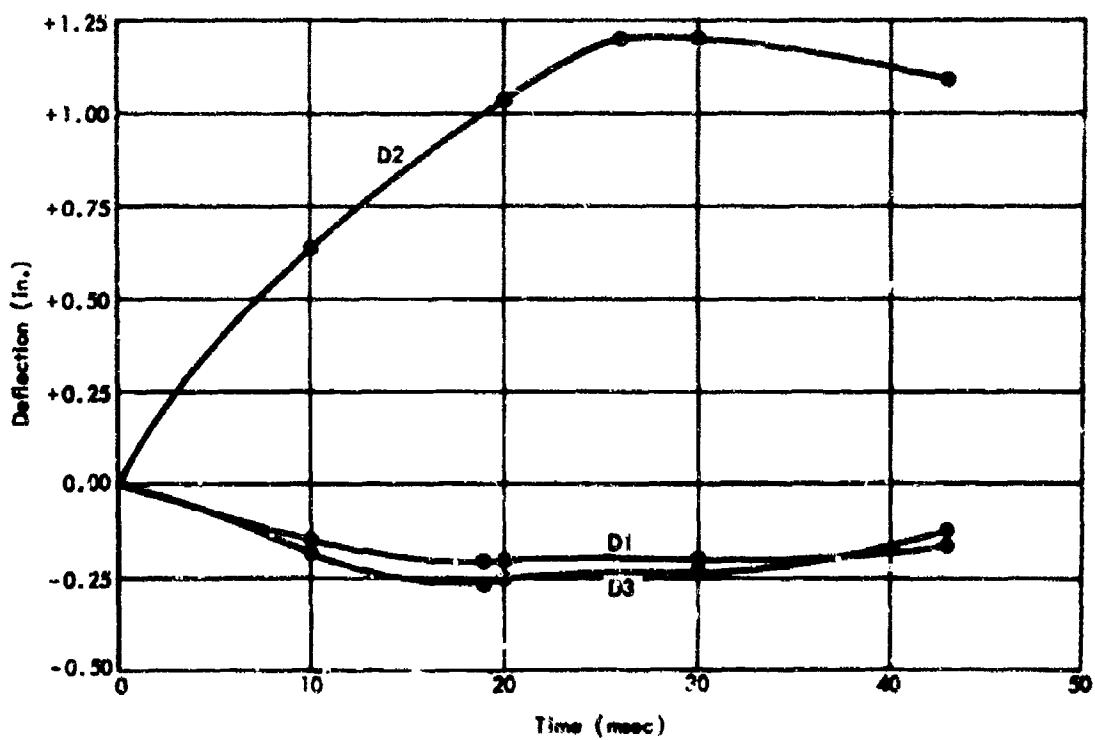
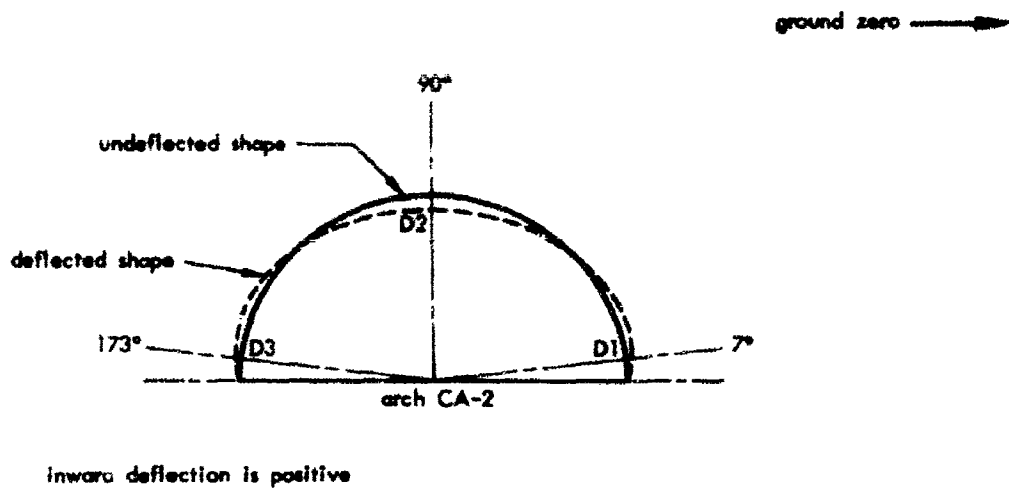


Figure 17. Deflection versus time, arch CA-2.

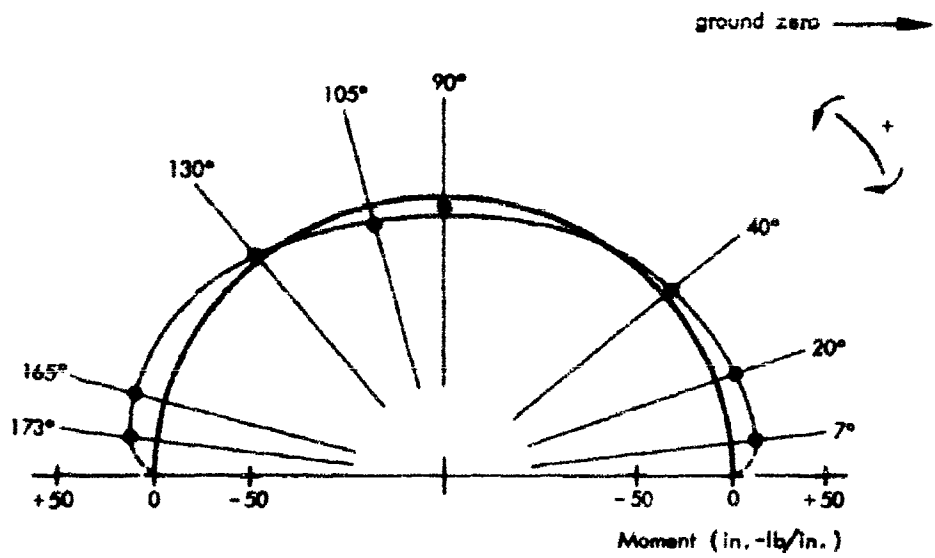


Figure 18. Moment diagram at 10 milliseconds, arch CA-2.

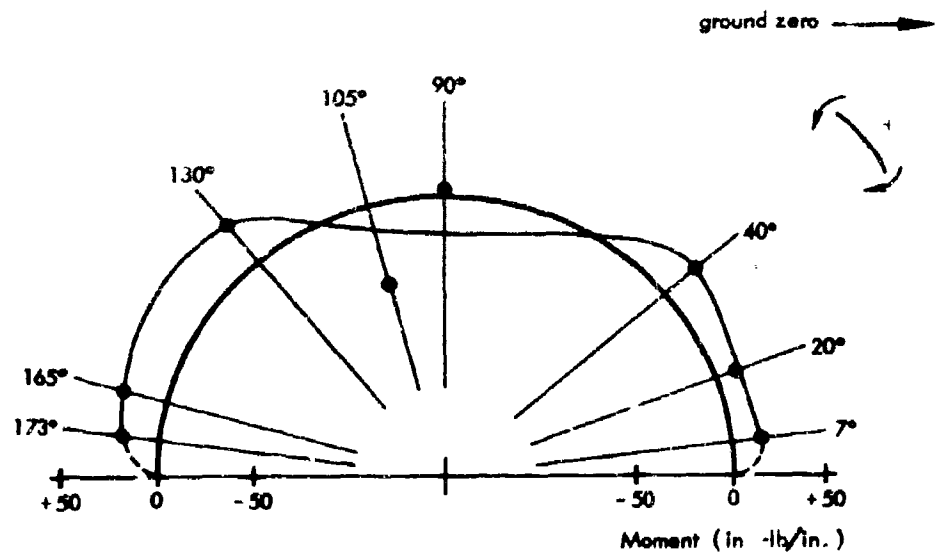


Figure 19. Moment diagram at 20 milliseconds, arch CA-2.

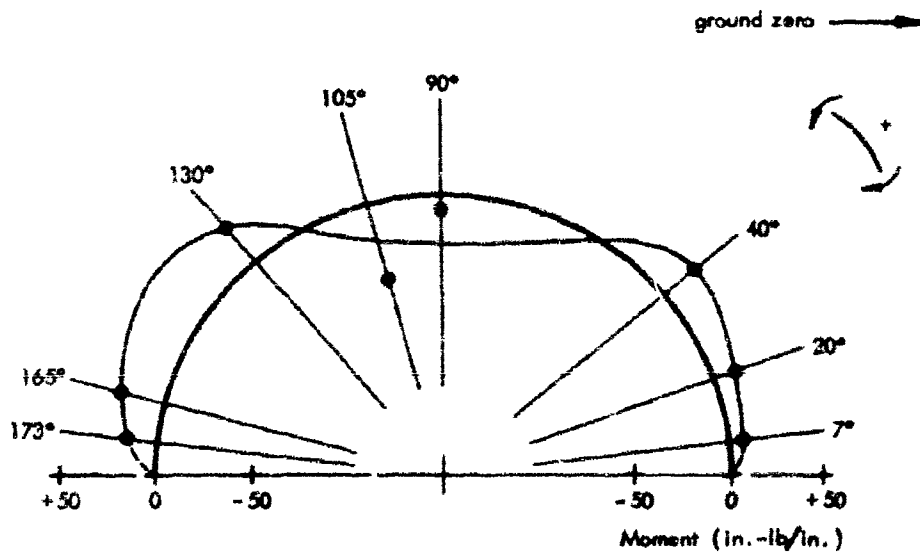


Figure 20. Moment diagram at 30 milliseconds, arch CA-2.

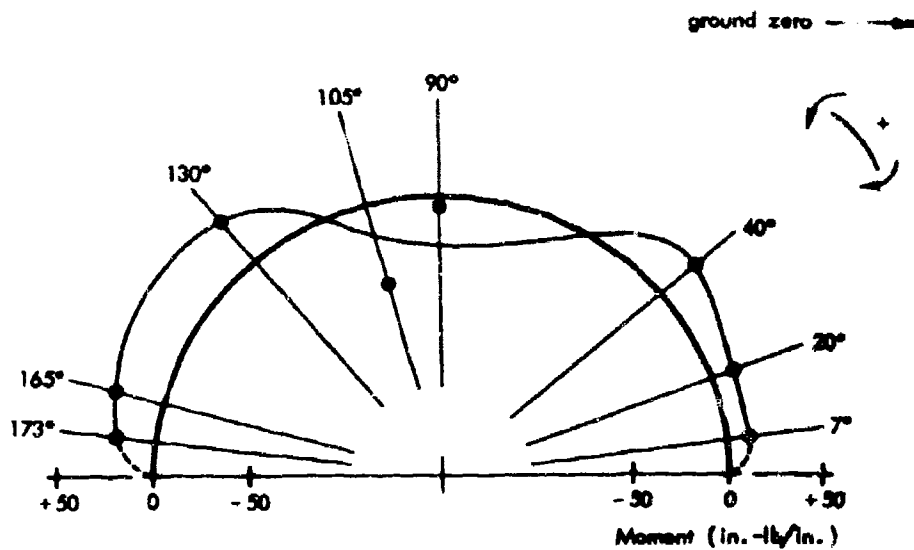


Figure 21. Moment diagram at 43 milliseconds, arch CA-2.

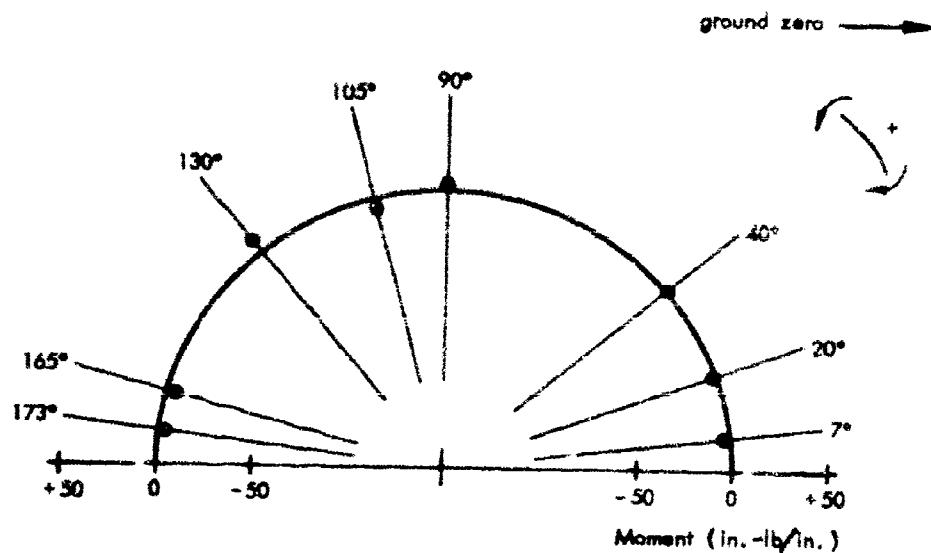


Figure 22. Residual moment diagram at 2 seconds, arch CA-2.

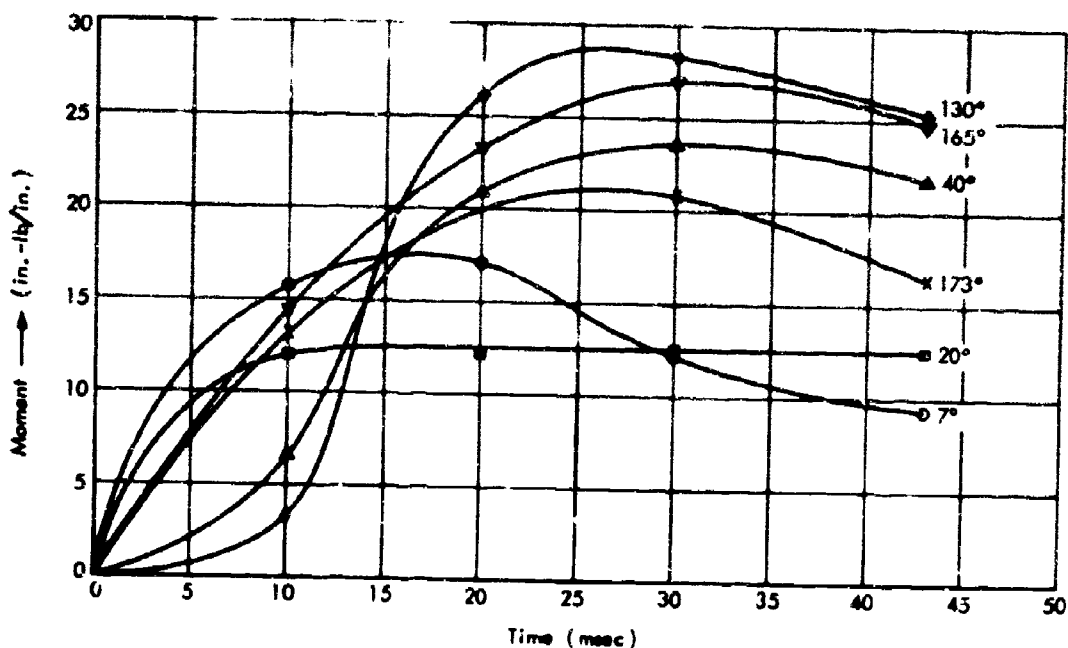


Figure 23. Moment versus time for positions around arch CA-2.

Spatial distribution of the thrust around the perimeter of the arch was fairly uniform at all times, as may be seen from the plots of Figures 24 through 28. At all stations and at all times, the thrust was appreciably less than the product of the surface pressure times the radius, the thrust under hydrostatic load conditions. Variation of the thrusts with time, at various stations around the arch, may be seen in Figure 29. At the 20- and 40-degree stations, the peak thrust was reached in about 10 milliseconds; at the 7-degree station, the peak thrust was reached at approximately 17 milliseconds. Residual thrusts were essentially zero at all stations.

Footing Behavior

Deflection. Absolute displacement of the footings was obtained from integration of the velocity traces. Deflection versus time curves from these data are presented in Figures 30 through 35.

Peak footing deflections in all cases occurred between 42 and 48 milliseconds; maximum values are given in Table VIII. It should be noted that, at the time of maximum footing deflection, the surface pressure had decayed to about one-tenth of peak value; thus, the deflections were much smaller than would have been induced by a megaton nuclear weapon. Absolute displacements of the two points for which measurements were made in the free field also are given in Table VIII. The peak absolute displacement of the free field at the elevation of the footings was 0.682 inch. The relative displacement of the footing of arch CA-2, with respect to a point in the free field at the same elevation, was 0.91 inch.

A check on the reasonableness of the deflections from the velocity gages is obtainable from the scratch gages; the scratch gage traces are given in Appendix D. Scratch traces nearest the footings showed a maximum displacement of the footing with respect to the floor of 1.00 inch. Motion of the floor, as determined from the corrected double integration of the floor acceleration, was 0.62 inch. The sum of these quantities is 1.62 inches, almost exactly the same deflection obtained from integration of the velocity trace.

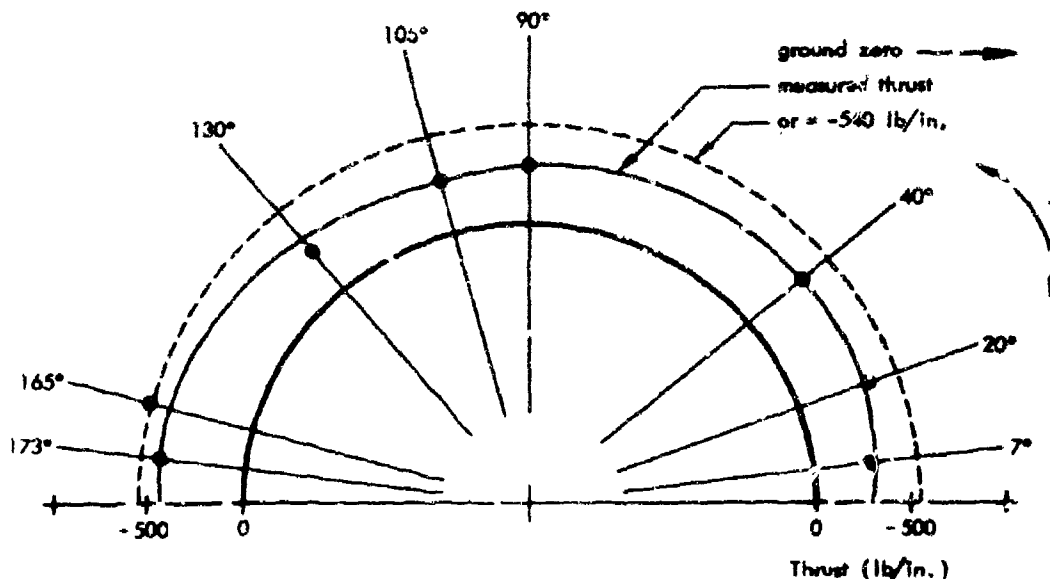


Figure 24. Thrust diagram at 10 milliseconds, arch CA-2.

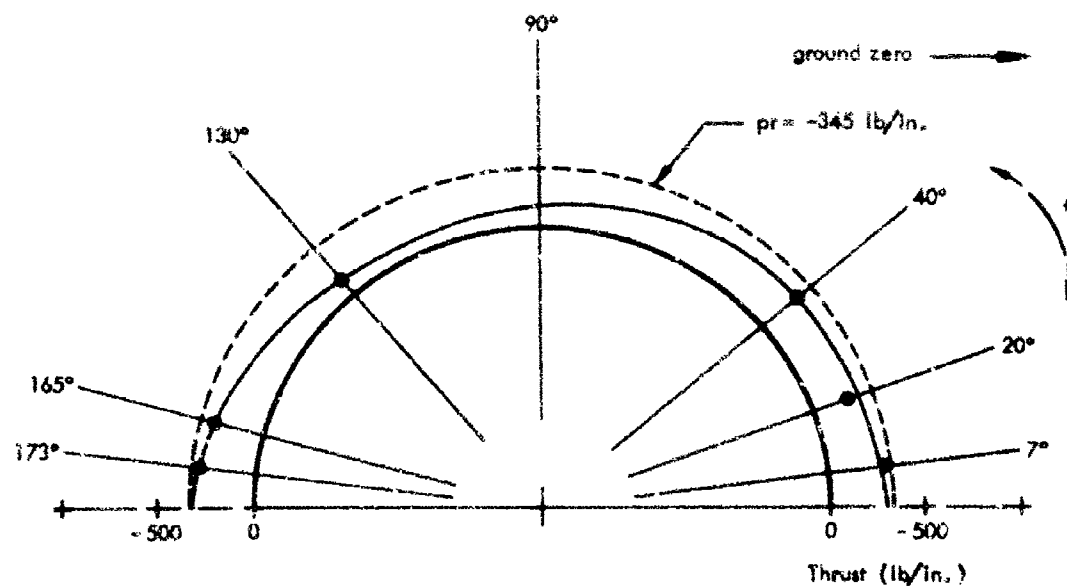


Figure 25. Thrust diagram at 20 milliseconds, arch CA-2.

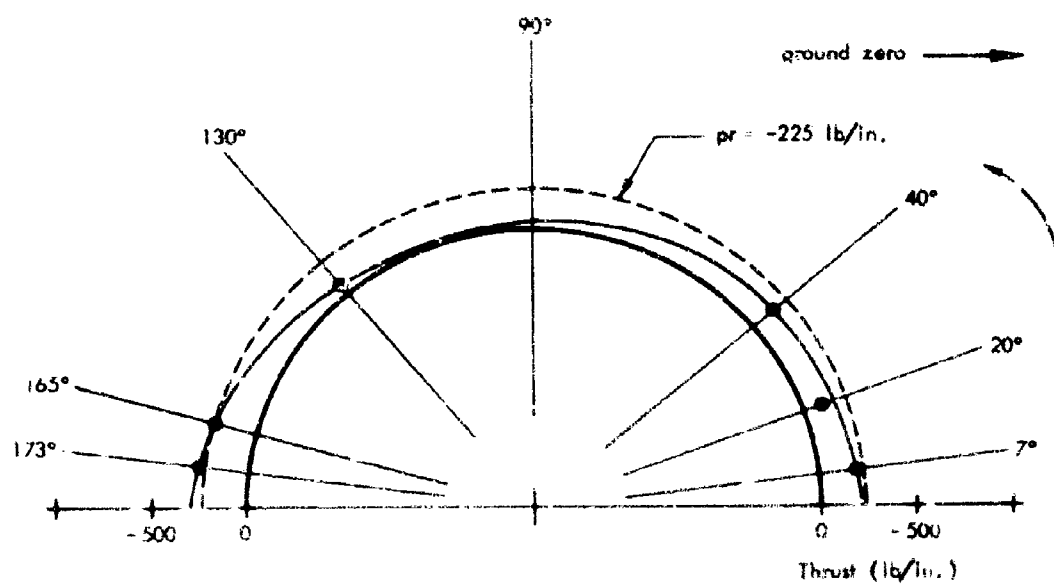


Figure 26. Thrust diagram at 30 milliseconds, arch CA-2.

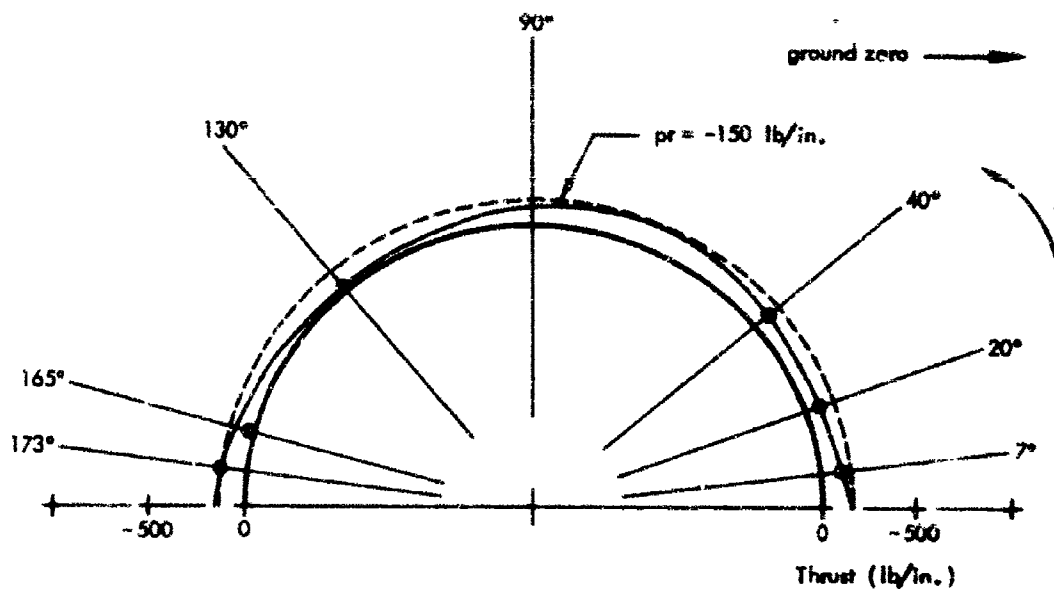


Figure 27. Thrust diagram at 43 milliseconds, arch CA-2.

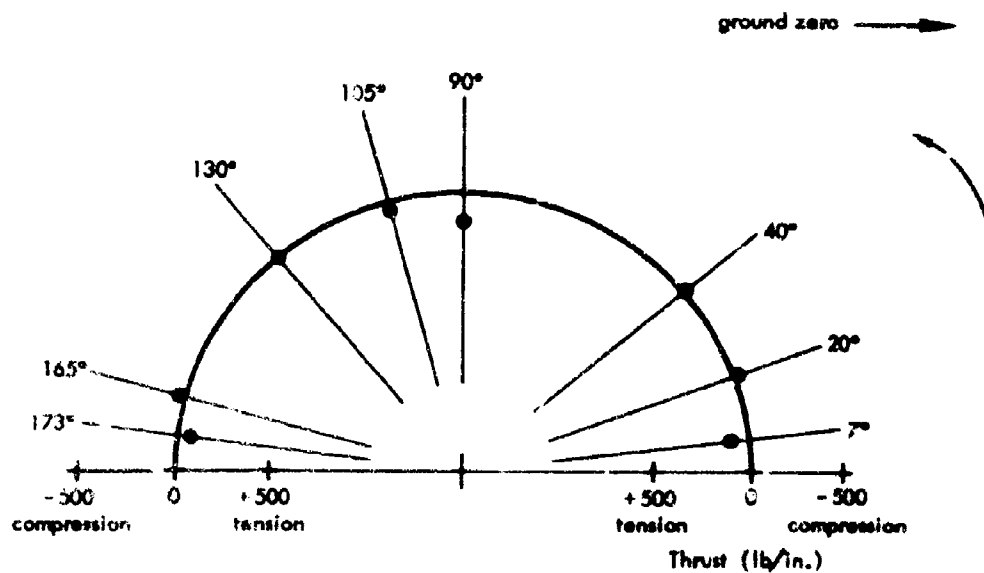


Figure 28. Residual thrust diagram at 2 seconds, arch CA-2.

Rotation of arch CA-2 was negligible; however, arch CA-1 rotated away from ground zero $1^{\circ}11'$. Even larger rotations were noted in arch CA-4 on its recovery. The blastward end wall of arch CA-4 was about 4 inches higher than the leeward end wall. This rotation must have been caused by the ground motions.

Little usable information was derivable from the survey data, partly due to failure of the velocity gage on the bunker to function properly. The first order survey data was of no value, probably because of the error resulting from the long distance that the levels had to be brought in from the bench mark.

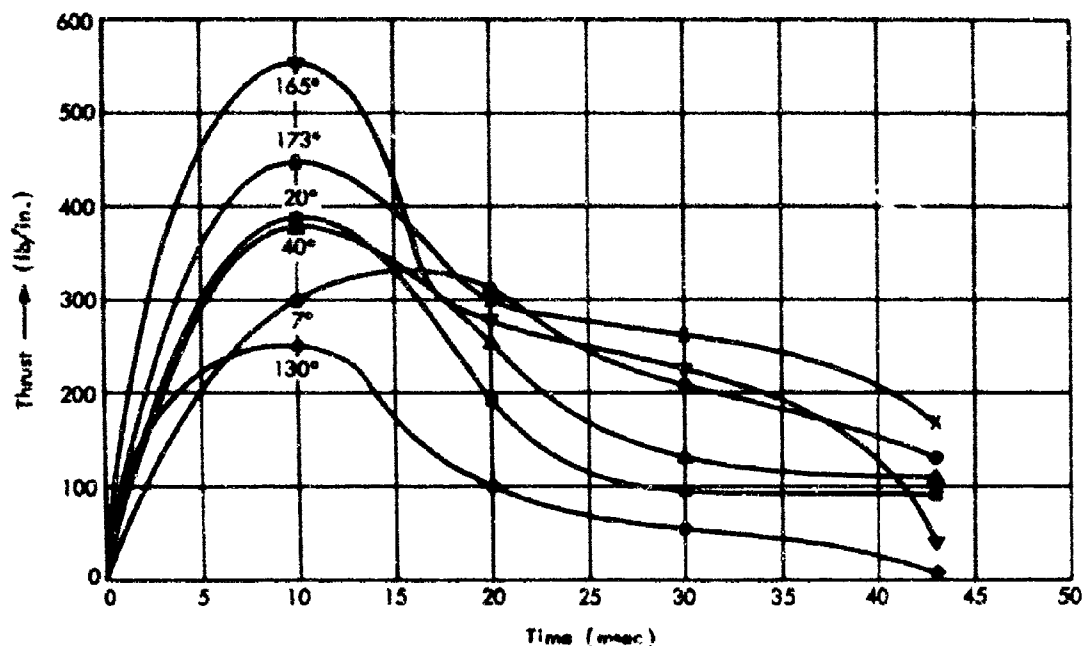


Figure 29. Thrust versus time for positions around arch CA-2.

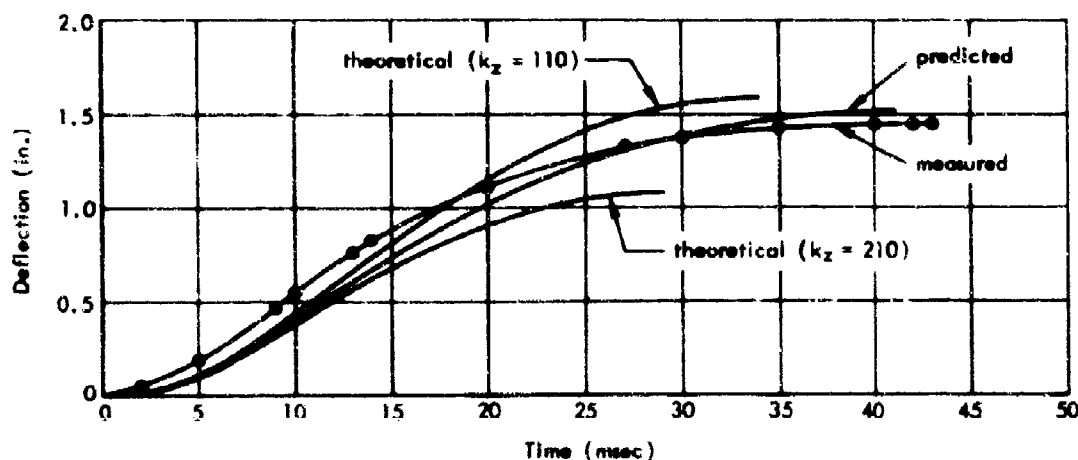


Figure 30. Deflection of the blastward footing, arch CA-1.

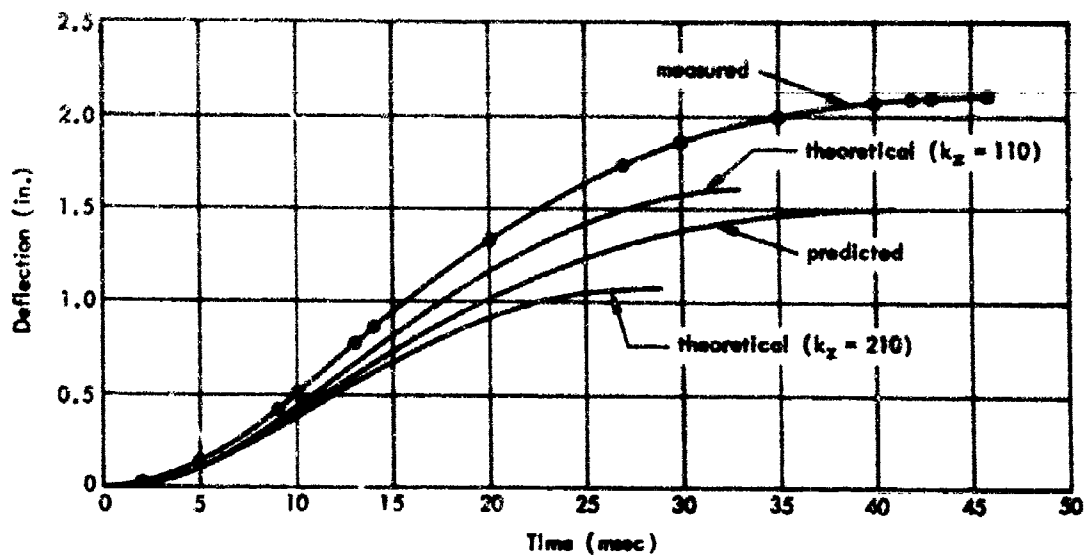


Figure 31. Deflection of the leeward footing, arch CA-1.

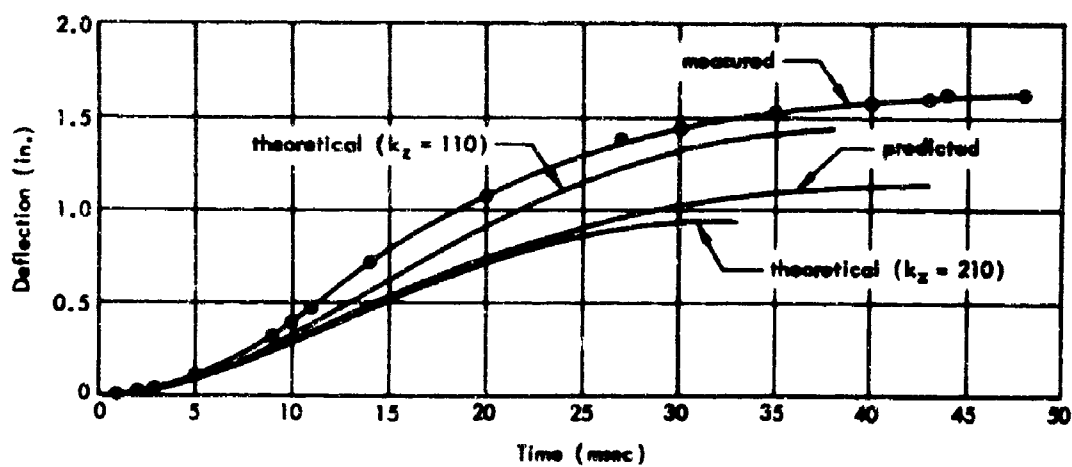


Figure 32. Deflection of the blastward footing, arch CA-2.

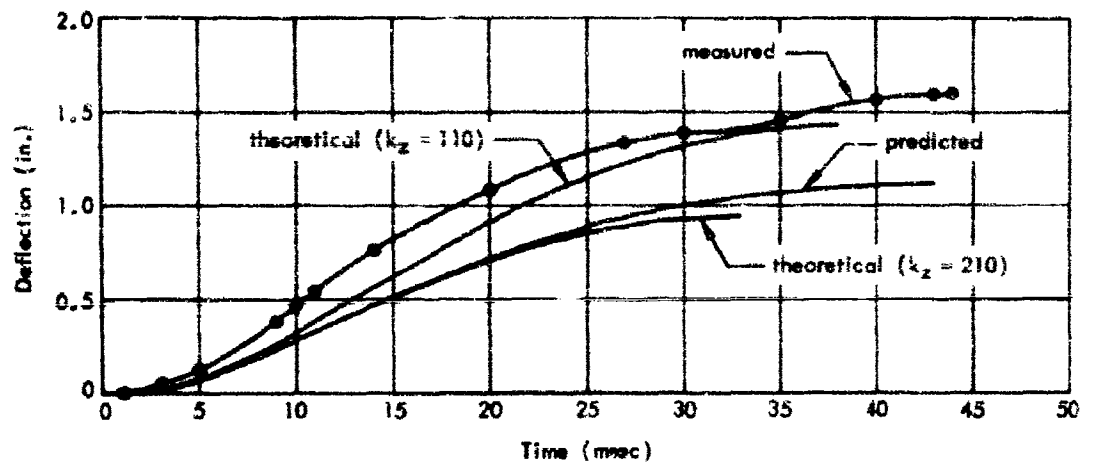


Figure 33. Deflection of the leeward footing, arch CA-2.

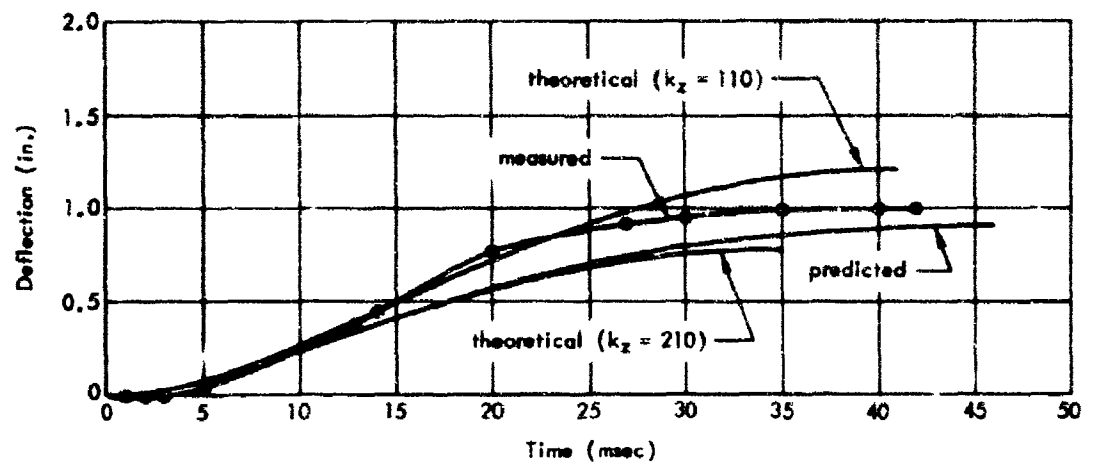


Figure 34. Deflection of the blastward footing, arch CA-3.

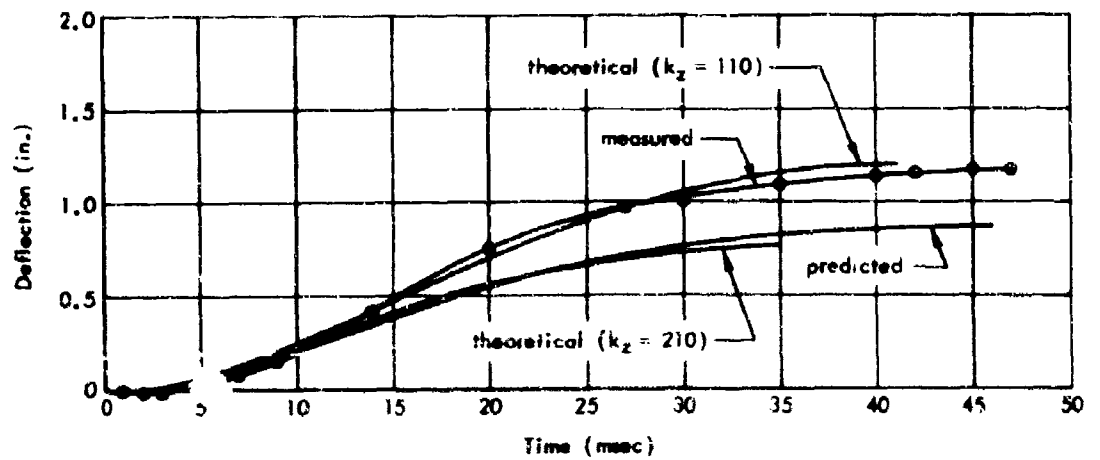


Figure 35. Deflection of the leeward footing, arch CA-3.

Table VIII. Peak Values of Body Motions

Arch	Range (ft)	Footing	Deflection (in.)			Velocity (in./sec)			Acceleration (in./sec ²)		
			Measured	Theoretical		Measured	Theoretical		Measured	Theoretical	
				$k_z = 110$	$k_z = 210$		$k_z = 110$	$k_z = 210$		$k_z = 110$	$k_z = 210$
CA-1	365	Blast side	1.48	1.576	1.074	77.6	76.1	60.8	*	12,889	12,021
		Lee side	2.10	1.610	1.095	92.6	77.4	62.1	*	12,322	11,362
CA-2**	425	Blast side	1.61	1.428	0.940	76.4	60.0	47.2	10,500	9,113	8,556
		Lee side	1.60	1.440	0.947	71.7	60.5	47.6	10,300	8,921	8,291
CA-3	482	Blast side	1.02	1.201	0.775	57.4	47.1	36.8	*	6,703	6,217
		Lee side	1.17	1.199	0.774	61.5	47.0	36.7	*	6,737	6,264

*Not measured.

**Peak free field displacements were 0.682 in. at the footing elevation and 1.09 in. at the crown elevation.

Velocity and Acceleration. Variation of velocity with time for arches CA-1, CA-2, and CA-3, are shown in Figures 36 through 41. It may be noted that the peak values of velocity occurred between 12 and 14 milliseconds. Most of the velocity traces exhibit a minor peak prior to the occurrence of maximum value. Peak values of displacement, velocity, and acceleration are given in Table VIII. Velocities obtained from integration of the accelerometer traces are considerably below the velocity obtained from the Stanford Research Institute (SRI) gages. Apparently, there was some baseline shift in the accelerometer traces as often happens in such measurements.

The acceleration traces exhibited high frequency perturbations which had to be mechanically filtered out before the data became meaningful. These perturbations were poorly defined in the first 3 milliseconds of response. To achieve suitable filtering, a curve was plotted through points midway between the peaks of the perturbations. Figures 42 and 43 are the resultant curves. Peak values of acceleration in Table VIII were obtained from the filtered curve. Peak values of velocity and deflection, by contrast, are the actual maximum values from the oscillogram traces.

Free-Field Motion

Measurements from velocity gages V2-4 and V2-3, in the free field adjacent to the structure, show that the peak absolute displacements at 6 inches and 21 inches from the surface were 1.08 inches and 0.68 inch, respectively. Absolute displacement of the floor of the structure was 0.80 inch, almost the same as the displacement of the free field at the same elevation.

Peak velocities at the 6-inch and 21-inch depths were 44 and 24 inches per second, respectively.

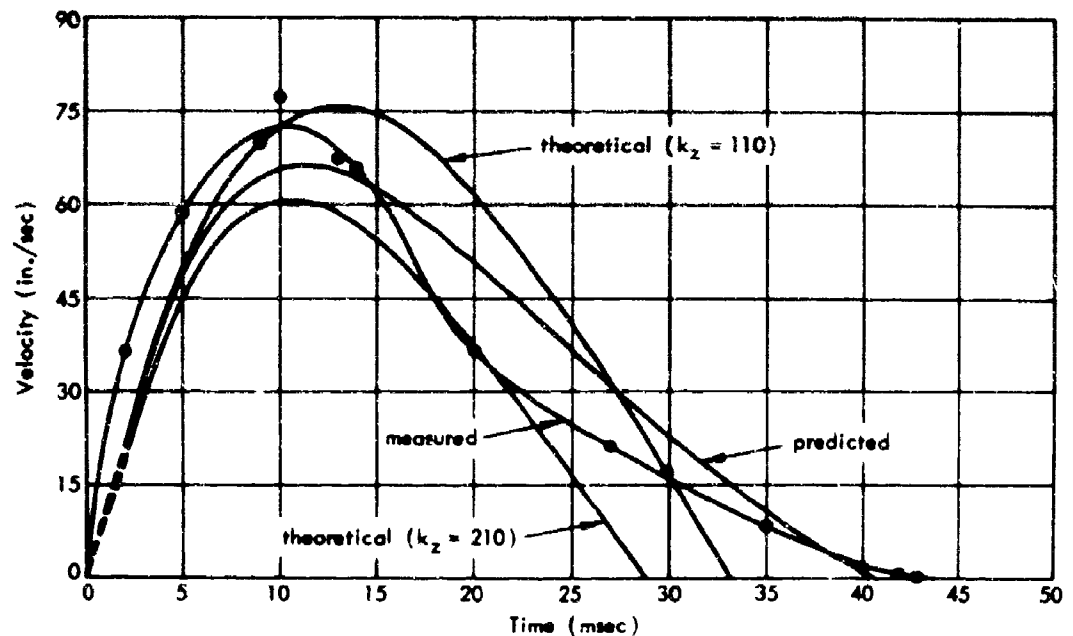


Figure 36. Velocity of the blastward footing, arch CA-1.

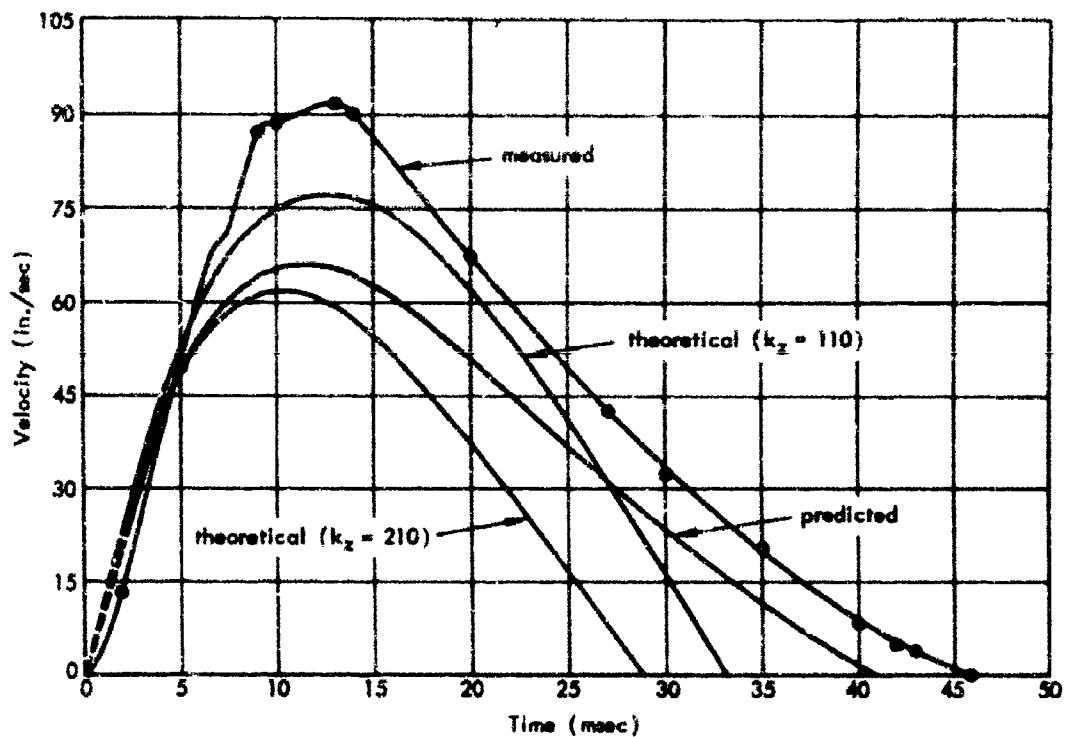


Figure 37. Velocity of the leeward footing, arch CA-1.

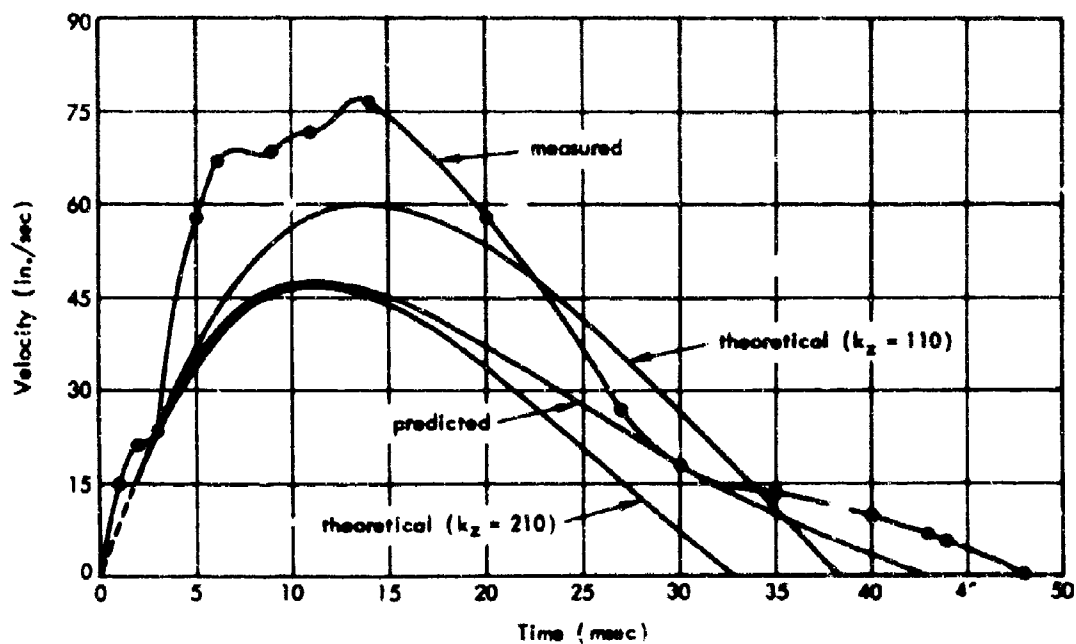


Figure 38. Velocity of the blastward footing, arch CA-2.

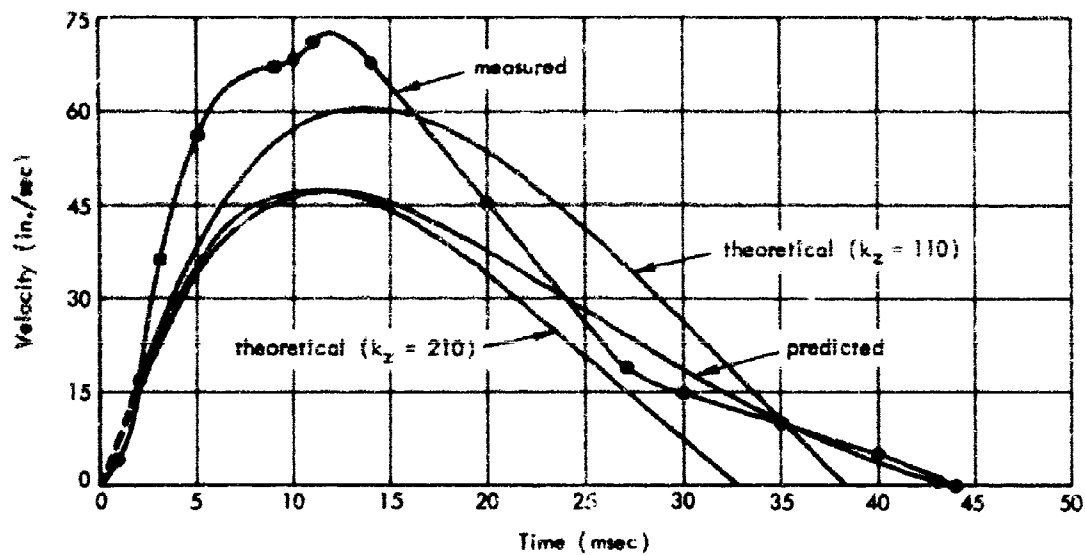


Figure 39. Velocity of the leeward footing, arch CA-2.

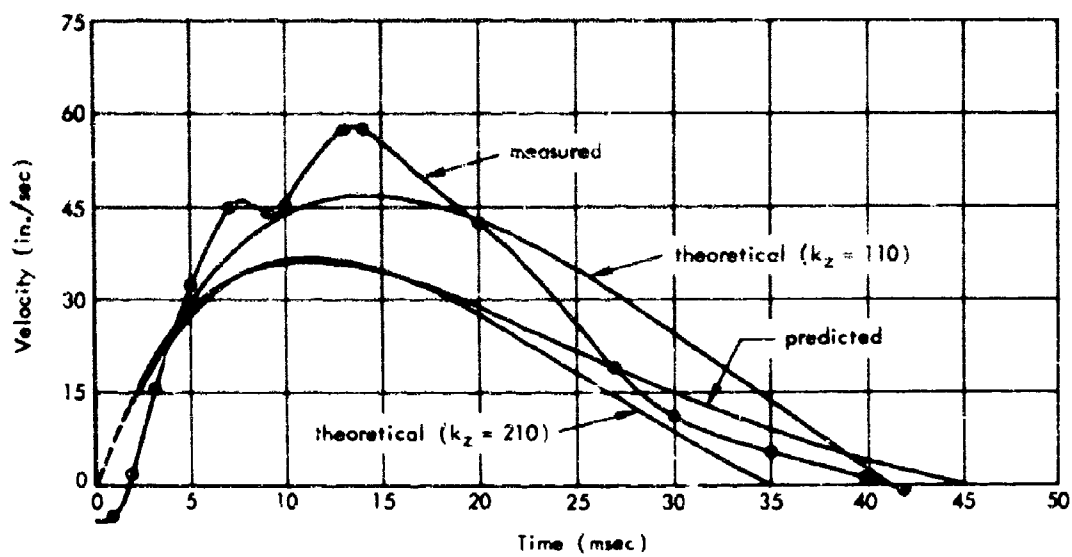


Figure 40. Velocity of the blastward footing, arch CA-3.

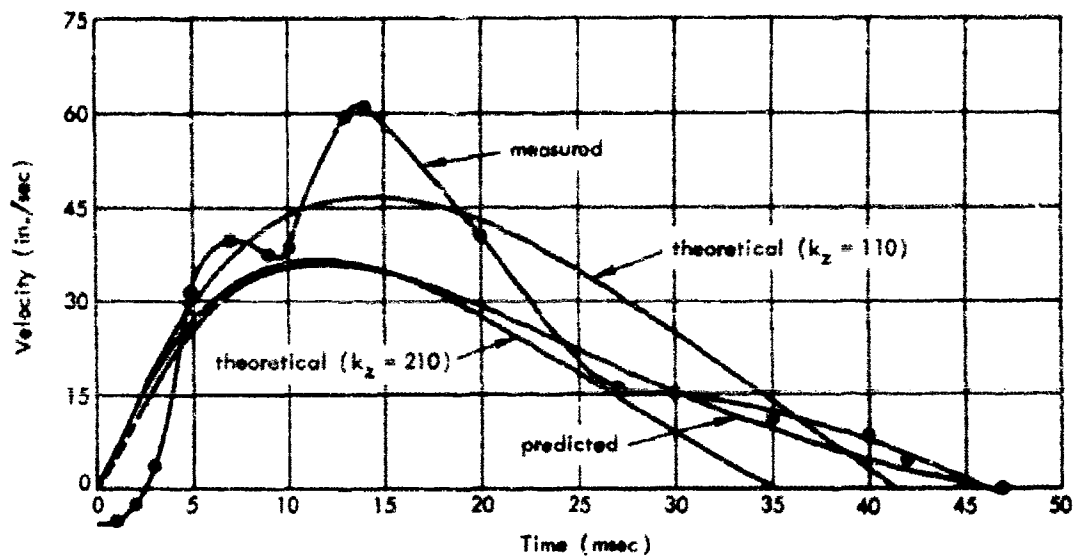


Figure 41. Velocity of the leeward footing, arch CA-3.

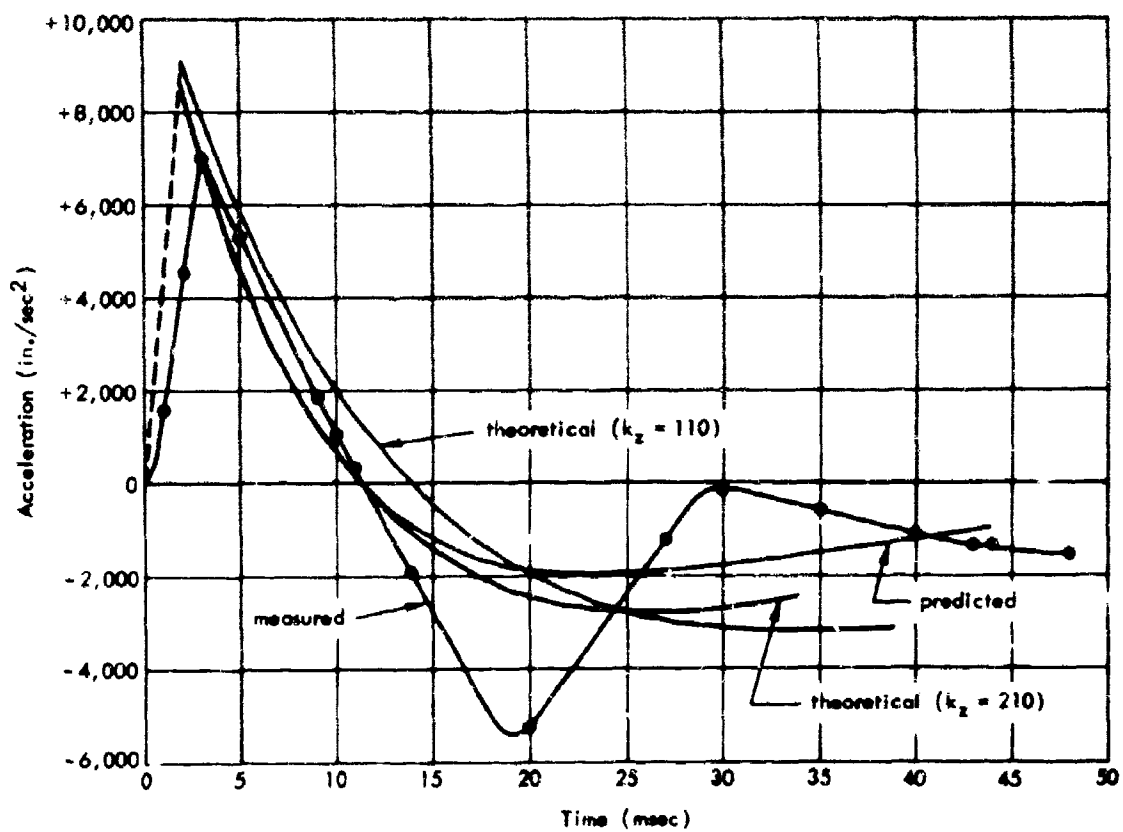


Figure 42. Acceleration of the blastward footing, arch CA-2.

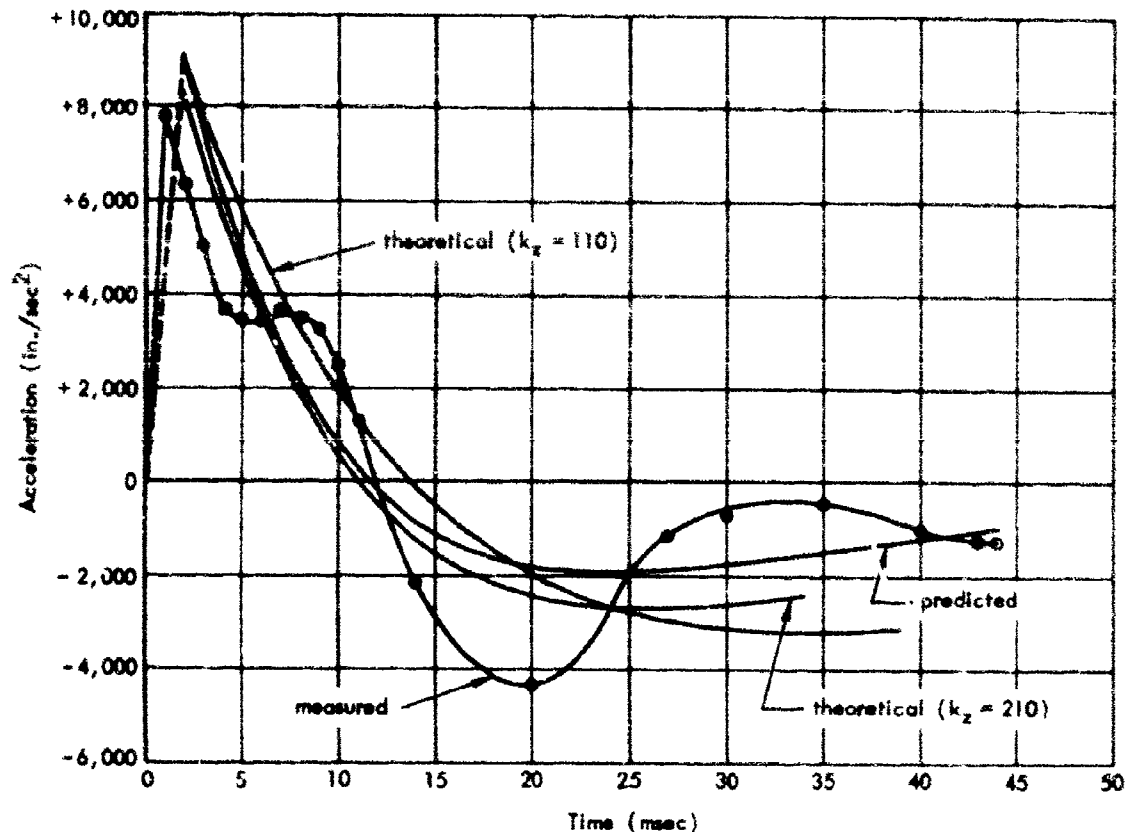


Figure 43. Acceleration of the leeward footing, arch CA-2.

Tie Rod and Floor Behavior

During the first 12 milliseconds, the tie rod, Figure 7, was in tension. Thereafter, it developed a very large compression which reached a maximum value of about 4,000 pounds at 23 milliseconds. The average horizontal thrust on the footings reached a maximum of 280 pounds per inch of length. The horizontal force was larger than expected which emphasizes the need for a bracing system to provide lateral support and prevent rotation of the footings. Failure to include such a support is believed to be primarily responsible for the footing failures of the Project 3.6 arches in Operation Hardtack.⁸ The horizontal thrust also may have been partly responsible for the floor failure in the Operation Plumbbob 3.3 arches.¹ In the latter instance, the footing was probably pushed against the slab and, as a consequence, the edge of the floor was forced downward with the footing causing a break in the floor approximately 2 feet in from the spring line.

Movement of the floor was determined from double integration of an acceleration trace. A maximum absolute deflection of 0.62 inch occurred at 40 milliseconds. This data indicates that the deflection of the floor was small compared to the translational deflection of the structure.

Soil Arching

The term "arching" is used here to mean the total shear on a vertical plane through the footings. This force, as a percentage of the surface load, is plotted versus time in Figure 44. It was determined from a vertical equilibrium of the forces on the free body, shown in the

diagram of Figure 44, by using the measured thrust as the footing reaction and an inertial force, based upon the mass of the structure and the soil over the structure, times the acceleration of the footings.

The shape of the arching curve of Figure 44 is somewhat different from that determined from tests in the blast simulator.³ The results shown in Figure 44 indicate that at early times most of the load is transmitted through the soil around the arch.

Recapitulation

The sequence of events influencing the behavior of arch CA-2 was:

1. The surface overpressure reached a peak value in about 1 millisecond and gradually decayed to zero in 124 milliseconds.
2. The maximum thrust was reached in about 10 milliseconds and the maximum moment was reached in about 25 milliseconds.
3. The peak deflection of the crown was reached in about 26 milliseconds.
4. Maximum deflection of the footings was reached in an average time of 46.2 milliseconds.

Body motion was by far the most significant mode of response, although first symmetrical mode response was also sizable. Some antisymmetrical mode behavior was evident, but it was smaller than expected.

Computer Analysis

Computer Program. A Fortran computer program was written using the theory given in Appendix A. The objective of the program was to obtain data for comparison with the experimental results. The program was designed to receive the dominant parameters corresponding to any equivalent-triangular load, any semicircular arch oriented "side-on" to the load, and any soil. With this input, footing deflections, velocities, and accelerations can be computed, accounting for rotational and translational body motions.

Computer Input. Input to the computer program is shown in Table IX. The three types of data used as input represent dimensions of the structure, characteristics of the load, and properties of the soil.

Dimensions of the model were established in the design of the experiment. Footing dimensions, depth of burial, and arch radius were one-tenth scale of a Navy standard personnel shelter. The stiffness and the mass of the arch were greater than the scaled quantities to insure against failure of the shell. Mass was obtained by weighing the models, including the arch, footings, footing braces, and transducers. End wall and floor masses were not included since these are separate assemblies not directly attached to the arch.

Peak overpressure was measured at the surface of the ground at each model location using BRL self-recording pressure gages. Effective duration was obtained by calculating the impulse (area under the overpressure-time curve) from zero time to the time of maximum deflection, and from this, constructing an equivalent triangular loading.

Velocity of the blast front was estimated using the formula

$$U = C_0 \sqrt{\frac{1 + 6 p_{s0}}{7(14.7)}}$$

where $C_0 = 1,117$ fps is taken as the ambient sound velocity ahead of the blast, and p_{s0} is the peak side-on overpressure. It is recognized that C_0 varies with atmospheric conditions

$$A = \frac{F}{\bar{p}r} \times 100$$

$$F = \bar{p}r - R - \frac{m\ddot{y}}{2}$$

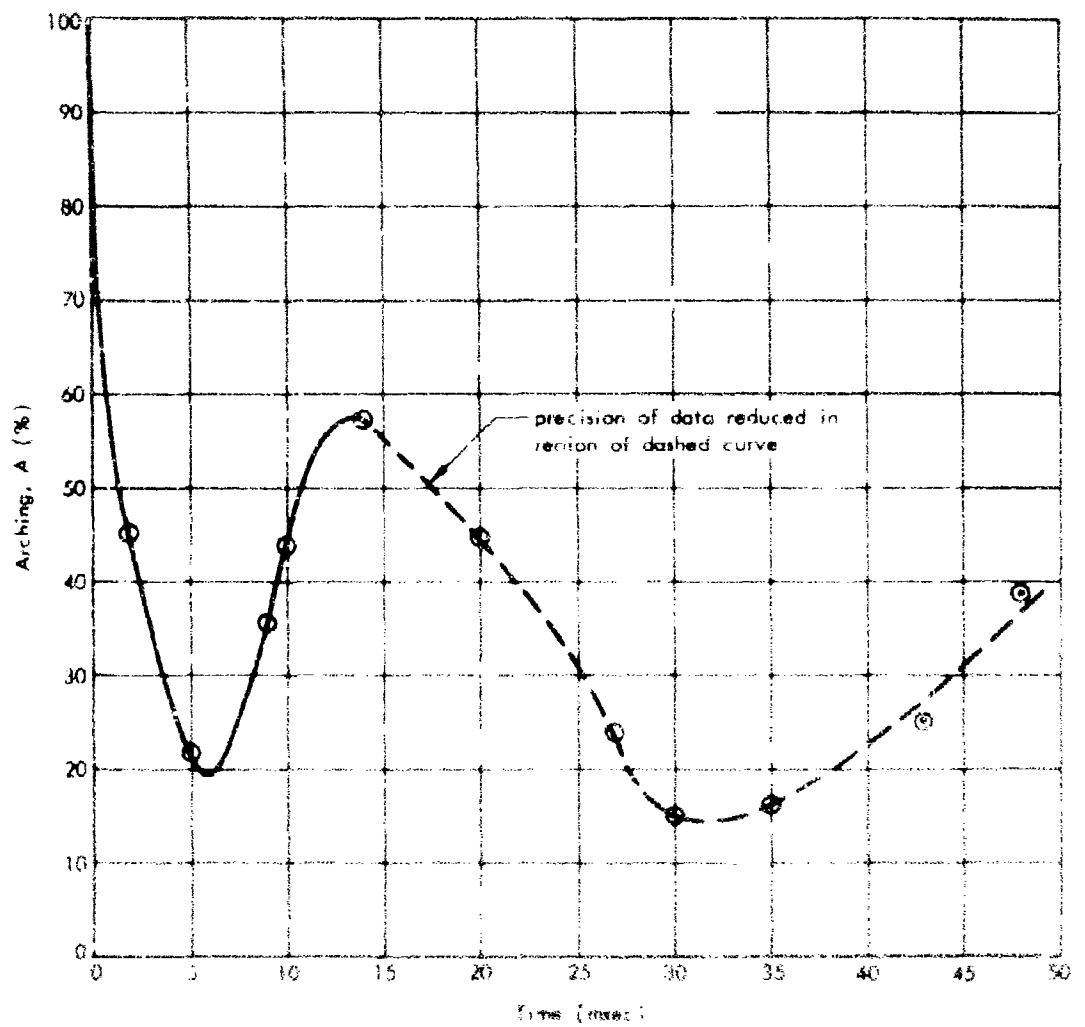
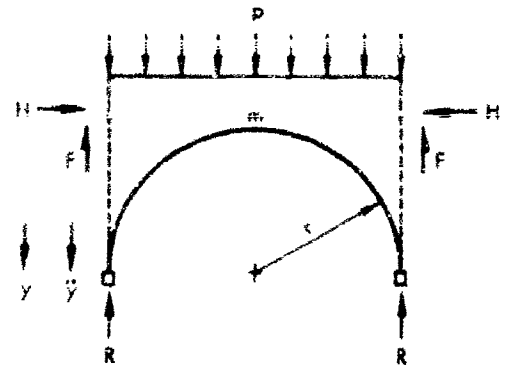


Figure 44. Arching of the wall about arch CA-2.

Table D Computer Input

Type Data	Symbol	Definition	Input			
			Measured Values	Predicted Values	Units	Arch
Structure Dimensions	d_0	Depth of cover at crown	8.00	8.00	in.	All
	r	Radius of the arch	15.0	15.0	in.	All
	b	Width of the footings	1.24	1.25	in.	All
	H	Height of the footings	1.88	1.875	in.	All
	m	Mass of the arch and footings	0.745	0.46	slug/ft	CA-1
	m	Mass of the arch and footings	0.760	0.46	slug/ft	CA-2
	m	Mass of the arch and footings	0.737	0.46	slug/ft	CA-3
Load Characteristics	p_0	Effective peak overpressure	83	85	psi	CA-1
	p_0	Effective peak overpressure	60	60	psi	CA-2
	p_0	Effective peak overpressure	45	45	psi	CA-3
	t_d	Effective duration	30	82	msec	CA-1
	t_d	Effective duration	39	97	msec	CA-2
	t_d	Effective duration	45	118	msec	CA-3
	U	Velocity of blast front	2,700	2,700	fps	CA-1
	U	Velocity of blast front	2,400	2,400	fps	CA-2
	U	Velocity of blast front	2,100	2,200	fps	CA-3
Soil Properties	γ_s	Density of backfill soil	111	110	pcf	All
	k_z	Coefficient of subgrade reaction	110 and 210	300	psi/in.	All
	ϕ	Angle of internal friction	34.5	35	degrees	All
	c	Cohesion	0	0	none	All
	K	Coefficient of lateral earth pressure	0.32	0.32	none	All
	C_s	Velocity of shock front	1,000	1,300	fps	All

Density of the soil was determined at the test site, using a segmented box and the sand drop method described in Appendix B. The most dense segment was 111.5 pcf and the least dense segment was 109.7 pcf. The average density of six segments was 110.8 pcf.

The coefficient of subgrade reaction in Table IX is the ratio of the average pressure on the bottom of the footing to the vertical displacement of the footing. The modulus as a function of time was obtained with a plot of thrust, from strain measurements at the 7- and 173-degree positions on the arch, versus vertical deflection of the footings obtained from integration of the velocity measurements. A plot showing the variation of the coefficient with time is given in Figure 45. It may be noted from this figure that there is no great variation in the modulus during the period from 10 to 30 milliseconds when most of the deflection of the footings occurs. This would lead one to believe that use of a constant value for the modulus in the theory is justified. In selecting a reasonable coefficient of subgrade reaction, the mean value occurring during the period from 10 to 35 milliseconds, when most of the deflection takes place, might be used. The coefficient is obtainable from the load-deflection curve of the footing, Figure 46. Subgrade reaction pressure is found by dividing the thrust at the spring line per unit of length by the area of the footing per unit of length. Both absolute and relative deflections are plotted as determined from the velocity gage measurements. It is interesting to note the difference of the character of this curve as compared with typical load-deflection curves from plate bearing tests.⁶ Initially, the foundation is very stiff; then, at about 350 psi/in., it appears that punching commences and the reaction pressure drops off rapidly. The subgrade reaction, Figure 46, increases again at the same time the acceleration, Figure 43, goes negative and rises until punching corresponding to the lower surface surcharge pressure (at 20 milliseconds) develops.

Both the absolute and relative deflections are plotted in Figure 46 versus the subgrade reaction to show how much stiffer the coefficient based on the relative deflection is than the corresponding value based on the absolute deflection. Secant moduli (coefficients), based on the absolute deflection curves and accounting for the inertia of the soil moving with the footing, are plotted in Figure 45. The inertial component, based on a soil mass with a diameter four times the footing width, is small. From Figure 45, the mean value of the coefficient of subgrade reaction, during the period from 10 to 35 milliseconds when most of the deflection takes place, is about 210 psi/in. This is the value used in the computer program. Computed results are also generated for a modulus of 110 psi/in.

The angle of internal friction of the soil was determined as described in Appendix B. Cohesion was taken as zero, because of the dry condition of the sand. The estimated coefficient of lateral earth pressure was based on triaxial tests of a similar material. Stress wave velocity in the soil was determined by using the time of arrival at the free field velocity gages and the known distance between them.

Computer Output. The computer output, composed of footing deflections, velocities, and accelerations, is plotted with measured data in Figures 30 through 43. Curves labeled "theoretical" were obtained from the computer, using measured input; curves labeled "predicted" were obtained before the test from the computer, using estimated input data. A set of curves showing the interrelation of the dominant parameters is given in Figure 4.

Theoretical versus Experimental Results

Using the constants determined as previously indicated, the computer program was run to obtain theoretical data for comparison with the experimental results. Theoretical and experimental data are given in Table VIII and in Figures 30 through 43. For a coefficient of subgrade reaction of 210 psi/in., the experimental values are larger than those determined by the theory. Use of a coefficient of subgrade reaction of 110 psi/in. gives computed data that agrees well with the experimental results. The latter data is also included in Table VIII and in Figures 30 through 43.

The value of 110 psi/in. is the coefficient from Figure 45 at a time equal to 67 percent of the time to maximum displacement. It is the lowest value that could possibly be justified. Except for the first few milliseconds, the coefficient of subgrade reaction is considerably less than the initial tangent modulus of 300 psi/in. determined from the static plate bearing tests.

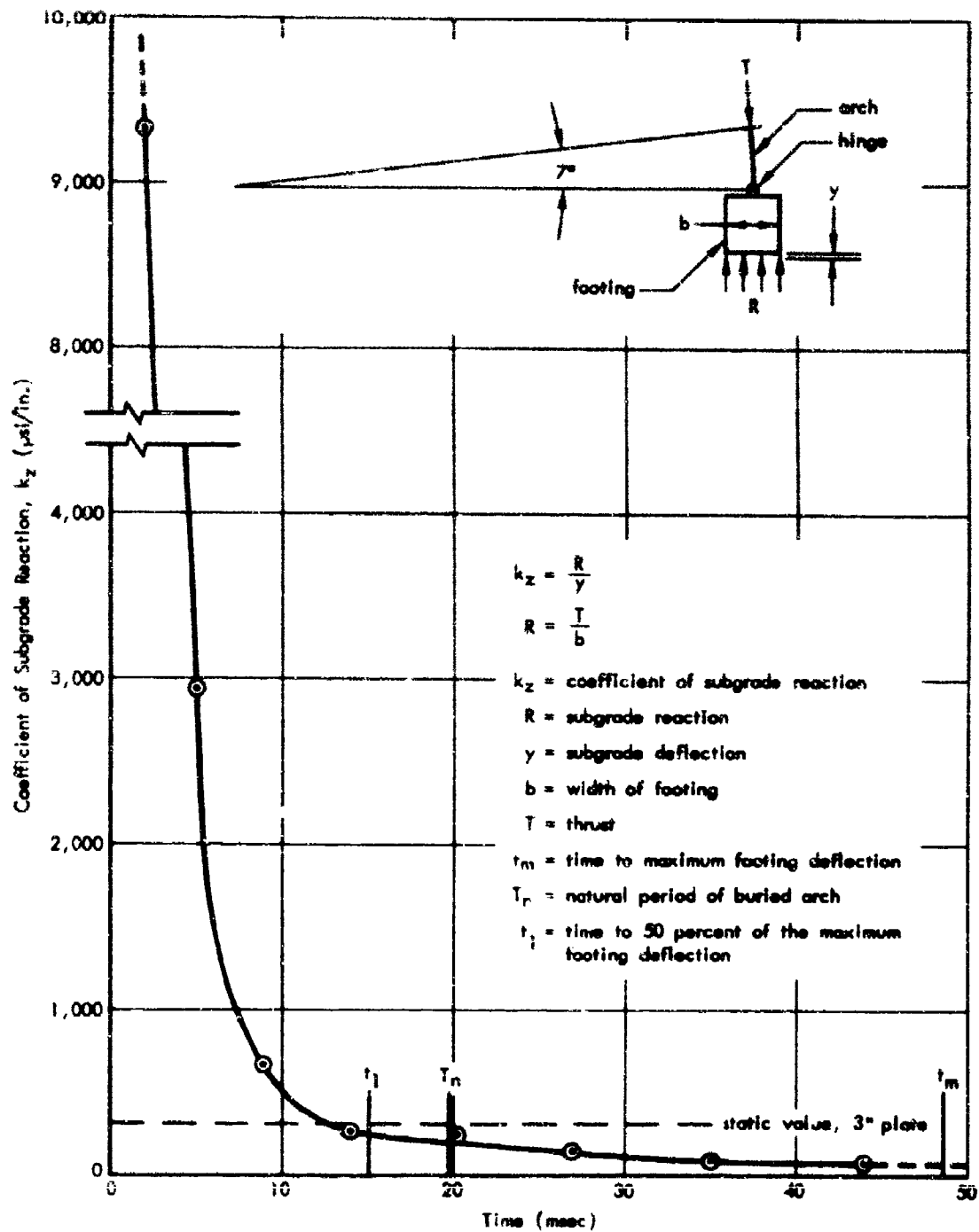


Figure 45. Dynamic coefficient of subgrade reaction.

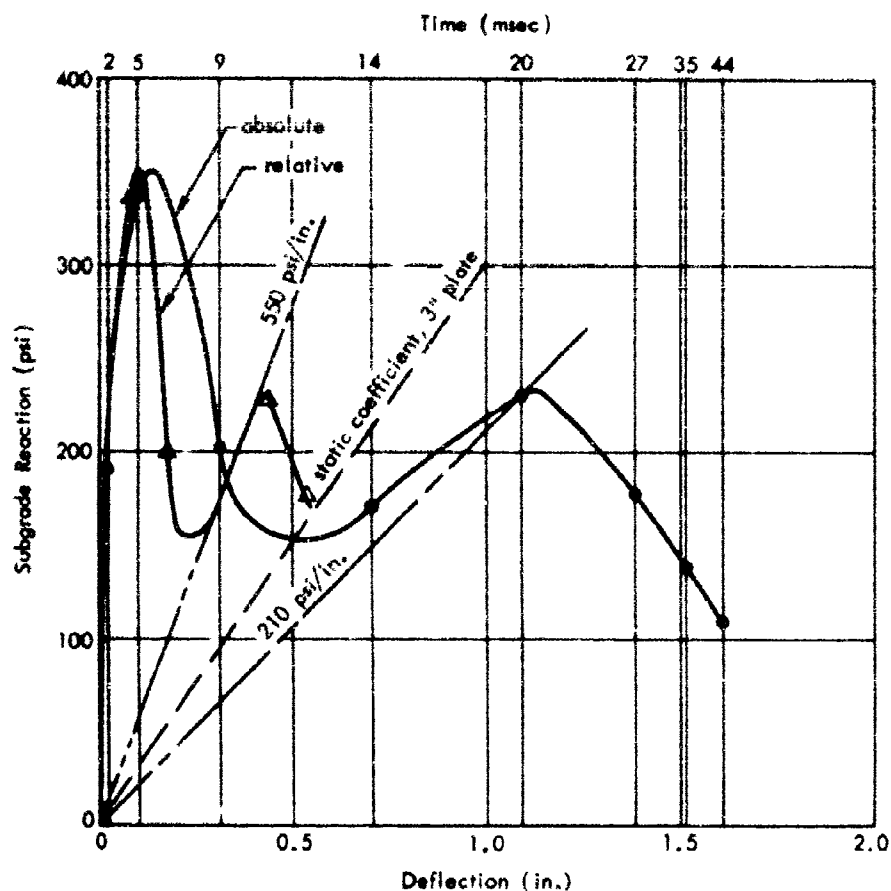


Figure 46. Subgrade reaction versus deflection.

Agreement between response and the theory was best for arch CA-3, the arch furthest from ground zero, and was progressively worse for the closer arches. Arch CA-1, the closest of the large arches, rotated considerably, although this rotation was not predicted by the theory.

From the 3-inch plate bearing tests described in Appendix B, the coefficient of subgrade reaction was found to be 300 psi/in. The corresponding coefficient for the 1.24-inch-wide footing would be expected to be greater than 300 psi/in. because of the narrower width and the fact that the arch footing is subjected to a surcharge pressure. As previously stated, however, the effective coefficient of subgrade reaction from Figure 45 is only 210 psi/in. The reason is that the latter value is based upon absolute rather than relative displacements.

To explain further, consider a semi-infinite soil field alone. Application of a surface overpressure will cause deformation much the same as described in Reference 9. This action may be thought of as a load on a giant spring, although probably a nonlinear one. Relative buried arch footing deflections, in effect, are superimposed on the motion of the free field. Thus, the effective coefficient for defining absolute body motion should be the equivalent coefficient of a series spring system. As is well known, the equivalent spring constant of two springs in series is the product of the spring constants divided by their sum. The resulting equivalent spring constant is less than either component which accounts for the low effective coefficient of subgrade reaction obtained from Figure 45. It is important in designing a footing for a buried structure that a coefficient of subgrade reaction (or the equivalent load-deflection relation) based upon absolute deflections is used, instead of one based on relative deflections if absolute deflections are of dominant concern.

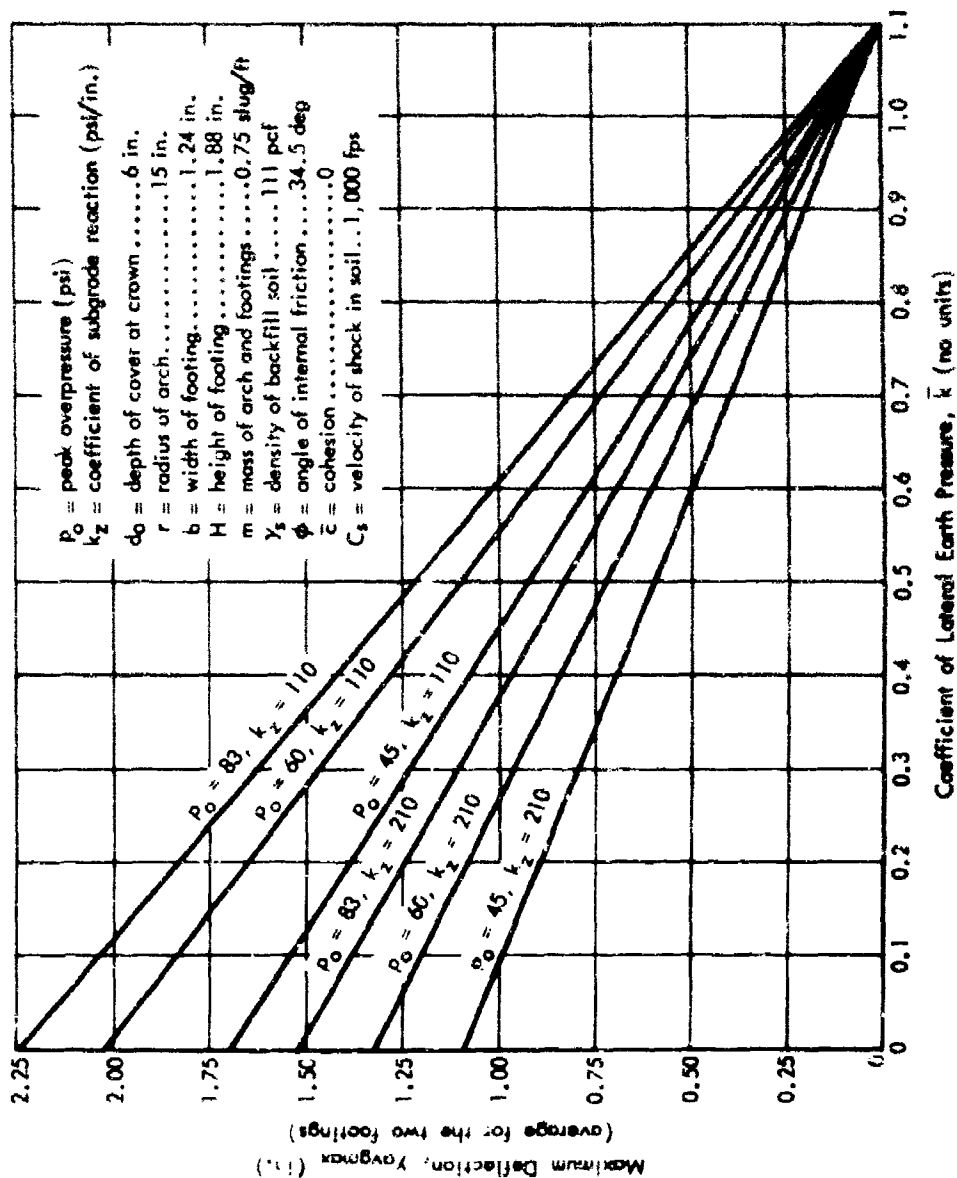


Figure 47. Dominant parameters in the theory.

Examination of the theory in the context of the experimental results and other recently gained knowledge indicates that the theory as formulated could be improved in two respects: (1) the coefficient of subgrade reaction should not be taken as a constant; the true load-deflection relation should be used, and (2) the arching term should be a function of deflection.

The dynamic or static load-deflection relation of a bearing plate or footing on noncohesive soils can be represented analytically by an exponential equation of the form

$$p = Cy^a \quad (3)$$

where p = unit load on the plate or footing

y = deflection of plate

C = constant

a = exponent, a constant

For soils with cohesion, the corresponding relation would be of the form

$$p = \frac{C_1 \left(\frac{y}{y_m} \right)}{1 + \left(\frac{y}{y_m} \right)^2} \quad (4)$$

where y_m = maximum plate deflection

C_1 = constant

A recent theoretical study of the classical trapdoor problem has shown that arching is a function of deflection.⁴ By treating the soil as an elastic material, it was found that the percentage of the surface load carried by arching might be expressed as a function of b/h , and $x = ph/yE$, where $2b$ is the width of the trapdoor, h is the depth of soil cover over the door, p is the uniform surface pressure, d is the deflection of the trapdoor, and E is the modulus of the soil. Results from the theory show that Poisson's ratio has a negligible effect on the arching.

Although the theory was developed for the trapdoor, it is applicable to the buried arch since the arch may be treated as a curved trapdoor insofar as arching is concerned. Empirical fits of the plots from the cited arching theory⁴ may be written in the form

$$\frac{V_1}{pr} = a_1 x^{-b_1} e^{-c_1/x} \quad (5)$$

where V_1 = arching shear

r = arch radius

a_1, b_1, c_1 = constants depending on b/h

The other terms in Equation 5 are as previously defined.

Incorporating nearly exact relations for the load-deflection characteristic of the soil and for arching should bring the theory in conformance with experimental behavior. Whether or not it would be worthwhile adding these terms, with the attendant complication, is argumentative in view of the wide variation in soil properties expected at a given installation in the field. For the present, at least, it should be sufficient to use the theory as currently defined with an equivalent (secant) coefficient of subgrade reaction to account for the relatively reduced resistance of the soil, once punching has been initiated. Even with a more exact theory, prediction of deflections within very close tolerances still could not be expected, because of the nature of soil as a structural material.

Consequences of Observations

On completion of an experimental program such as Project 3.4, it should be determined what information can be expected from the test results that will aid in the design and construction of full-size buried structures. Most importantly, the experiment shows that with the proper input parameters, body motions can be estimated with reasonable accuracy. Beyond this, the experimental results and accompanying theories provide basic information needed for a theory to define the optimum footing width. Information also is provided which demonstrates the nature of the moments and thrusts induced by traveling-blast loading and, consequently, information on the nature of the loads carried by the soil in arching.

The tests provide a basis of judgment regarding what relative deflection may occur between the footing and the floor slab and between the footings and the free field. An important aspect of behavior is that the floor motions may be a fraction of the body motion of the structure itself and that the floor displacement will be about equal to the displacement of the free field. Further, observation of the acceleration traces gives the designer some understanding of the nature of the shock input to a shelter, although it is emphasized that shock input is not readily scaled.

Crushing of the smaller arches and denting of the larger arches by the ejecta point up the possible need for a missile shield over personnel shelters. If a shelter is in the vicinity of above-ground equipment or buildings that might be destroyed by a relatively low overpressure attack, it is possible that the debris created might impact above and penetrate the shelter. Wherever such a possibility exists, consideration should be given to the possibility of providing shielding from such missiles.

The physical evidence provided by the tie rod measurements furnishes positive proof of the large lateral forces imposed upon the footing of a buried arch shelter. The designer should recognize the existence of such forces and provide suitable struts to prevent large lateral deformations or rotation of the footings.

Perhaps most important of all, this study demonstrates that the body motion results from the compression of the soil field and from the relative deflection of the footings with respect to the soil field. Thus, an appropriate coefficient of subgrade reaction should be used, depending on whether the absolute or relative deflections are being determined.

Deficiencies of Work

Close controls were maintained over the material properties and the instrumentation and, in general, the experiment was considered most successful. The small uninstrumented structures were lost due to crushing by soil bombs from the ejecta. In addition to this unpredicted occurrence, the only serious data loss was due to failure of the velocity gage on the instrument bunker. Malfunction of this gage prevented establishment of a postshot bench mark within close proximity of the structures from which survey data could be obtained. The first order survey data brought in from beyond the range of influence of the blast proved to be too inaccurate to be of use.

In addition to the forementioned difficulties, the vertical rod from the crown of the structure to the soil surface, used for defining a preshot and postshot elevation of the crown of arch CA-2, caused difficulties in interpreting the moments near the crown. It was apparent from the strain gage reading that the soil above the crown of the structure experienced considerable motion with respect to the crown of the structure, inducing extraneous moments. It is apparent that no such appendages should be fastened to the shell of an arch structure. The difficulties mentioned are considered the only deficiencies of the experiment; however, it would have been most desirable to have obtained soil-structure interface pressure measurements.

FINDINGS AND CONCLUSIONS

From analysis of the data of the four large arches and from comparing the results with the theory, it was found that:

1. The measurable natural periods of the uncovered arch agreed reasonably well with the theoretical values.
2. Moments and thrusts induced by backfilling were negligibly small; however, the crown deflection was significant.
3. The natural period of the covered arch was much less than the corresponding natural period of the uncovered structure.
4. The peak overpressures were almost exactly those predicted.
5. Actual positive-phase durations were approximately 40 percent longer than predictions.
6. Body motions were larger than predicted.
7. The relative displacement between the free field and the footings in the quasi-static state was about 57 percent of the absolute footing displacement.
8. Asymmetric response of the shell was evident; moments on the leeward side were about 30 percent greater than those at corresponding positions on the blastward side.
9. Thrust variation around the arch was fairly uniform; in general, the thrust was less at the crown than in the vicinity of the spring line.
10. The thrust data indicates that interface shears were developed.
11. The velocity gages used to measure footing deflection proved to be excellent motion-sensing devices. Peak absolute footing displacement for arch CA-2 was 1.6 inches.
12. The peak floor deflection was about 40 percent of the footing displacement. Peak floor deflection occurred at about the same time as the maximum footing deflection.
13. Forces in the footing tie bar were large; an initial tension phase was followed by a much larger compression phase.
14. Body motions from the unmodified theory did not correlate well with the measured data.

Comparisons of the results of the Project 3.4 tests with the theory revealed areas in which the development can be improved. The theory, as set down in Appendix A, can be expected to predict deflections correctly only if a suitable modulus is employed. It is evident that a correct representation of the soil-arch system can be achieved only by expressing the arching shear as a function of deflection.

The experiment was successful in permitting achievement of primary and secondary objectives. Tertiary objectives of gaining information on the effect of depth of cover and footing width were not achieved because of failure of most of the eight small arches under impact from the large clods of hard clay in the ejecta.

ACKNOWLEDGEMENTS

Appreciation is extended to all those who aided in bringing the Project 3.4 experiment to a successful conclusion. The authors are indebted to I. M. Derr and D. H. Johnson of the NCEL Instrumentation Division for layout, setup, and checkout of the instrumentation and for writing the corresponding section of this report, Appendix C.

A major contribution to the Project was made by L. W. Heller, of NCEL, who supervised the soil placement and authored Appendix B. The field work accomplished by T. J. Landrum, M. C. Chapman, and R. M. Topping, Yeoman Second Class, USN, is gratefully acknowledged.

Efficient support was provided Project 3.4 by personnel of the Suffield Experiment Station.

REFERENCES

1. Operation Plumbbob, Project 3.3. WT 1422: Evaluation of Buried Corrugated Arch Structures and Associated Components, by G. H. Albright, et al. DASA Field Command, Sandia Base, Albuquerque, New Mexico, 28 February 1961.
2. U.S. Naval Civil Engineering Laboratory. Technical Report R-278: Static Loading of Small Buried Arches, by H. L. Gill and J. R. Allgood. Port Hueneme, Calif., 31 January 1964.
3. U.S. Naval Civil Engineering Laboratory. Technical Report R-216: Blast Loading of Small Buried Arches, by J. R. Allgood, C. R. White, R. F. Swalley, and H. L. Gill. Port Hueneme, Calif., 3 April 1963.
4. U.S. Naval Civil Engineering Laboratory. Technical Note N-591: Arching in Soil Due to Yielding of a Rigid Horizontal Strip, by C. V. Chelepati. Port Hueneme, Calif., October 1964.
5. U.S. Naval Civil Engineering Laboratory. Technical Note N-281: Failure Modes of Impact-Loaded Footings on Dense Sand, by L. W. Heller. Port Hueneme, Calif., 27 January 1964.
6. U.S. Naval Civil Engineering Laboratory. Technical Report R-338: Static and Dynamic Plate-Bearing Tests on Dry Sand with Overburden, by C. R. White. Port Hueneme, Calif., 7 October 1964.
7. U.S. Naval Civil Engineering Laboratory. Technical Report R-344: Behavior of Buried Cylinders, by J. R. Allgood. Port Hueneme, Calif., 8 January 1965.
8. Operation Hardtack. WT 1626: Response of Earth-Confined Flexible Arch Structures in High Overpressure Regions, by P. J. Rush and J. C. LeDoux. 1961. SECRET
9. S. D. Wilson and E. A. Sibley. "Ground Displacements from Air-Blast Loading," Journal of the American Society of Civil Engineers, vol. 88, no. SM6, part 1, December 1962.
10. Air Force Special Weapons Center. TDR-62-9: Design and Analysis of Foundations for Protective Structures, by K. E. McKee and S. Shenkman. Armour Research Foundation, Kirtland Air Force Base, New Mexico, January 1962.
11. E. T. Selig, K. E. McKee, and E. Vey. "Underground Structures Subjected to Air Overpressure," Journal of the Engineering Mechanics Division, Proceedings of the ASCE, August 1960.
12. U.S. Army Corps of Engineers Waterways Experiment Station. Analysis and Design of Flexible Underground Structures, vol. II (1 May 1960), by N. M. Newmark, J. N. Brisco, and J. L. Merritt. Vicksburg, Mississippi. A report prepared by the University of Illinois under Contract DA-22-079-eng-225. CONFIDENTIAL

13. Air Force Special Weapons Center. Numerical Studies of the Dynamic Response of Shallow-Buried Arches Subjected to Blast Loading, by C. R. Whipple. Kirtland Air Force Base, New Mexico. A draft of a report prepared by the University of Illinois under Contract AF29(601)-25901. August 1961.
14. M. T. Davisson and H. L. Gill. "Laterally Loaded Piles in a Layered Soil System," a paper submitted to the Soil Mechanics and Foundations Division of ASCE, October 1962.
15. U. S. Department of Defense. The Effects of Nuclear Weapons, edited by Samuel Glasstone. Superintendent of Documents, U.S. Government Printing Office, Washington, D.C., April 1962.
16. K. Terzaghi and R. B. Peck. Soil Mechanics in Engineering Practice. New York, John Wiley & Sons, 1948.
17. E. Cohen and S. Weissman. "Underground Shock Environment Data and Application to the Design of Underground Structures," Bulletin no. 28, Shock, Vibration, and Associated Environments, part III September 1960, pp. 269-322.
18. K. Terzaghi. "Evaluation of Coefficients of Subgrade Reaction," Geotechnique, vol. 5, 1955.
19. U.S. Naval Civil Engineering Laboratory. Technical Note N-585: Static and Dynamic Shear Strength of Dry Sand, by R. L. Lytton and C. R. White. Port Hueneme, Calif., April 1964.
20. D. M. Burmister and R. D. Stoll. Static and Dynamic Response of Granular Soils. A report to the U. S. Naval Civil Engineering Laboratory under contract NBy-32198. Columbia University, New York, February 1963.
21. U.S. Naval Civil Engineering Laboratory. Technical Report R-126: Soil Stabilization by Vibration, by C.R. White. Port Hueneme, Calif., 13 March 1961.
22. U.S. Naval Civil Engineering Laboratory. Technical Note N-520: Investigation of a Technique for Placing Sand in the NCEL Blast Simulator, by J. P. Nielsen. Port Hueneme, Calif., 6 June 1963.
23. U.S. Naval Civil Engineering Laboratory. Technical Report R-277: Static and Dynamic Plate-Bearing Tests on Dry Sand Without Overburden, by C.R. White. Port Hueneme, Calif., 14 January 1964.

LIST OF SYMBOLS

		Dimension
A	area of soil between failure planes	L^2
a	constant exponent	-
b	footing width; one half of trapdoor width	L
a_1, b_1, c_1	constants depending on b/h	
$c, \bar{c}()$	constants	-
C_n	constant corresponding to nth mode	-
C_s	velocity of sound in the soil	LT^{-1}

	Dimension
c damping coefficient	$FL^{-2}T$
\bar{c} cohesion	FL^{-2}
$D_{()}$ linear dimensions	L
d_2 depth of cover	L
E modulus of elasticity	FL^{-2}
g acceleration of gravity	LT^{-2}
H footing depth	L
h depth of soil cover	L
I impulse for an element of area of unit width and length x	FTL^{-2}
\bar{I} moment of inertia of mass of the structure and soil acting with the structure in rotation	FT^2
$i_{()}$ impulse coefficient	dimensionless
k stiffness of foundation soil	FL^{-1}
\bar{k} coefficient of lateral earth pressure	dimensionless
k_z coefficient of subgrade reaction	FL^{-3}
k_1 subgrade modulus for a 1-foot width of footing	FL^{-3}
m mass of arch per unit length including ribs and footings	$FL^{-2}T^2$
m_e equivalent mass of soil acting with a footing per unit of length	$FL^{-2}T^2$
m_g mass of soil per unit length between failure planes ($t > t_\gamma$)	$FL^{-2}T^2$
m_1 mass of soil per unit length between failure planes ($t \leq t_\gamma$)	$FL^{-2}T^2$
p unit overpressure; unit load on plate or footing	FL^{-2}
\bar{p} average pressure over a distance along the surface between failure planes	FL^{-2}
p_0 peak overpressure	FL^{-2}
Q total load on a 1-foot length of the surface over the arch	FL^{-1}
r radius of arch	L
T_n natural period of n th mode	sec/cycle
t time	T
\bar{t} $t - t_\gamma$	T
$t_{()}$ time for shock front to reach various points on surface	T
t_d effective (triangular) duration	T

		Dimension
t_m	time to maximum footing deflection	T
c	velocity of air shock	LT^{-1}
V_1	total soil shear above the footing per foot of length on a vertical plane through the spring line	FL^{-1}
x	ph/yE	dimensionless
$x()$	distances along surface from origin of coordinate system	L
y	mean vertical displacement of footings, deflection of plate or trap door	L
y_b	total deflection of blastward footing	L
y_L	total deflection of leeward footing	L
y_m	maximum deflection of plate	L
y_o	footing deflection due to rotation	L
$\bar{y}()$	deflections due to long-duration loading	L
z	radial displacement of point on arch	L
α	angle of soil shear plane with horizontal	degrees
$\bar{\alpha}$	coefficient in displacement equations	T^{-2}
β	angle of soil stress front with horizontal	degrees
$\bar{\beta}$	coefficient in displacement equations	T^{-2}
γ	mass per unit of arc length	FT^2L^{-2}
γ_s	unit weight of soil	FL^{-3}
$\Delta I()$	impulse per unit of length transmitted to the soil-structure system	FTL^{-1}
ζ	translational damping factor	dimensionless
η_r	rotational damping factor	dimensionless
θ	angular displacement	radians
$\dot{\theta}_0$	initial angular velocity	radians/sec
λ_a	coefficient in equation for mass of soil between shear failure planes	-
$\lambda_i()$	(1, 1, 2,) coefficients in load relation	-
λ_d	coefficient in equations for initial velocity	-
ξ	nondimensional translation	-

	Dimension
U_0 initial translational velocity (nondimensional)	-
$\tau()$ nondimensional time	-
ϕ angle of internal friction of soil	degrees
ω natural translational frequency of soil-structure system	radians/sec
ω_n natural frequency of nth mode	radians/sec
ω_θ natural angular frequency of soil-structure system	radians/sec

BODY MOTION THEORY

by

J. R. Allgood and D. A. DeDeppo

INTRODUCTION

This appendix presents an approximate method for determining the deflections of the footings of a buried arch subjected to blast loading. The method presented is in a form suitable for use by the designer.

The foundation of a buried structure must be designed so that it has sufficient load capacity and also so that the deflections will not exceed some prescribed maximum value. Usually, it is specified that the maximum footing deflection shall be less than 2 inches. Limiting the deflections prevents rupturing the water seals and breaking fuel and other lines entering the shelter. Extreme deflections of the structure with respect to the floor could cause severe damage to partitions and internal fixtures and equipment. Multiple loadings, also, could cause undesirably large accumulative deflections. These factors justify the logic of limiting maximum deflections from a single loading to less than 2 inches.

The problem is how to design the footings to assure against excessive deflections. A promising method has been proposed,¹⁰ but it presupposes that the load on the footing is known. Determination of the load is one of the more difficult aspects of the problem. A method also has been proposed which, in effect, permits determination of the load on a buried structure,¹¹ but it does not account for the traveling characteristics of the blast. Refinements to the latter method have been proposed which are intended to more accurately account for the stress-strain characteristics of the soil.¹² The development presented here attempts to provide a means for determining the loading under traveling-wave conditions. With the loading known, prediction of deflection becomes more realistic.

The following treatment is limited to shallow-buried arches, however, with minor modifications, the method may be readily adapted to other geometrical forms. These shelters are presumed to be in overpressure regions of the order of 100 psi, although refinements are suggested for adapting the method to higher overpressure regions.

FUNDAMENTAL CONSIDERATIONS

The system under study is shown schematically in Figure A-1a. As an air shock travels across the surface, stress waves are induced in the soil field. For purposes of this report, all induced waves except the dilatational wave are assumed random and negligible. This includes the shear wave which lags the compression wave by a very few milliseconds at shallow depths. The air-induced dilatational wave front is taken as a plane perpendicular to the direction of travel of the stress wave and inclined at an angle, β , with the horizontal.¹³ As the wave travels downward through the soil, dispersion takes place and the rise time of the front increases. For this reason, it is referred to as a stress wave and not as a shock wave.

As the wave front envelops the structure, it would be expected that, if the overpressure is large enough, shear planes would form as indicated in Figure A-1b. This presumes that the compliance of the arch-foundation system is less than that of the surrounding soil. The breadth of the mass between the failure planes would increase with time, as shown in Figure A-1c, until the structure was completely enveloped. Thereafter, a rapid transition would ensue and the failure planes for the remainder of the loading would shift to a nearly vertical position as indicated in Figure A-1d.

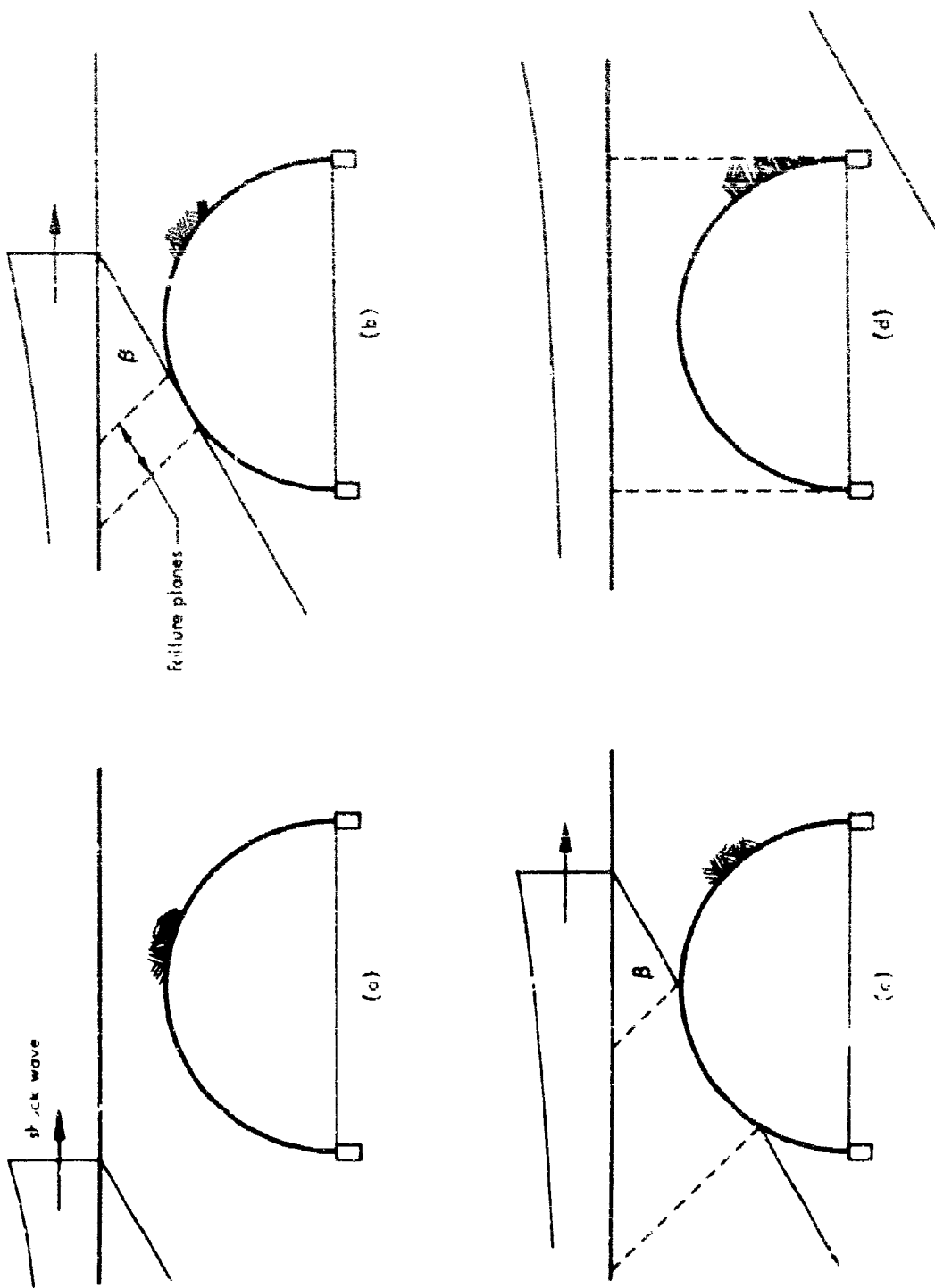


Figure A-1. Buried arch subjected to blast.

Equations expressing the variable breadth mass for inclusion in the equations of motion become untidily involved. Also, accounting for the variation of shearing resistance of the soil with depth, as has been done in other studies,¹⁴ complicates formulation of the problem. The latter refinement is unwarranted for shallow-buried structures since the normal pressure due to depth of cover is small compared to the normal pressure induced by the surface overpressure. To eliminate these and other complexities and reduce the system to a reasonable yet readily tractable model, a number of simplifying assumptions were introduced.

The basic assumptions were as follows:

1. The applied blast load can be represented by an equivalent triangular load.
2. The effect of the stress wave traversing the structure is equivalent to an impulse which imparts an initial translational and angular velocity to the structure.
3. The structure undergoes purely rigid body motions insofar as determining the deflection of the footings is concerned.
4. The mass of soil between the failure planes can be treated as a rigid body of constant breadth.
5. The soil constitutes an elastic homogeneous half-space. This only implies that the soil is elastic in compression; it is not considered to have any recovery ability.

Justification for all of the assumptions except the last one is fairly obvious, but number 5 warrants further consideration. It is accepted procedure that the foundation soil must be densely compacted prior to casting the footings. For dense granular materials, the stress-strain curve is such that in most cases the tangent modulus can be employed in calculations when the stress is less than about one-half of the ultimate stress. For stresses greater than one-half of the ultimate stress, assumption 5 results in large errors unless a secant modulus is employed or the theory is modified to account for the nonlinearity of the stress-strain properties of the soil. Experience with laterally loaded piles indicates that such refinement is not usually justified and that it is satisfactory to employ a secant modulus.¹⁴

In addition to the itemized assumptions, the conventional relations of static analysis are considered applicable to the soil. Also, the usual interrelations between blast parameters are employed.¹⁵

ANALYTICAL DEVELOPMENT

Procedure

There are two distinct phases of behavior of a shallow-buried arch: (1) the action during the time in which the stress wave is enveloping the arch, and (2) the motion thereafter. Developing relations to define the behavior in the second phase is relatively straightforward because the loading on the structure is symmetrical and directed vertically downward. It is apparent that if the initial translational and rotational velocities, due to the behavior in the first phase, could be determined, a solution could be achieved.

During the first phase, the load imparted to the arch may be considered as an impulse because of the short time required for the stress wave to envelop the structure. This fact is utilized in determining the initial velocities for the second phase solution. The procedure is as follows:

1. Needed geometrical relations are written.
2. The impulse is determined.
3. Initial velocities are derived.
4. An appropriate load function is set down.
5. A relation for the resistance is developed.
6. The equations of motion are formulated and solved.

Geometrical Relations

From Figure A-2, the geometrical relations of the system may be determined. In these relations and in Figure A-2, β is the angle which the stress front makes with the horizontal and α is the angle that the failure planes D and D_2 make with the vertical. The failure planes form an angle of $45^\circ + \phi/2$ with the horizontal¹⁶ where ϕ is the angle of friction of the soil. Linear dimensions on the surface of the soil are designated by x 's with subscripts; D 's with subscripts define distances in the soil mass. The radius of the semicircular arch and the depth of cover over the crown are designated by r and d_0 , respectively.

The basic geometrical relationships are:

$$D = (r + d_0) \sec \alpha - r \tan \alpha$$

$$D_1 = (r + d_0) \csc \beta - r \sin \alpha / \sin \beta$$

$$D_2 = (r + d_0) \sec \alpha$$

$$D_3 = (r + d_0) \csc \beta - r \cot \beta$$

$$D_4 = r + r \sin (\beta - \alpha)$$

$$D_5 = r \tan \alpha$$

$$x_1 = (r + d_0) \tan \alpha$$

$$x_2 = 2r + (r + d_0) \tan \alpha$$

$$x_\alpha = r (1 + \cos \alpha) / \cos \alpha$$

$$x_\beta = r (1 - \tan \beta / 2 + \tan \alpha) + d_0 (\tan \alpha + \cot \beta)$$

$$x_\gamma = r [1 + \cos \alpha + \tan \alpha + (1 - \sin \alpha) \cot \beta] + d_0 (\tan \alpha + \cot \beta)$$

Nondimensional plots for finding magnitudes of the parameters x_β and x_γ in terms of the angles α and β are given in Figures A-3, A-4, and A-5. These figures materially aid computation.

It has been tentatively concluded that for shallow depths, "the shock front (stress wave) in soil may be considered as a plane perpendicular to the direction of travel of the shock wave and inclined at an angle, β , with respect to the horizontal as given by the equation

$$\beta = \arcsin \frac{C_s}{U} \text{ when } \frac{C_s}{U} \leq 1$$

$$\beta = \frac{\pi}{2} \text{ when } \frac{C_s}{U} > 1$$

(A-1)

where C_s = seismic velocity of the soil

U = velocity of the shock wave in air at the point of interest.¹³

Plots of shock velocity in air for a given overpressure are readily available¹⁵ as is information on the seismic velocity of soils.¹⁷ The velocity of the stress front may be taken equal to the seismic velocity of the soil for the range of overpressure of interest.

As previously implied, α is calculable from the relation $\alpha = 45^\circ - \phi/2$. These are all of the basic geometrical relations necessary to the solution.

Determination of Impulse

Consider the impulse of the load acting on the mass between the failure planes, Figure A-2, as the soil stress wave travels the distance D_4 . The pressure at any point, x , behind the shock front is

$$p(x, t) = p_0 f(\xi) \quad (A-2)$$

$$\xi = t - \frac{x}{U} \quad (A-3)$$

where U = velocity of the air shock

t = time; $t = 0$ at $x = 0$

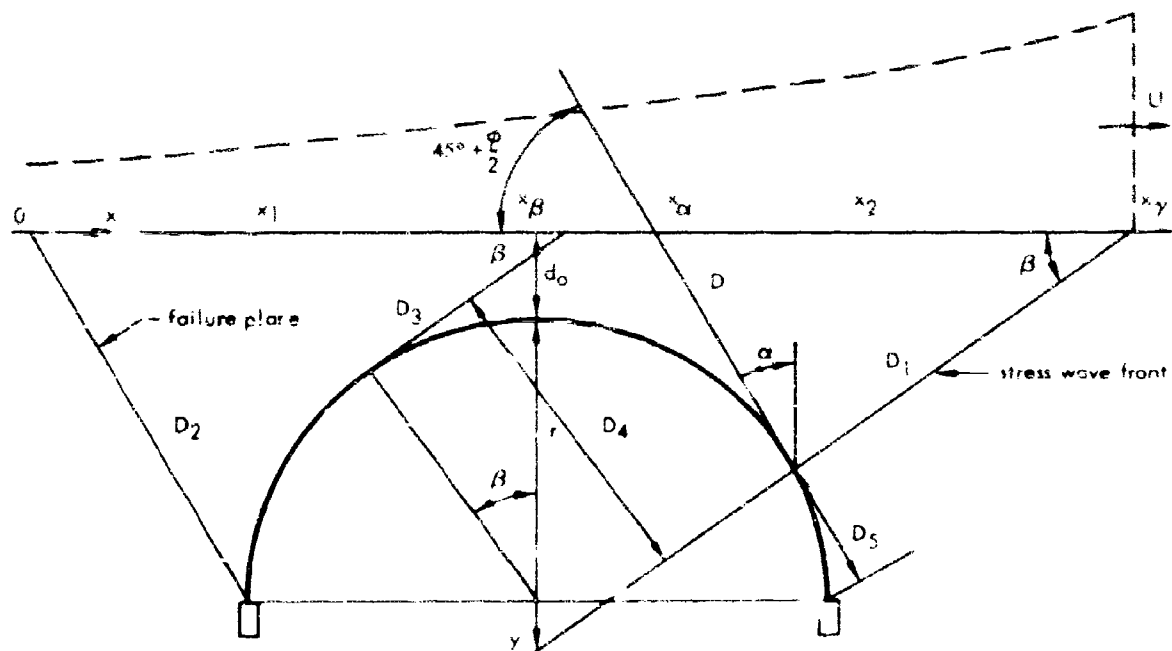


Figure A-2. Geometry of system.

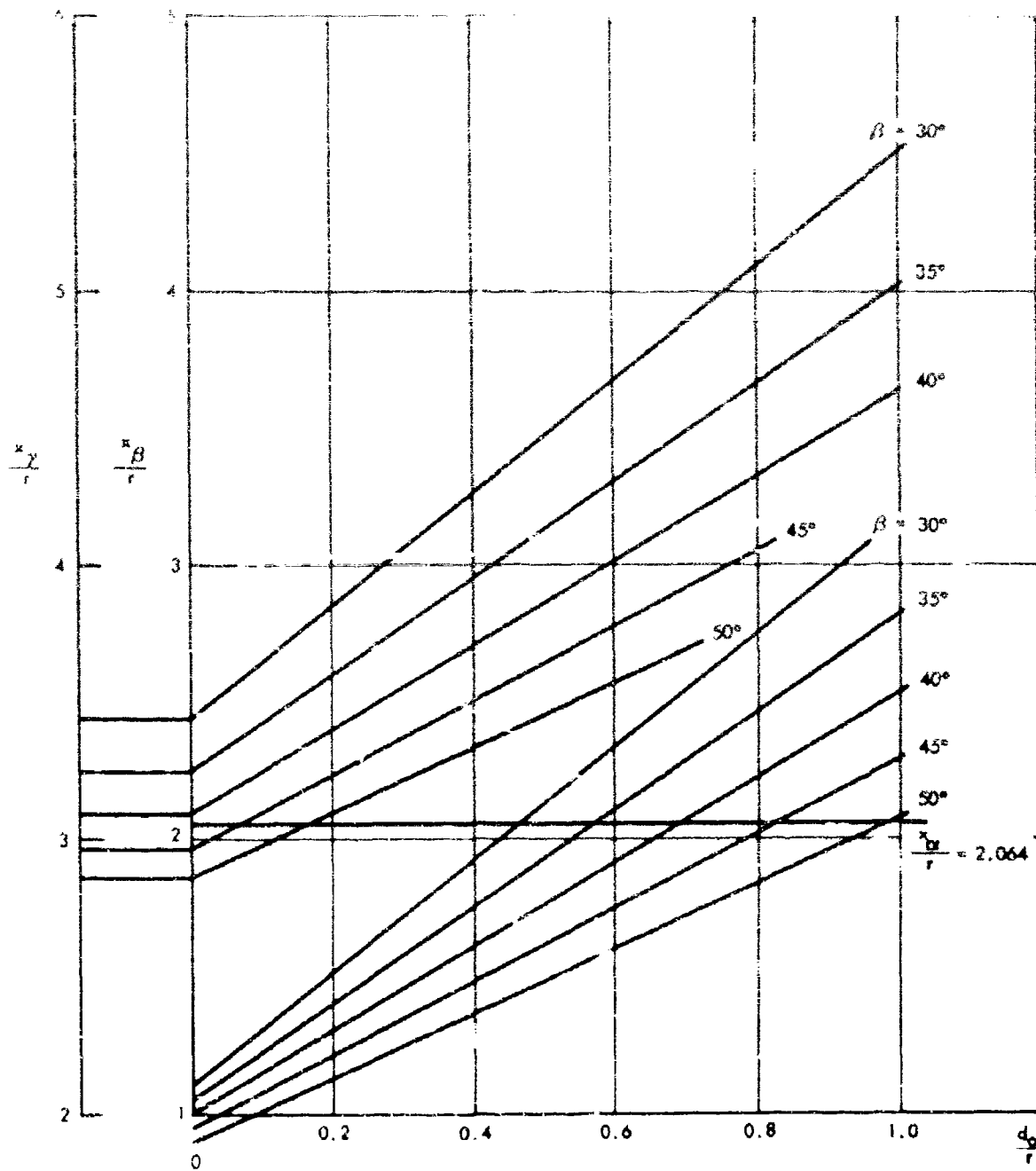


Figure A-3. Chart for determining x_γ and x_β ; $\alpha = 20^\circ$.

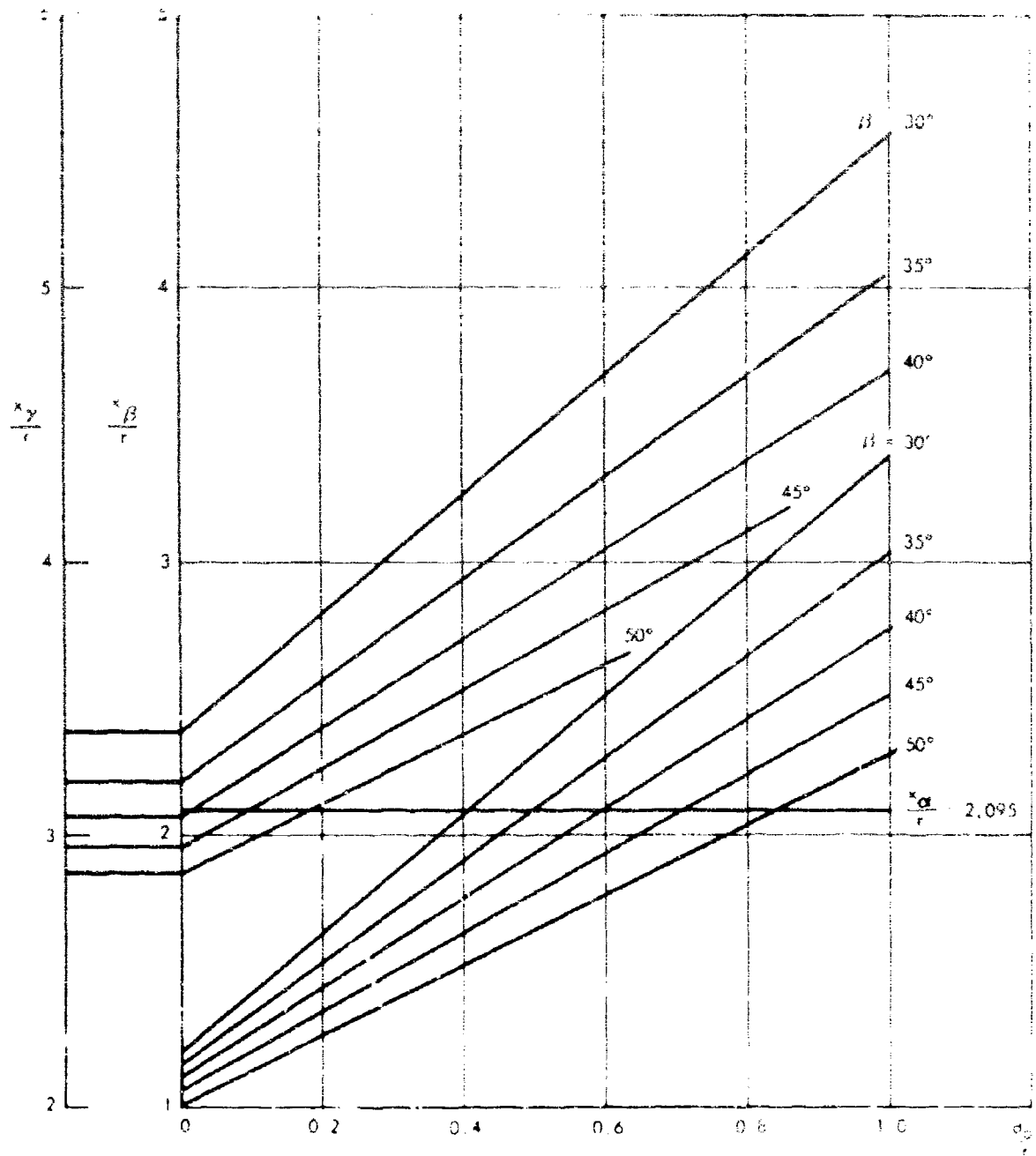


Figure A-4. Chart for determining x_Y and x_B ; $\alpha = 25^\circ$.

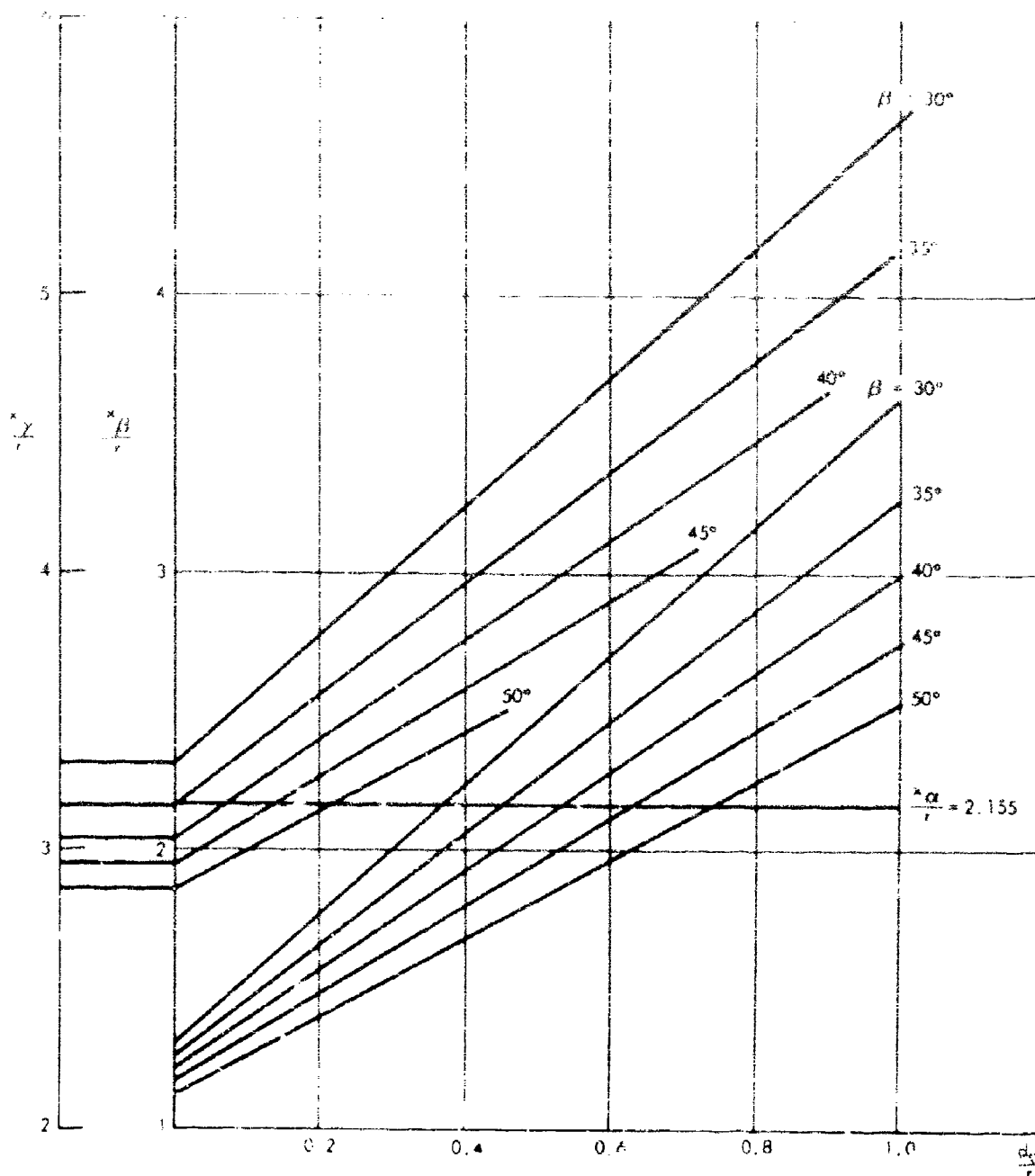


Figure A-5. Chart for determining x_γ and x_β ; $\alpha = 30^\circ$.

The total impulse of the load per unit of surface area at any point x behind the shock front at time t is

$$\frac{dI}{dx} = p_0 \int_0^{t - \frac{x}{U}} f(\xi) d\xi \quad (A-4)$$

Hence, for an element of area of unit width and length x , the total impulse is

$$I = p_0 \int_0^x \int_0^{t - \frac{y}{U}} f(\xi) d\xi dy \quad (A-5)$$

Since an equivalent triangular loading of duration t_d has been assumed

$$f(\xi) = 1 - \frac{\xi}{t_d} \quad \xi \leq t_d \quad (A-6)$$

Substituting Equation A-6 in Equation A-5 and evaluating the integral gives

$$I = p_0 \left[tx - \frac{x^2}{2U} - \frac{1}{2t_d} \left(t^2 x - \frac{tx^2}{U} + \frac{x^3}{3U^2} \right) \right] \quad (A-7)$$

This is more simply expressed by letting

$$\left. \begin{aligned} \tau_x &= \frac{x}{Ut_d} \\ \tau &= \frac{1}{t_d} \end{aligned} \right\} \quad (A-8)$$

Then the impulse becomes

$$I = \frac{p_0 Ut_d^2}{6} \left(6\tau\tau_x - 3\tau_x^2 - 3\tau^2\tau_x + 3\tau\tau_x^2 - \tau_x^3 \right) \quad (A-9)$$

The impulse transmitted to the soil-structure system as the soil-stress wave travels the distance D_4 is

$$\left. \begin{aligned} \Delta I_1 &= I(x_\alpha, t_\gamma) - I(x_\alpha, t_\beta) \text{ if } x_\beta > x_\alpha \\ \Delta I_2 &= I(x_\alpha, t_\gamma) - I(x_\beta, t_\beta) \text{ if } x_\beta < x_\alpha \end{aligned} \right\} \quad (A-10)$$

Designating τ_x as τ_α , τ_β , or τ_γ when $x = x_\alpha$, x_β , and x_γ , and noticing that $t/t_d = x_\alpha/U_d t_d$ when $t = t_\alpha$, etc., the transmitted impulse for $\tau_\beta \geq \tau_\alpha$ becomes

$$\Delta I_1 = \frac{p_0 U_d^2}{6} \left[\tau_\alpha (\tau_\gamma - \tau_\beta) (6 - 3\tau_\gamma - 3\tau_\beta + 3\tau_\alpha) \right] \quad (A-11)$$

and for $\tau_\beta < \tau_\alpha$

$$\Delta I_2 = \frac{p_0 U_d^2}{6} \left[6\tau_\gamma \tau_\alpha - 3\tau_\alpha^2 - 3\tau_\gamma^2 \tau_\alpha + 3\tau_\gamma \tau_\alpha^2 - \tau_\alpha^3 - 3\tau_\beta^2 + \tau_\beta^3 \right] \quad (A-12)$$

Or, more simply

$$\Delta I = \frac{p_0 U_d^2}{6} i \quad (A-13)$$

where $i = i_1$ when $\tau_\beta > \tau_\alpha$

$i = i_2$ when $\tau_\beta < \tau_\alpha$

and i_1 and i_2 are, respectively, the terms in brackets in Equations 11 and 12. Charts for i_1 and i_2 are given in Figures A-6 through A-13.*

Formulation of Initial Velocities

Equations for the initial velocities may be formulated by equating the impulse given the system to the change in momentum. The only difficulty in accomplishing this is in deciding just what constitutes the system. Certainly the structure and the soil between the shear planes above the arch are a part of the system but that is not all; the soil in the neighborhood of the footings which acts with them must also be accounted for. Preliminary studies suggest that it is sufficient to take the effective mass as that of a cylinder with a section diameter four times the footing width.

The effective area of soil acting with the structure is indicated in Figure A-14 together with the coordinates employed in the impulse-momentum equations. These equations for the initial velocities are

$$m_1 \dot{x}_0 = \Delta I \cos \alpha - N \dot{x} \quad (A-14)$$

$$(m + 2m_e) \dot{y}_0 = N \dot{x} \cos \alpha \quad (A-15)$$

*Linear interpolation between these charts may result in significant error.

$$\ddot{\theta}_0 = rNd^3 \sin(\beta - \alpha) \quad (A-16)$$

where m_1 = mass of soil between the failure planes

m_e = effective mass of soil acting with a footing as shown in Figure A-14

N = resultant force on arch

I = mass moment of inertia of arch and soil acting with the arch in rotation

The resultant force on the arch, N , is assumed to act at the point at which the stress wave first contacts the extrados. Under this assumption, the extremes of the region and line of action of the force are as indicated in Figure A-15. As shown, the extremes of the angle of friction of soil are taken as 25 and 45 degrees and the extremes of the angle β are taken as 14 and 39 degrees. These ranges are applicable for the overpressure region from 100 to 200 psi.

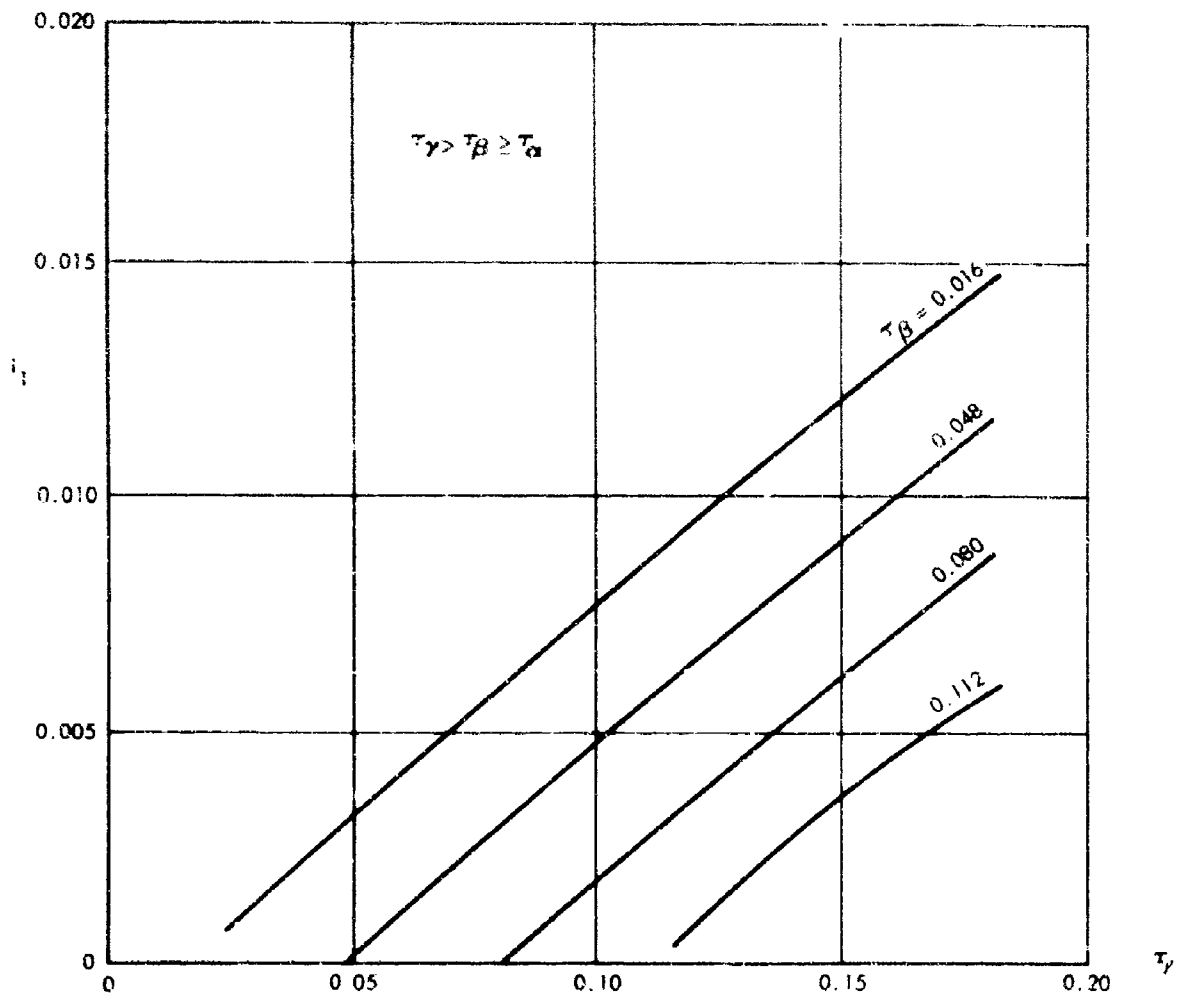


Figure A-6. Impulse chart, $\tau_\alpha = 0.016$.

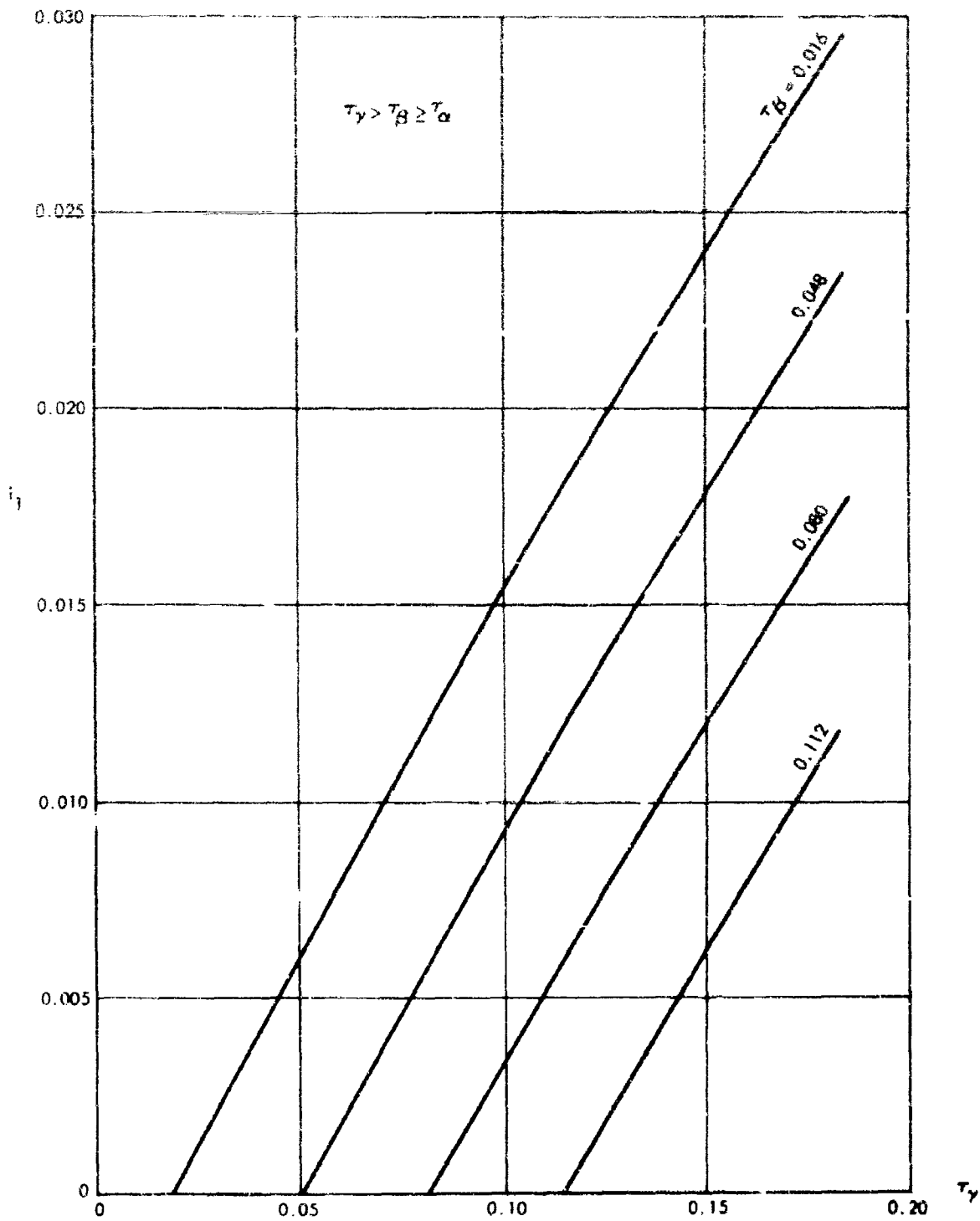


Figure A-7. Impulse chart, $\tau_\alpha = 0.032$.

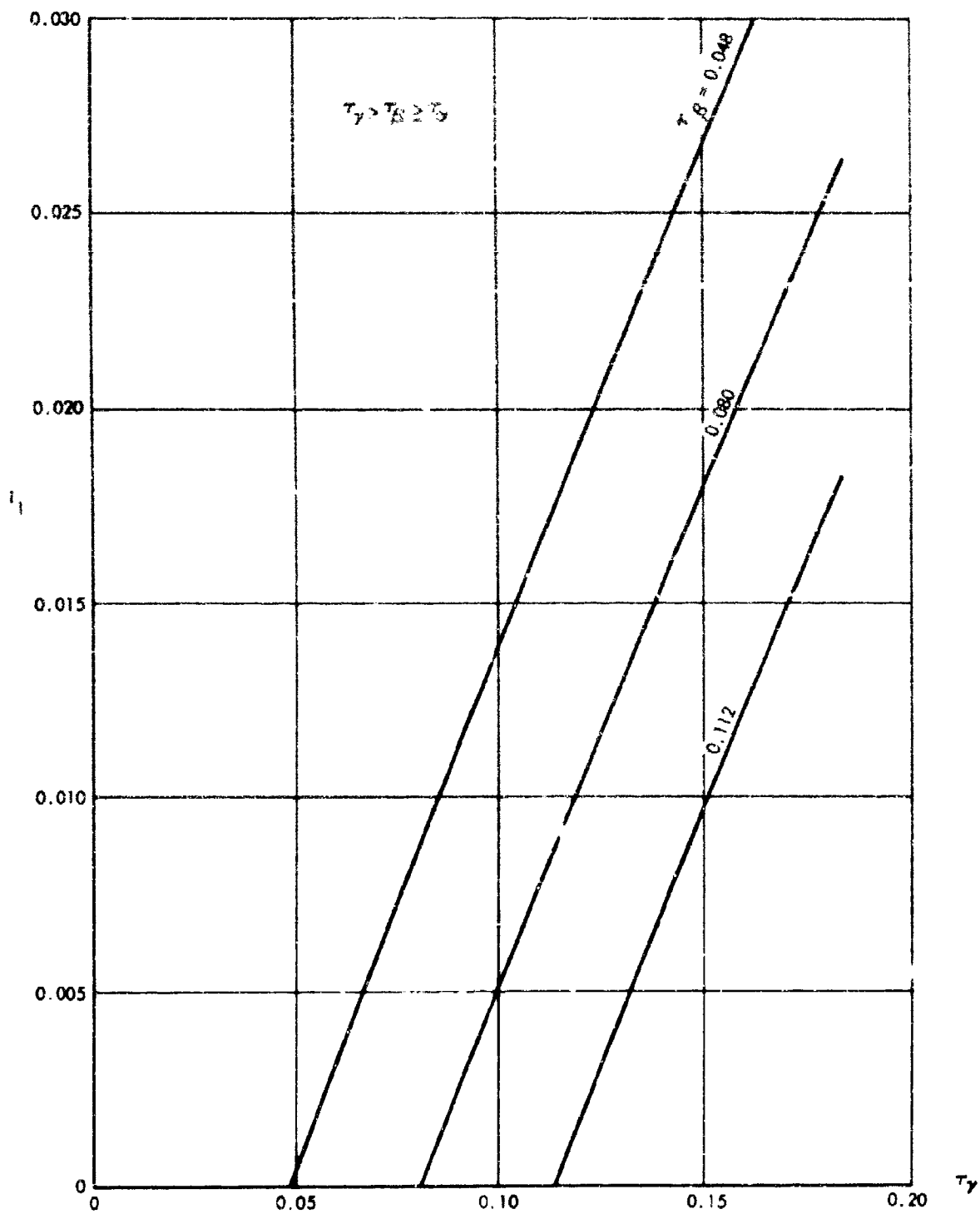


Figure A-8. Impulse chart, $\tau_\alpha = 0.048$.

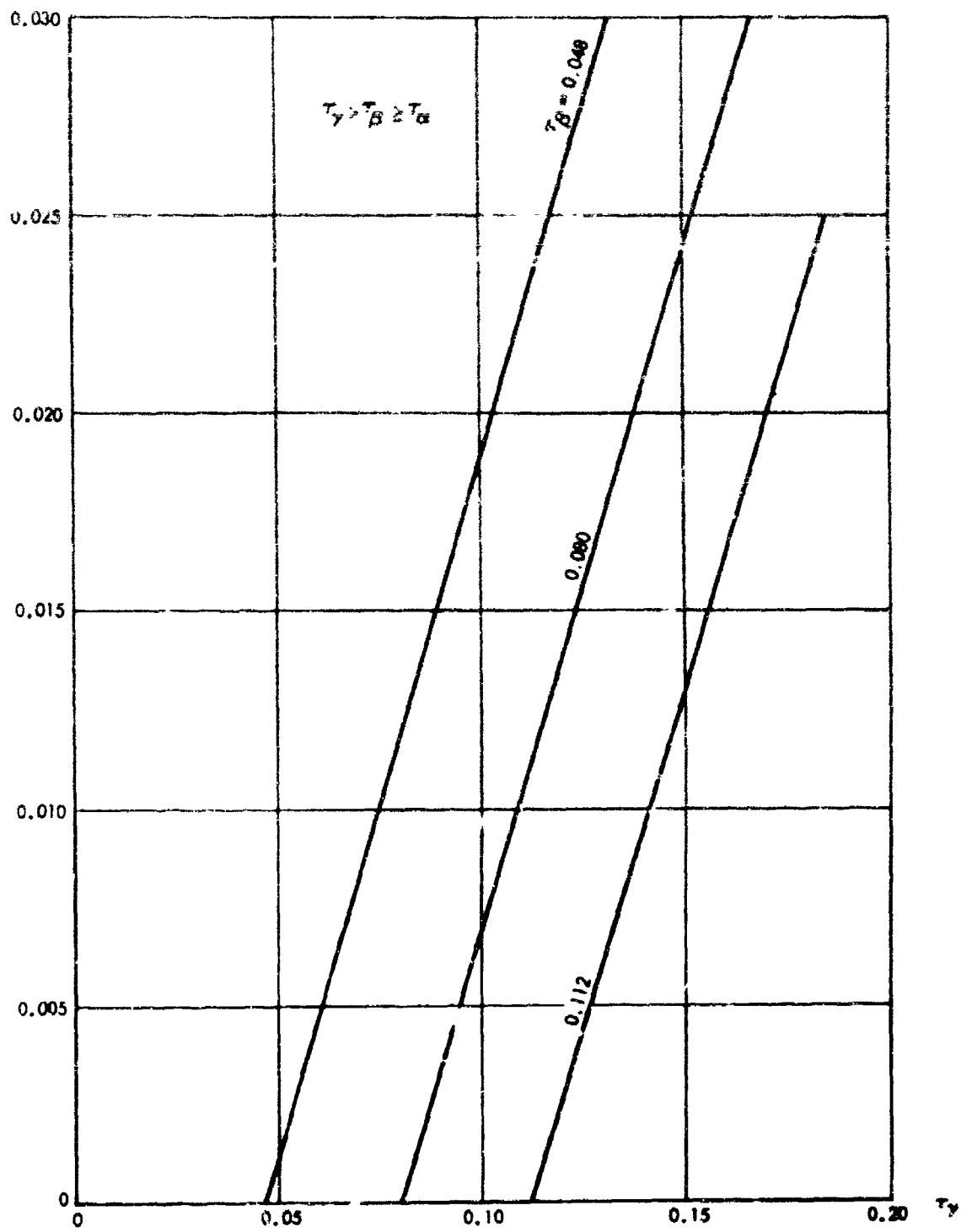


Figure A-9. Impulse chart, $\tau_\alpha = 0.064$.

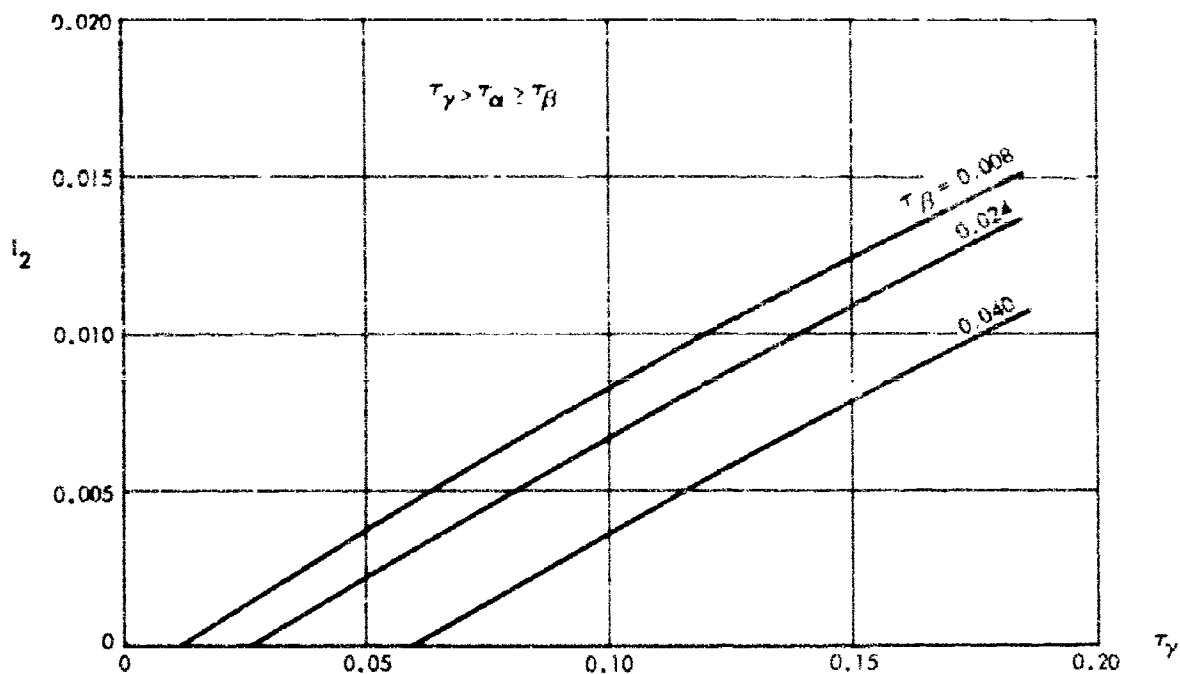


Figure A-10. Impulse chart, $\tau_{\alpha} = 0.016$.

In Equation A-14, the mass of soil between the failure planes is

$$m_1 = \frac{\gamma_s A}{g} \quad (\text{A-17})$$

where γ_s = weight of soil per unit of volume

A = area of vertical section of soil mass between the failure planes

This area may be expressed as

$$A = r_{\alpha} (r + d_0) - \frac{(\pi - \alpha) r^2}{2} - \frac{r D_5}{2}$$

or more conveniently

$$A = r^2 \left[\left(\frac{1 + \cos \alpha}{\cos \alpha} \right) - \frac{(\pi - \alpha)}{2} - \frac{\tan \alpha}{2} \right] + \frac{d_0 (1 + \cos \alpha)}{r \cos \alpha} \quad (\text{A-18})$$

$$A = r^2 \lambda_a$$

λ_a being the term in braces.

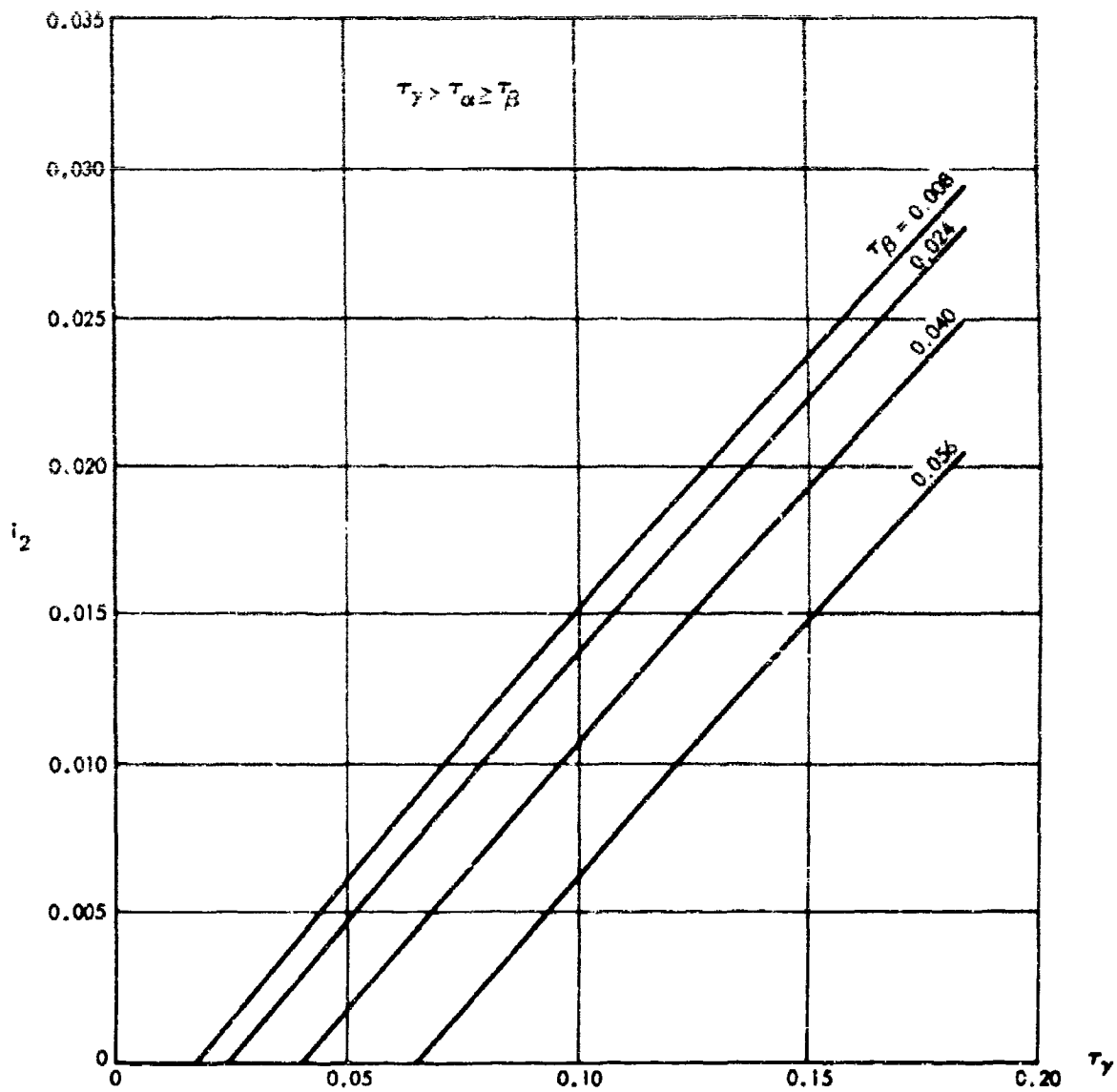


Figure A-11. Impulse chart, $\tau_\alpha = 0.032$.

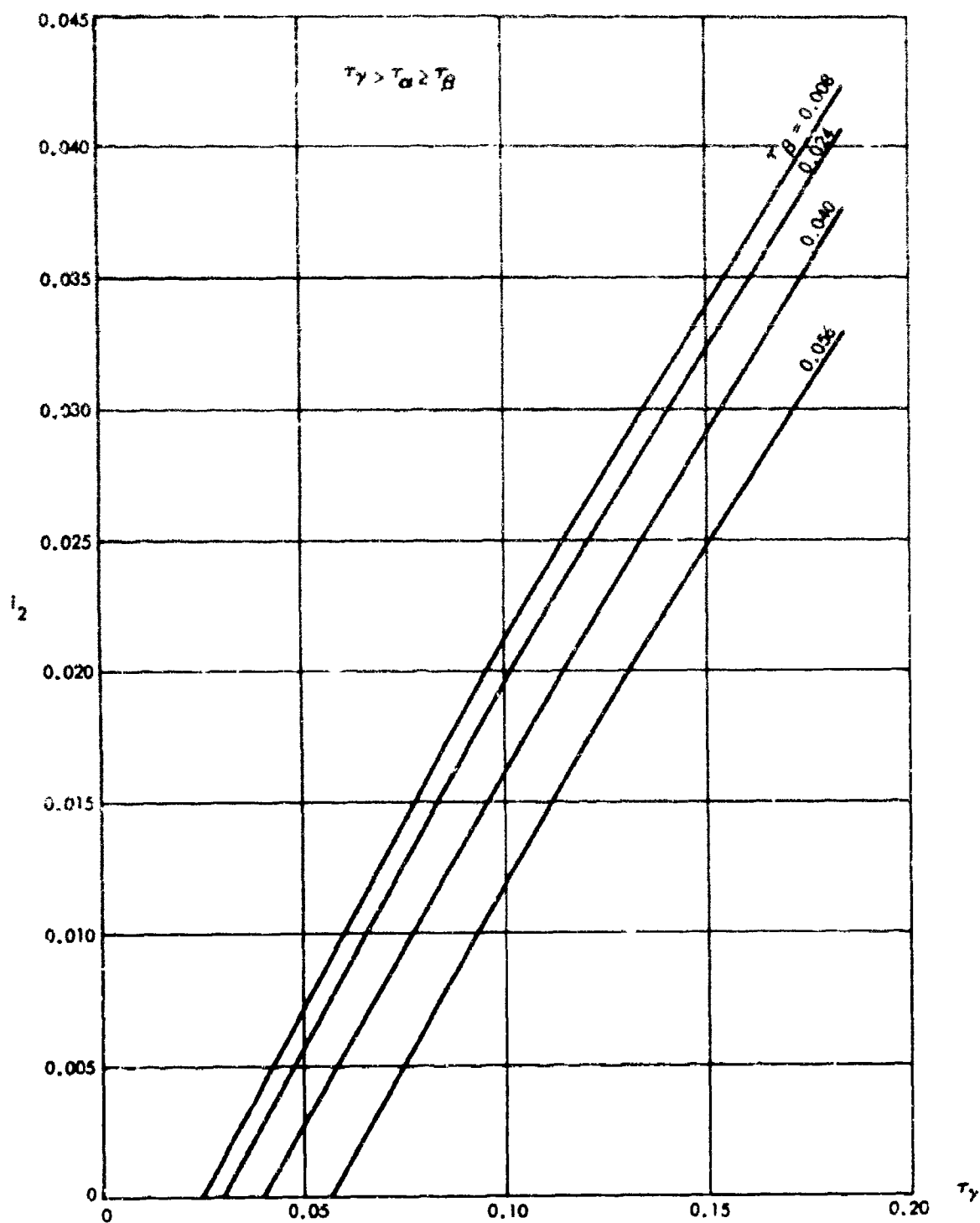


Figure A-12. Impulse chart, $\tau_\alpha = 0.048$.

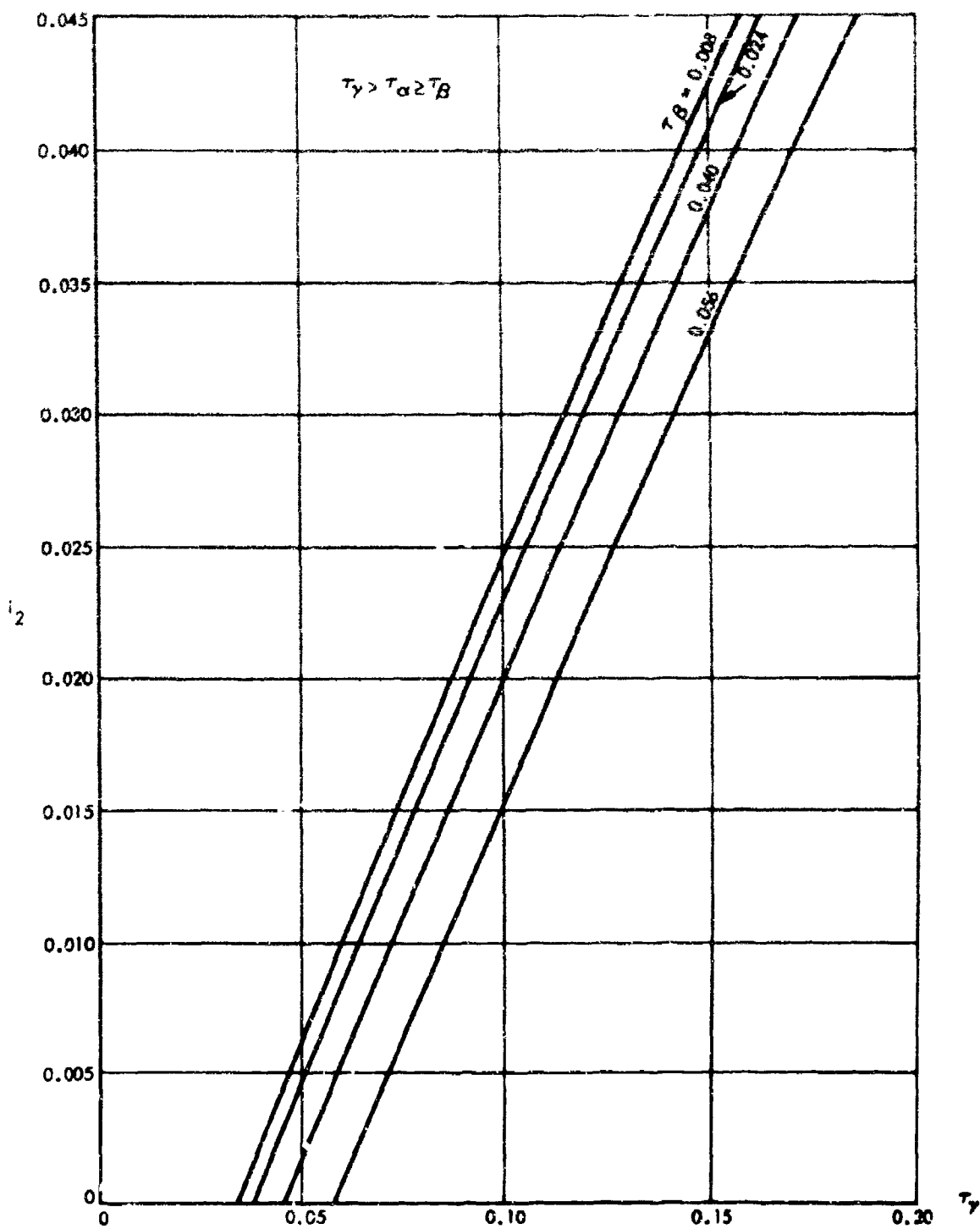


Figure A-13. Impulse chart, $\tau_\alpha = 0.064$.

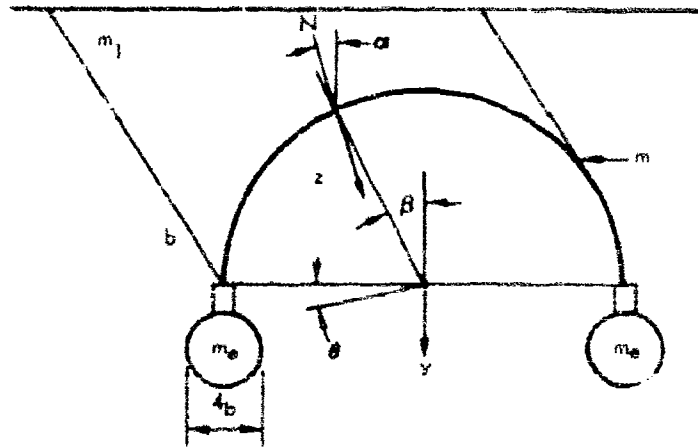


Figure A-14. System with coordinates.

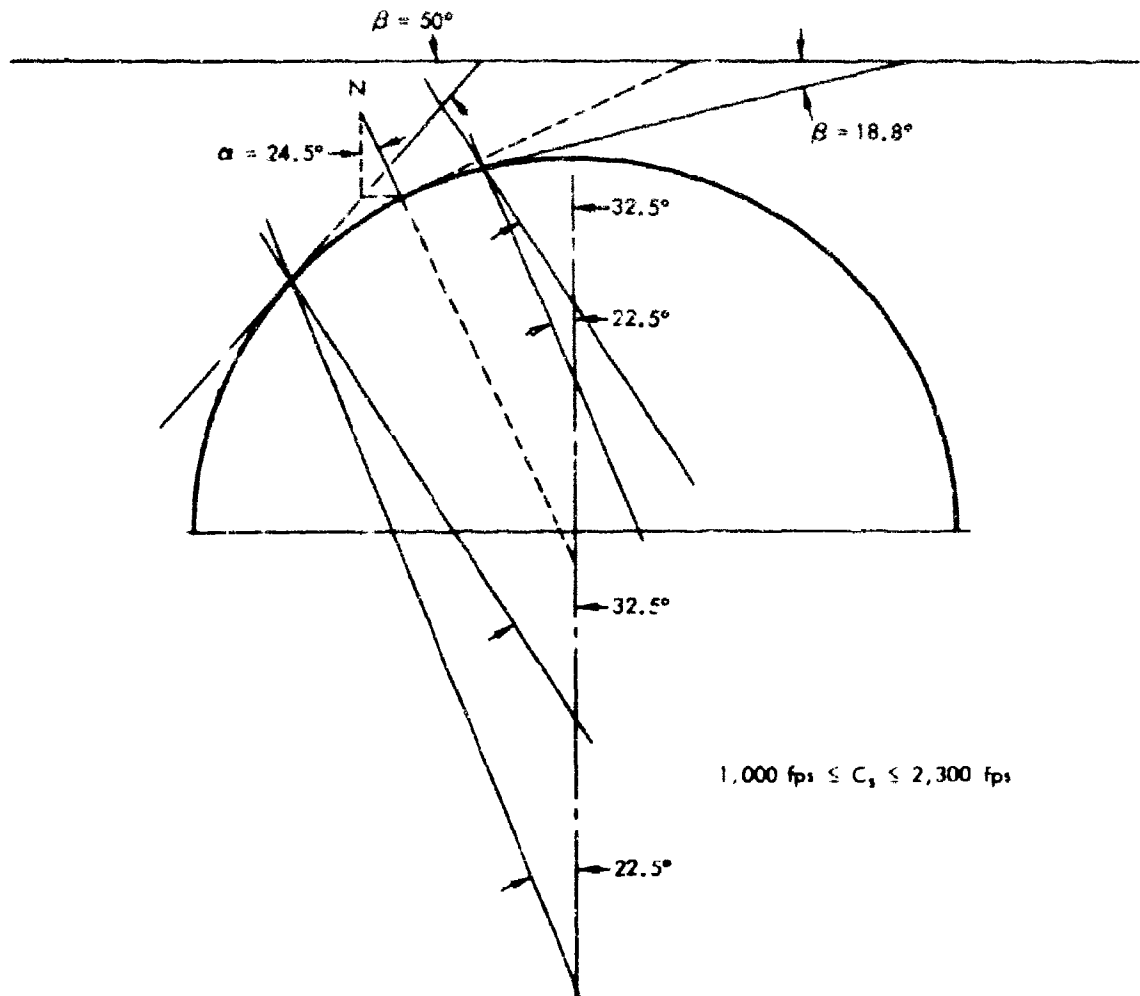


Figure A-15. Region and line of action of resultant force for 150-psf overpressure.

There is a simple geometrical relationship between z , θ , and γ from which we obtain

$$\dot{z}_0 = \dot{\gamma}_0 \cos \alpha + \dot{\theta}_0 r \sin(\beta - \alpha) \quad (\text{A-19})$$

Using this relationship, solving for Ndt from Equation A-14, and substituting it in Equations A-15 and A-16 yields the set of equations

$$\left(m + 2m_e + m_1 \cos^2 \alpha \right) \dot{\gamma}_0 + \left[m_1 r \cos \alpha \sin(\beta - \alpha) \right] \dot{\theta}_0 = \Delta I \cos^2 \alpha \quad (\text{A-20})$$

$$\left[m_1 r \cos \alpha \sin(\beta - \alpha) \right] \dot{\gamma}_0 + \left[I + m_1 r^2 \sin^2(\beta - \alpha) \right] \dot{\theta}_0 = r \Delta I \sin(\beta - \alpha) \cos \alpha \quad (\text{A-21})$$

Solution of these equations is readily accomplished by determinants to give

$$\dot{\xi}_0 = \frac{\dot{\gamma}_0}{r} = \frac{\Delta I}{rm_1} \left[\frac{\cos^2 \alpha}{\frac{m + 2m_e}{m_1} + \cos^2 \alpha + \frac{r^2 (m + 2m_e) \sin^2(\beta - \alpha)}{I}} \right] \quad (\text{A-22})$$

$$\dot{\theta}_0 = \frac{\Delta I}{rm_1} \left\{ \frac{\sin(\beta - \alpha) \cos \alpha}{\frac{I}{(m + 2m_e)r^2} \left[\frac{m + 2m_e}{m_1} + \cos^2 \alpha + \frac{r^2 (m + 2m_e) \sin^2(\beta - \alpha)}{I} \right]} \right\} \quad (\text{A-23})$$

For practical purposes, the center of gravity of the mass of the arch and the effective footing soil is concentrated at the distance r from the center of curvature of the arch, thus, $I = (m + 2m_e)r^2$. Using this relation, the denominators in the preceding two equations have the common term

$$\lambda_d = \frac{1}{\frac{m + 2m_e}{m_1} + \cos^2 \alpha + \sin^2(\beta - \alpha)} \quad (\text{A-24})$$

Utilizing Equations A-13, A-17, and A-18 with Equation A-24, Equations A-22 and A-23 may be expressed as

$$\dot{\xi}_0 = \frac{p_0 U t_d^2 g}{6 \gamma_s r^3} \left(\frac{\gamma_d}{\gamma_s} \right) \lambda_d \cos^2 \alpha \quad (\text{A-25})$$

$$\dot{\theta}_0 = \frac{p_0 U t_d^2 g}{6 \gamma_s r^3} \left(\frac{\gamma_d}{\gamma_s} \right) \lambda_d \cos \alpha \sin(\beta - \alpha) = \dot{\xi}_0 \frac{\sin(\beta - \alpha)}{\cos \alpha} \quad (\text{A-26})$$

These are the velocities needed to solve the equations of motion governing the second phase of behavior.

Second Phase Motion

In formulating equations of motion, the important factors influencing deflection of the foundation must be determined. It has been suggested that it is necessary to consider the stress wave generated by the footings to get a realistic prediction of the motion.¹⁰ One line of reasoning indicates that this is not true.

Tests on buried model arches⁹ show that the time to maximum displacement of the structure is far in excess of the time required for the soil stress wave to propagate beyond the region occupied by the arch. Thus, a solution sufficiently accurate for design purposes should be obtainable without considering wave propagation.

The dominant parameters are thought to be those indicated in the model of Figure A-16. An equation of motion and a solution for this model can be developed if the effective mass which acts with the footing, an appropriate foundation modulus, and a suitable damping coefficient are available. At present, there is no comprehensive information on these quantities, however, analysis utilizing extensive dynamic footing test data is being made at the Waterways Experiment Station to determine the character of these parameters. It is expected that the effective mass, the foundation modulus, and possibly the damping may be functions of displacement and time. For purposes of the present development, nevertheless, these parameters will be considered as constants.

As discussed later, some pertinent information is available concerning damping, and methods are available for computing the modulus of subgrade reaction. Expressions for Q and V_1 also will be required to complete the equations of motion. In the following paragraphs the equations of motion are presented with each of the cited factors considered in turn.

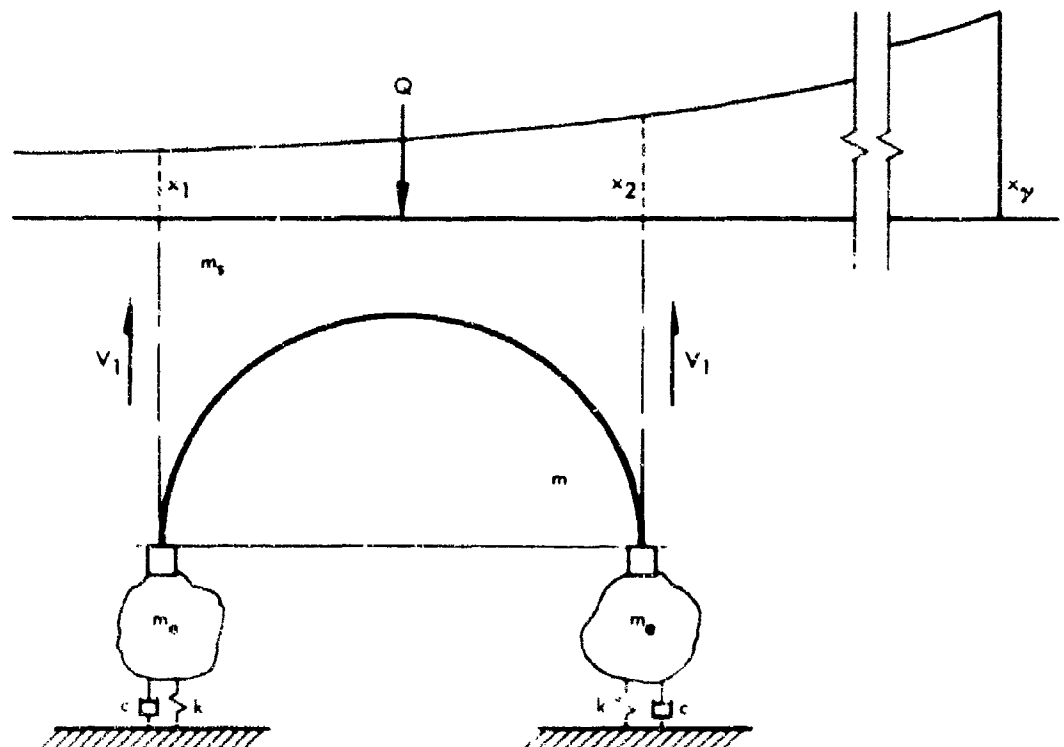


Figure A-16. Model for buried arch.

Equations of motion for $t > t_y$. With $y = r\dot{\xi}$ and $k = bk_s$, the equation of vertical motions is

$$(m + m_s + 2m_e) \ddot{\xi} + 2c\dot{\xi} + 2k\xi = \frac{Q - 2V_1}{r} \quad (A-27)$$

$$m_s = \frac{2\gamma_s r^2}{g} \left[\left(1 + \frac{d_0}{r} \right) - \frac{\pi}{4} \right] \quad (A-27a)$$

Here, the arch is assumed to be sufficiently long so that the influence of the end wall foundation is negligible. For a short structure, the shear on the vertical planes of the end walls must be included.

Assuming that the mass of the system may be considered as acting at a distance r from the center of curvature of the undeformed arch

$$I\ddot{\theta} + 2cr^2\ddot{\theta} + 2kr^2\theta = 0 \quad (A-28)$$

With the relations

$$\omega^2 = \frac{2k}{m + m_s + 2m_e} \quad (A-29)$$

$$2\eta\omega = \frac{2c}{m + m_s + 2m_e}$$

and

$$\omega_\theta^2 = \frac{2k}{m + m_s + 2m_e} \quad (A-30)$$

$$2\eta_\theta\omega_\theta = \frac{2c}{m + m_s + 2m_e}$$

Equations A-27 and A-28 may be expressed as

$$\ddot{\xi} + 2\eta\omega\dot{\xi} + \omega^2\xi = \frac{Q - 2V_1}{r(m + m_s + 2m_e)} \quad (A-31)$$

$$\ddot{\theta} + 2\eta_\theta\omega_\theta\dot{\theta} + \omega_\theta^2\theta = 0 \quad (A-32)$$

It may be noted that $2m_e$ is used in Equation A-30 instead of m_e . This approximation simplifies subsequent relations but results in a negligible error because $m + m_g \gg m_e$. In these equations, η and η_θ are interrelated, however, because of the identical angular and translational frequencies

$$\eta = \eta_\theta \quad (\text{A-33})$$

It now becomes necessary to evaluate the undertermined parameters.

Load and soil shear. The driving force shown in Figure A-15 is

$$Q = 2x\bar{p} \quad (\text{A-34})$$

where \bar{p} = average pressure over x_1, x_2

The pressure at any point, x , behind the shock front for $t > t_y$ is

$$p(x, t) = p_0 \left(1 - \frac{t - t_x}{t_d} \right) \quad (\text{A-35})$$

Let $t = \bar{t} + t_y$, then

$$p(x, \bar{t}) = p_0 \left(1 - \frac{t_y}{t_d} + \frac{t_x}{t_d} - \frac{\bar{t}}{t_d} \right)$$

but

$$\frac{t_y}{t_d} = \tau_y \text{ and } \frac{t_x}{t_d} = \tau_x$$

hence

$$p(x, \bar{t}) = p_0 \left[\left(1 - \tau_y + \tau_x \right) - \frac{\bar{t}}{t_d} \right]$$

The average pressure over x_1, x_2 then is

$$\bar{p} = \lambda_t p_0 \left(1 - \frac{\bar{t}}{t_d \lambda_t} \right) \quad 0 \leq \bar{t} \leq t_d - t_y \quad (\text{A-36})$$

where

$$\lambda_t = 1 - \tau_y + \left(\frac{\tau_{x1} + \tau_{x2}}{2} \right) \quad (\text{A-36a})$$

Assume that, for the depths of burial of interest, the vertical soil stress equals the average surface pressure over the arch. The shearing force in the soil on a vertical plane through the spring line per unit of width is

$$V_1 = (\bar{c} + \bar{k} \bar{p} \tan \phi) (r + d_o) \quad (A-37)$$

where \bar{c} = soil cohesion

\bar{k} = the coefficient of lateral earth pressure

Thus, the numerator of the right side of Equation A-31 becomes

$$\begin{aligned} Q - 2V_1 &= 2r\lambda_t p_o \left(1 - \frac{\bar{f}}{t_d \lambda_t}\right) - 2r\bar{c} \left(1 + \frac{d_o}{r}\right) \\ &\quad - 2r\lambda_t p_o \left(1 - \frac{\bar{f}}{t_d \lambda_t}\right) \bar{k} \tan \phi \left(1 + \frac{d_o}{r}\right) \end{aligned} \quad (A-38)$$

Alternately expressed, Equation A-38 becomes

$$Q - 2V_1 = 2rp_o \left[(\lambda_t \lambda_1 - \lambda_2) - \lambda_1 \frac{\bar{f}}{t_d} \right] \quad (A-39)$$

where

$$\lambda_1 = 1 - \bar{k} \left(1 + \frac{d_o}{r}\right) \tan \phi \quad (A-40)$$

$$\lambda_2 = \frac{\bar{c}}{p_o} \left(1 + \frac{d_o}{r}\right)$$

Attention may now be directed to determination of the foundation modulus.

Foundation modulus. The foundation modulus is the ratio of the unit load on a footing to the total settlement of the footing and is commonly expressed by the relation¹⁸

$$k_z = k_1 \left(\frac{b+1}{2b} \right)^2 \quad (A-41)$$

where k_1 = the subgrade modulus for a footing width of one foot (usually determined from a plate bearing test); here the dynamic modulus with the appropriate surcharge pressure should be used.

b = footing width (ft)

With k_z , Q , and V_1 determined, all of the necessary quantities except the damping are available for the solution of Equations A-31 and A-32.

Damping. The model arch tests previously referred to² indicate that damping of the body motions is near critical. The oscillograms show that the structure deflected to a maximum value and experienced no further oscillation, although there was a small elastic recovery as the load was removed.

Measurements from the Operation Plumbbob 3.3 structures also indicate that the damping was near critical. For present purposes, therefore, it is considered sufficiently accurate to employ the solution of the equations of motion for critical damping.

Solution of Equations of Motion

With Equation A-39 in Equation A-31, the governing equations of motion are

$$\ddot{\xi} + 2\eta\omega\dot{\xi} + \omega^2\xi = \frac{2p_0}{(m + m_s + 2m_e)} \left[(\lambda_t\lambda_1 + \lambda_2) - \lambda_1 \frac{t}{t_d} \right] = \bar{\alpha} (1 + \bar{\beta}t) \quad (A-42)$$

$$\ddot{\theta} + 2\eta_\theta\omega_\theta\dot{\theta} + \omega_\theta^2\theta = 0 \quad (A-43)$$

with initial conditions

$$\xi(0) = \theta(0) = 0 \quad (A-44)$$

$$\dot{\xi}(0) = \dot{\xi}_0$$

$$\dot{\theta}(0) = \dot{\theta}_0$$

For $\eta = \eta_\theta = 1$, the formal solutions of these equations are

$$\xi = \frac{\bar{\alpha}}{\omega^2} \left(1 - \frac{2\bar{\beta}}{\omega} \right) (1 - e^{-\omega t}) + t \left[\frac{\bar{\alpha}\bar{\beta}}{\omega^2} + \left(\dot{\xi}_0 - \frac{\bar{\alpha}}{\omega} \left(1 - \frac{\bar{\beta}}{\omega} \right) \right) e^{-\omega t} \right] \quad (A-45)$$

and

$$\theta = \dot{\theta}_0 t e^{-\omega_\theta t} \quad (A-46)$$

where

$$\bar{\alpha} = \frac{2p_0 (\lambda_t\lambda_1 + \lambda_2)}{m + m_s + 2m_e} \quad (A-47)$$

$$\bar{\beta} = \frac{-\lambda_1}{t_d (\lambda_t\lambda_1 + \lambda_2)} \quad (A-48)$$

$$t = t - t_\gamma \quad t_\gamma \leq t \leq t_d \quad (A-49)$$

Equations A-45 and A-46 hold only for ξ and θ less than or equal to their initial maximum values because of the nonlinear character of the soil.

For the most severe load conditions, namely long-duration loading, it is possible to express the maximum deflection of the footings much more simply. Such a simplification is possible since the soil may be considered to have negligible recovery or rebound ability, especially at higher stresses. Because of this, it is possible to superimpose parts of the solution of the equations of motion by algebraic addition.

The response of the buried arch to a traveling wave may now be broken down into three parts. The response due to the load, with zero initial conditions, is essentially the peak deflection under a static load of the same peak magnitude. That is

$$y_{p(t) \max} = \frac{Q - 2V_1}{2k} - \frac{p_0 r - V_1}{k} \quad (A-50)$$

Differentiating Equation A-46 and equating the result to zero gives a time to maximum deflection of $1/\omega_\theta$. Substituting this in Equation A-46, the maximum displacement, $r\theta_{\max}$, caused by the initial angular velocity is

$$y_{\theta_0 \max} = \frac{r\dot{\theta}_0}{e\omega} \quad (A-51)$$

A similar expression results from Equation A-45 on employing the described procedure with $\alpha = 0$, thus, the maximum deflections of the footings for long duration loading may be expressed as

$$\bar{y}_{\max} = \frac{p_0 r - V_1}{bk_z} + \frac{\dot{y}_0}{e\omega} \pm \frac{r\dot{\theta}_0}{e\omega_\theta} \quad (A-52)$$

For short-duration loading, the deflection may be computed with the aid of Equations A-45 and A-46. Again, θ_{\max} and ξ_{\max} should be used so that

$$\bar{y}_{\max} = r\xi_{\max} \pm r\theta_{\max} \quad (A-53)$$

Relations A-52 and A-53 are readily evaluated once the initial velocities \dot{y}_0 and $\dot{\theta}_0$ have been determined. The impulse parameter in the expressions for the initial velocities, Equations A-25 and A-26, can be readily determined from the charts of Figures A-6 through A-13.

Discussion

Judgement regarding the influence of the dominant parameters is enhanced by a study of Equation A-52. It can be simplified by lumping those terms which are constant or only vary through a small range for the pressure regions of interest. Using this approach, for a cohesionless soil, the dominant translational part of the deflection can be expressed as

$$y'_{f_{\max}} \cong \frac{p_o}{2k_z} \left[1 - k \tan \phi \left(1 + \frac{d_o}{r} \right) + \frac{\sqrt{k_z}}{r^3} \frac{C}{\bar{C}_1 + \frac{d_o}{r} \bar{C}_2} \right] \quad (A-54)$$

Here it is seen that the footing deflection is primarily dependent upon the peak applied load, the foundation modulus, the angle of friction, the coefficient of lateral earth pressure, the radius of the arch, and the depth of cover over the crown. The manner in which these terms affect the deflection is fairly evident from Equation A-54.

The first two terms are approximately the deflection which would result from a static loading while the second term represents the contribution due to the dynamic nature of the loading. For a given subgrade modulus and depth of cover, the dynamic component decreases as the radius of the arch increases. This implies that, relatively speaking, the body motions are proportionately less for large structures than for small ones. The second term also shows that the subgrade modulus is not nearly as important in limiting the dynamic component as in reducing the static component of body deflection.

The complexity of the traveling-wave problem has necessitated making numerous assumptions to achieve a solution. Several of these assumptions are not validated by adequate experimental data and may require modification as better information becomes available. The development does offer a reasonable approach, however, to which refinement can be made as warranted. One requirement, which could easily and fruitfully be made when the depth of cover is more than a few feet, would be to employ the method of Reference 11 to replace Equation A-27 and its solution.

No attempt was made to determine the horizontal body motion of the structure since this deflection will generally be relatively small and of little consequence in the pressure regions considered, except possibly as input for shock isolation studies.

SUMMARY

The development presented permits achievement of an insight into the interrelation and influence of the dominant parameters controlling the body motions of a buried arch subjected to a traveling wave from a nuclear blast. Correlation of the theory with experimental results from the Operation Snowball Project 3.4 arches is given in the body of the report.

The method of this appendix should be considered as a first approximation for the prediction of body motions. Refinement of the theory to include the dependence of the arching shear on deflection and replacement of the constant coefficient of subgrade reaction with the dynamic load-deflection relation, as suggested in the main text, would refine the theory.

Appendix B
BACKFILL SOIL

by
L. W. Heller

REQUIREMENTS

The burial of the arches for Operation Snowball required that four flexible, 30-inch-diameter arches 5 feet long and eight flexible, 12-inch-diameter arches 2 feet long be encompassed within several fields of dry sand exhibiting consistent engineering properties. The dimensions of the excavated pits and the soil fields placed around the various arches are described in the main body of this report.

In order to compare the behavior of the 12 buried arches, it was necessary that each of the arches be embedded in a like manner and that the material surrounding each arch possess the same load-deformation characteristics. Some of the important properties of the in-place sand field required to insure similar engineering characteristics are as follows:

1. The sand should be kept air dry at all times. The influence of moisture on the dynamic properties of sand has been documented.¹⁹
2. The void ratio or density of the sand should be constant throughout the entire sand field. The density of a dry, homogeneous, particulate material greatly influences its engineering behavior.²⁰
3. In order to attain homogeneity throughout the artificially placed soil field, there must be no segregation of the sand grains. Segregation produces zones of potential failure interior to the sand field as well as altering its engineering properties.

METHODS OF CONSTRUCTING A SOIL FIELD

There are three primary methods of densifying an initially loose sand material into a condition suitable for engineering purposes namely, vibratory, tamping, and sieving methods.

1. Vibratory methods of densifying a dry granular material are described in Reference 21. Vibration is an excellent method of compacting roadbeds and fills when the loads on culverts placed in the roadbed or structures adjacent to the fill are not important. Segregation is an inherent, although often surmountable, difficulty in this method. A vibrator has been used in compacting a sand fill in previous NCEL tests.³

Because of the unrestrained flexibility of the arches, the absorption interface at the walls of the excavated pits, the reflection interface at the compliant face of the arch, and the possibility of grain-size segregation, the vibratory method appeared to be an undesirable means for constructing a homogeneous sand field.

2. Tamping methods can be used for the compaction of granular or cohesive materials whenever the moisture content of the material can be closely controlled and maintained at its optimum value. Such control at the test site would obviously be impossible without extensive earthwork equipment and laboratory testing.

Loads applied to the soil and thus to the unsupported flexible arches by the tamping action would be a second prohibitive disadvantage of this method.

3. Sieving methods for producing a dense granular structure have been used for laboratory studies in conjunction with small-scale tests.²² Sieving techniques appeared to offer several advantages over the previously enumerated densification methods for the circumstances involved in Operation Snowball.

When an air dry sand is used, a dense, uniform, and homogeneous soil field can be placed with none of the dynamic problems indigenous to the vibratory or tamping methods. Reported warm, dry weather conditions and the availability of unskilled labor for placing the soil material at the test site were further considerations favoring the sieving technique.

DEVELOPMENT OF SIEVING APPARATUS

The operating principles of the sieving method are quite simple. Sand is metered through a series of sieves to produce a randomly dispersed system of free-falling grains. The potential energy of each of these grains with respect to the impacting datum is expended as these grains strike the surface of the sand and seek their individual minimum energy positions.

A single-unit, developmental sieving device similar to that shown in Figure B-1 was fabricated and tested to determine the variables affecting the resultant sand densities. Length of conduit hose (B, figure B-1), height of drop to the sand surface, A, and rate of sand flow, Q, were the variables studied. With A = 18 inches, B = 7 feet, and Q = 0.5 cfm, the resulting density was 107.7 pcf. Changing A to 30 inches produced a density of 109.3 pcf. Figure B-2 illustrates the effect of flow rate and drop distance on the sand density produced when B is reduced to 2 feet. A 1-1/2-cubic foot container was used for these tests.

A single-unit, prototype developmental sieving device was moved outdoors, fitted with a 6-foot-long, 3-inch-diameter hose, and carefully calibrated with orifices of 3/4-, 1-, 1-1/4-, and 1-1/2-inch diameter. The flow rates and the resultant densities for this series of calibrations are given in Figure B-3. The densities obtained with this sieving apparatus using the 1-1/2-inch-diameter orifice were only slightly higher than those obtained by vibratory methods⁶ in the NCEL simulator pit. Two triple-unit sieving apparatus were designed and fabricated in a manner suitable for filling the NCEL blast simulator pit and the excavated pits for Operation Snowball.

Mr. R. C. Sloan of the Waterways Experiment Station, Vicksburg, Mississippi, and Mr. B. A. Donnellan of the Air Force Shock Tube Facility, Albuquerque, New Mexico, provided the concepts for the valving and sieving components of the NCEL sieving apparatus.

PROOF TESTS

Proof tests were conducted in the blast simulator pit at NCEL to determine if NCEL test sand could be placed in this facility by the sieving method at a density comparable to that previously obtained by vibratory methods.³ Figure B-4 shows the multiple-unit sieving apparatus positioned for filling the pit during these proof tests. The average density obtained for the vibratory method was 107.1 pcf. The average density obtained for the sieving method was 107.2 pcf.

PROCUREMENT AND PROPERTIES OF BACKFILL SAND

The cost of procurement and transportation of NCEL test sand from Ventura County, California, to the test site at the Suffield Experimental Station (SES), Alberta, Canada, for backfilling purposes was considered to be excessive; therefore, Projects 3.4 and 3.2 purchased sand from Kimmitt Concrete Limited, Medicine Hat, Alberta, Canada, through a joint contract administered by the Suffield Experimental Station.

The material was taken from a natural alluvial deposit of the South Saskatchewan River near Medicine Hat, Alberta. The natural sand was then washed and dried in a gas-fired asphalt batch plant. After drying, all material larger than the number 10 sieve (2.0 mm) and smaller than the number 200 sieve (0.075 mm) was removed by a screening process. The graded sand was then trucked to the test site and dumped on a protective plastic sheeting spread over the natural ground. Additional protective sheeting was placed over the sand and sand-bagged in place.

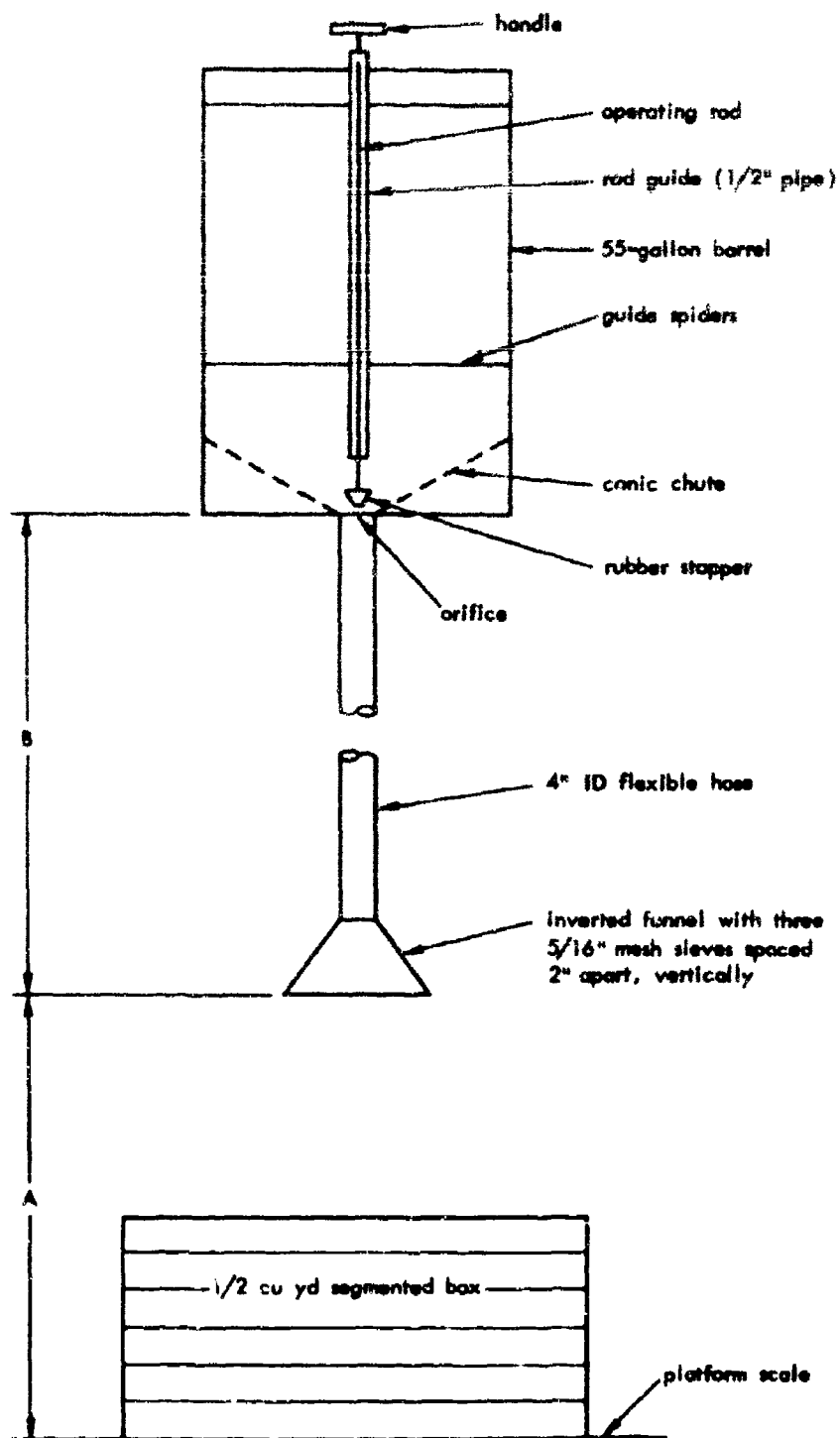


Figure B-1. Single-unit sieving device.

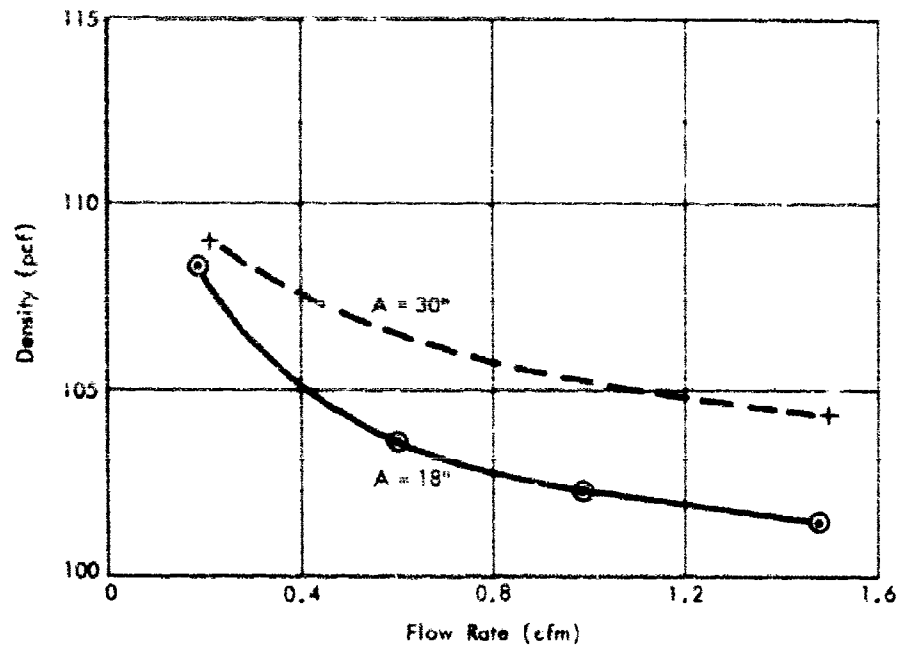


Figure B-2. Results of sieving tests.

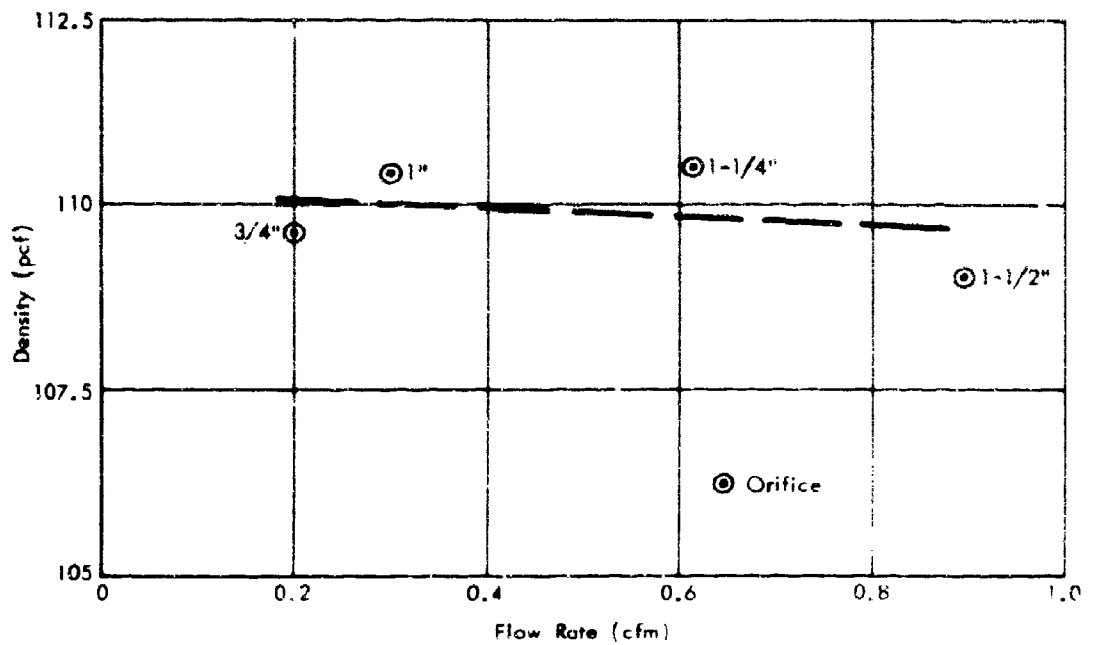


Figure B-3. Results of prototype calibration.

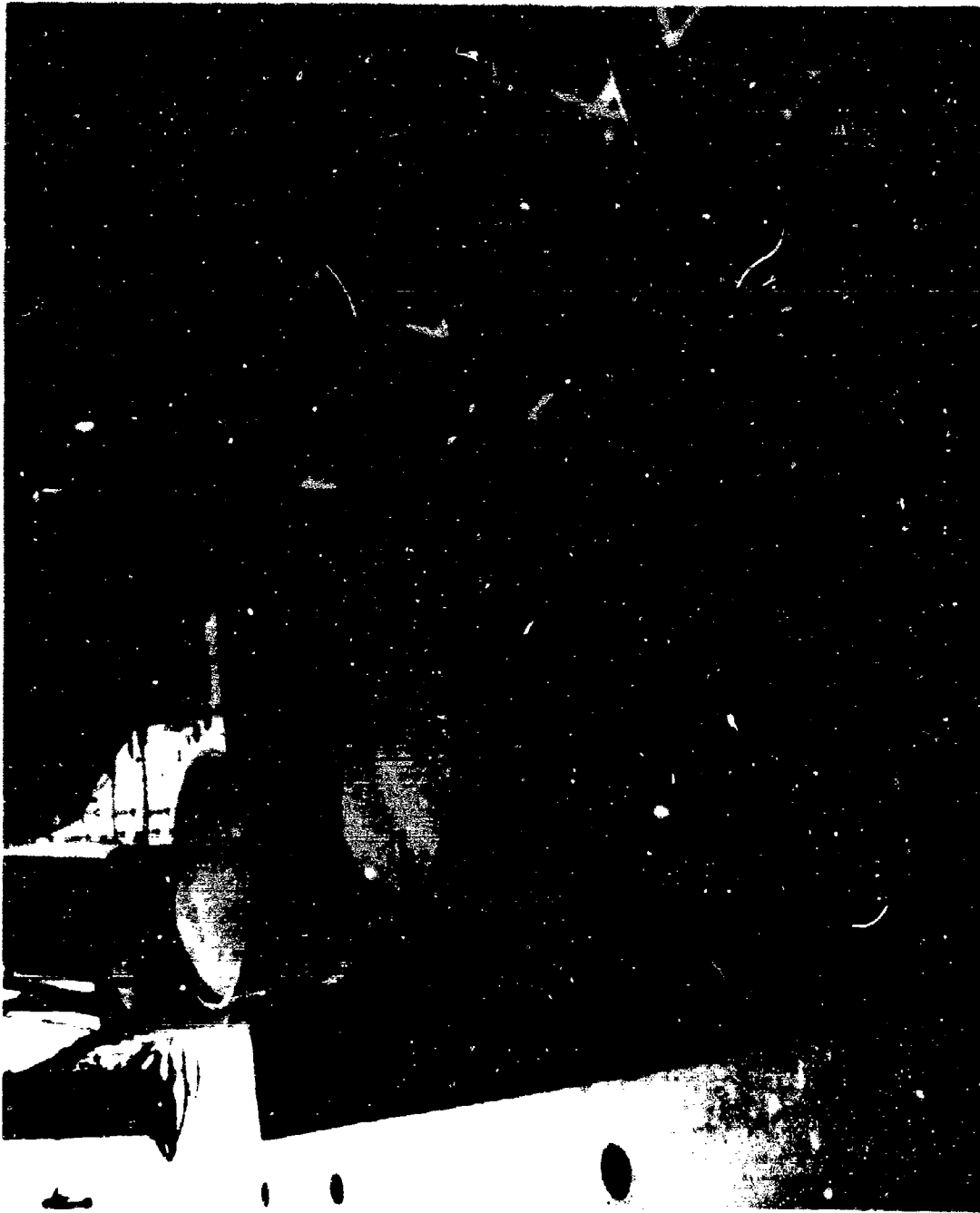


Figure B-4. Multiple-unit sieving apparatus during proof tests.

MECHANICAL ANALYSIS

Mechanical analyses of the sand delivered to the site are given in Figure B-5. The variability in the analyses could be due to the natural occurrence of the sand or to the screening process. The uniformity coefficient is about 2.1.

MICRO-ANALYSIS

Figure B-6 is a microphotograph of a typical group of sand grains from the material used for backfilling. A millimeter scale is shown at the edge of the figure. The sand is predominantly quartz with small portions of other rock fragments. A reddish clay containing oxides of iron often fills the interstices in the quartz and other rock. The quartz material is quite rounded.

VOID RATIOS

The maximum void ratio was determined by placing the sand in a 1/30-cubic foot mold through a 1/2-inch-inside diameter funnel held close to the surface of the sand. Three trials produced an average density of 95 pcf. The specific gravity of the sand grains is 2.67, so the maximum void ratio is about 0.75.

The minimum void ratio was determined in the following manner. The sand was placed in a 1/30-cubic foot mold in two layers. Each layer was compacted by 30 blows of a drop hammer weighing 10 pounds and falling 18 inches on a 2-inch-diameter base. Two trials produced an average density of 113.9 pcf, or a minimum void ratio of 0.46.

TRIAXIAL COMPRESSION TESTS

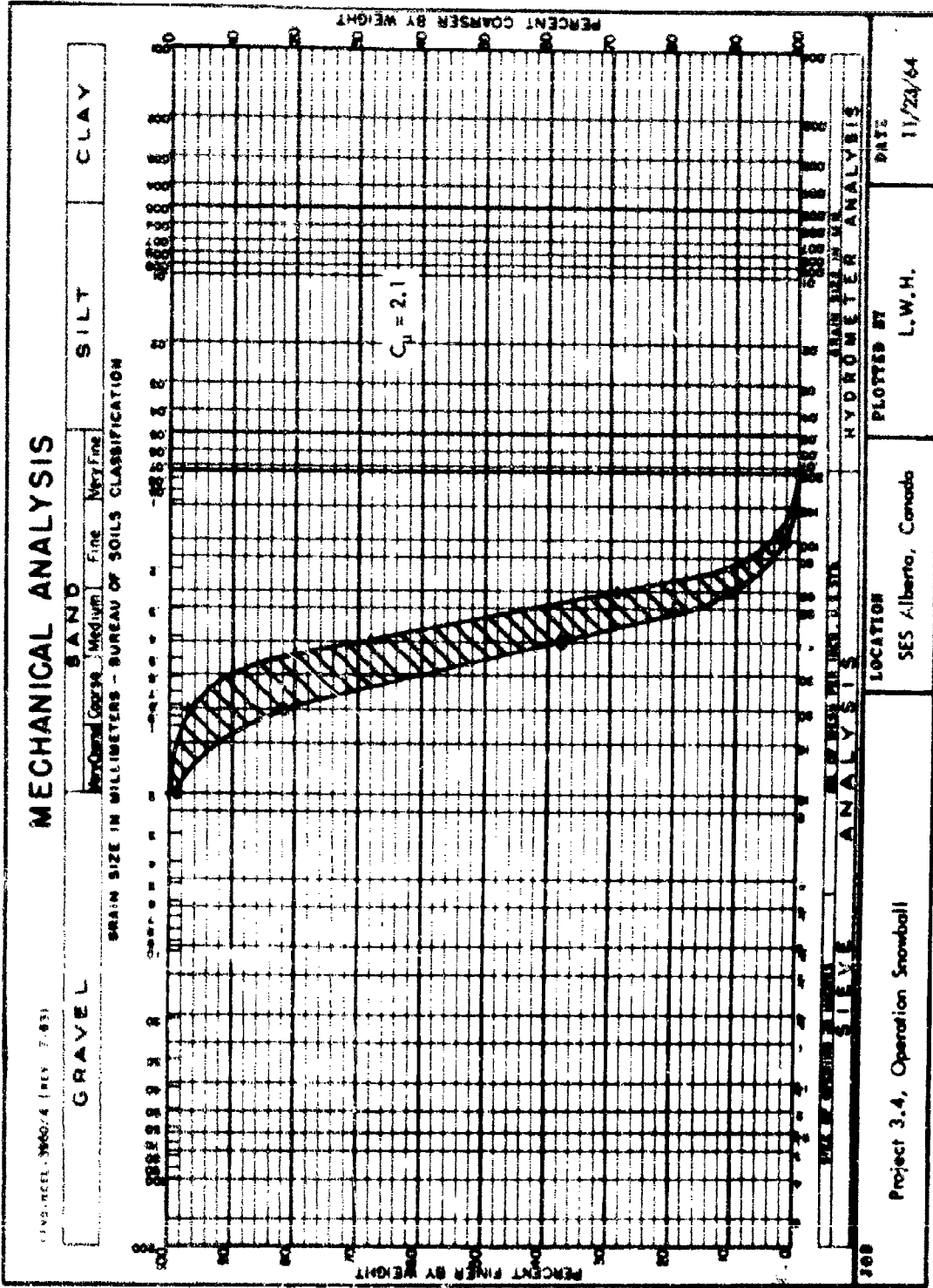
Table B-1 presents the results of drained triaxial compression tests performed on specimens of the backfill sand. Tests N-1 through N-4 were performed at NCEL, and Tests A-1 through A-3 were conducted at the University of Alberta, by Dr. E. W. Brooker. The relatively low friction angles are primarily attributable to the large portion of rounded quartz particles contained in the backfill material.

SIEVING APPARATUS CALIBRATIONS

One multiple-unit sieving apparatus and a Toledo platform scale (2,000 lb. capacity) were shipped to the test site at the Suffield Experimental Station. One of the sieving units was used for calibration purposes prior to any backfilling operation. The unit was suspended from a truck A frame and centered over the segmented box placed on the Toledo scale. The bottom of the inverted funnel was located 36 inches from the bottom of the 36- by 36- by 18-inch-high segmented box. The vertical distance from the orifice in the barrel to the bottom of the inverted sieve funnel was 5 feet. Sand was sieved into the segmented box and distributed evenly by slowly moving the funnel in lateral directions from its initial position.

This procedure resulted in sand drop distances from 36 inches to 18 inches. Subsequent density calculations revealed that, for this granular material, there was no significant variation in density for the range of drop distances. The average density obtained was 110.8 pcf or a relative density of 0.83.

A second calibration was performed in the same manner after the backfilling had been completed. The average density obtained was 110.8 pcf.



PERCENT FINER BY WEIGHT

PERCENT COARSER BY WEIGHT

ANALYSIS

LOCATION

DATE

Project 3.4, Operation Snowball

SES Alberta, Canada

HYDROMETER ANALYSIS

PLOTTED BY

11/23/64

300

200

100

50

25

Figure B-5. Mechanical analyses of backfill sand supplied by Kimmitt Concrete, Ltd.

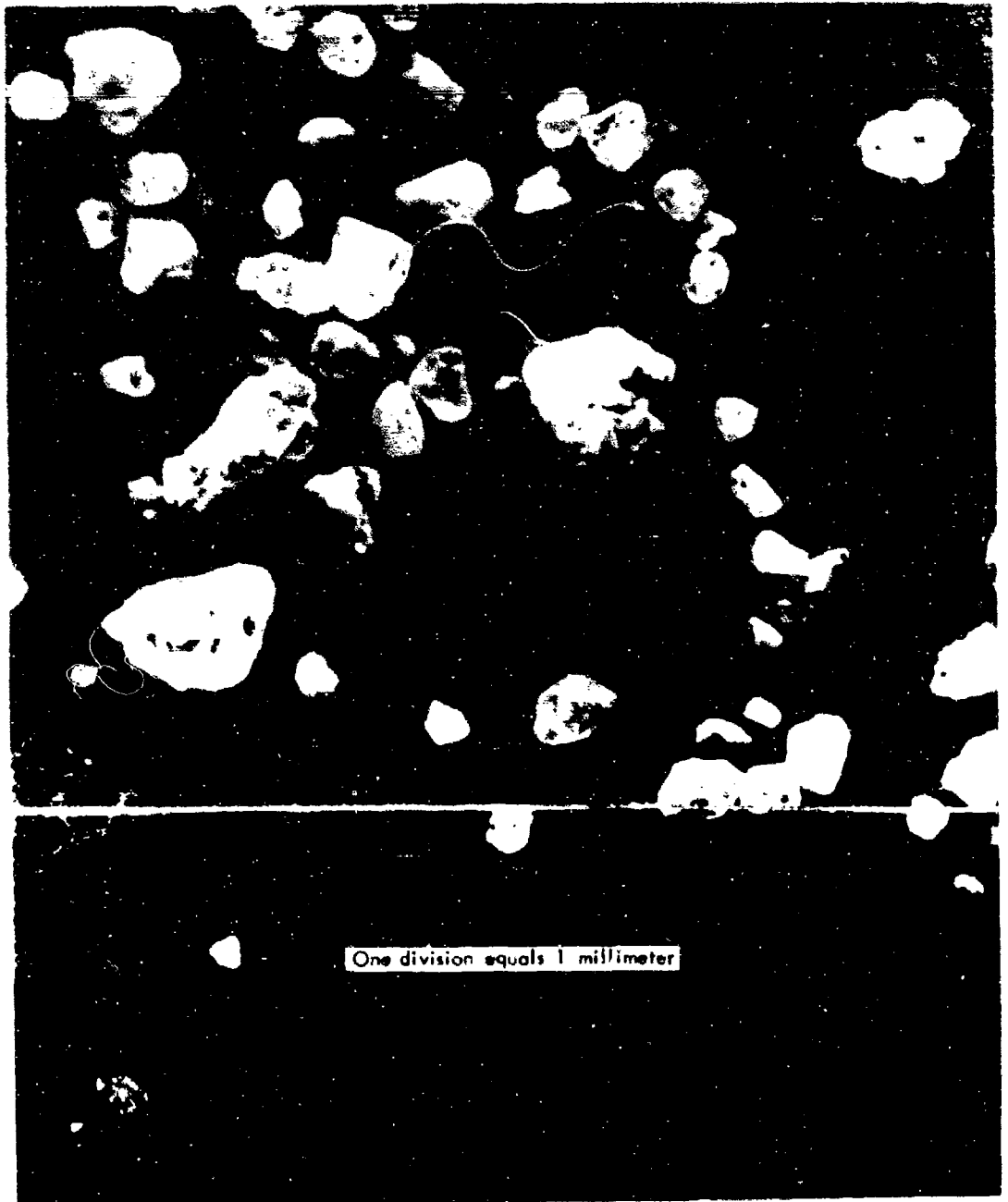


Figure B-6. Microphotograph of SES sand grains.

Table B-I. Results of Triaxial Compression Tests

Test No.	Confining Pressure (psi)	Loading Rate (in./min)	Relative Density	Friction Angle (deg)	Initial Tangent Modulus (psi)	Remarks
N-1	10	0.025	0.53	35.1	4,000	Air dry
N-2	10	0.025	0.55	34.4	3,200	Air dry
N-3	20	0.025	0.68	34.1	6,500	Air dry
N-4	20	0.025	0.70	34.1	5,300	Air dry
A-1	40	0.049	0.41	34.1 \pm 1.5	---	5.07% moisture
A-2	80	0.049	0.45	34.1 \pm 1.5	---	5.07% moisture
A-3	120	0.049	0.31	34.1 \pm 1.5	---	5.07% moisture

SAND AND ARCH PLACEMENT

The plan view of Project 3.4 (Figure 2) shows the locations of the excavated pits. The stockpile of sand was placed west of and adjacent to the pits so that the truck-mounted crane used to support, transport, and position the multiple-unit sieving apparatus could conveniently swing from the stockpile to the pit locations.

The field sieving operation required five men: three to distribute the sand flow from each of the three sieving units, one to operate all of the sieve control valves, and a crane operator to insure that no malfunction endangered the sand placement crew. The crane transported the apparatus to the stockpile where sand was placed into the sieving units with shovels. The units were then moved into place above the pit to be backfilled at a sand drop distance of 30 inches. The sand distribution and valve operation was directed to maintain a level sand surface during construction of the fill. When the units were emptied, they were returned to the stockpile for refilling. About 0.7 yard of sand was placed in each 20-minute cycle, so all of the pits could be filled in 30 hours.

In order to prevent disturbance to the structure of the sand placed in the pits, the following fill-and-trim method of bedding the arch footings was devised. After the surface of the sand had been brought to an elevation slightly below the level of the arch footings, thin angle iron supports were driven vertically into the placed sand, remote from the ultimate footing locations. These angles supported trimming guides, stiff horizontal angle irons connected between the vertical supports and running parallel to the major axis of the arch. Each of the vertical supports of the resulting H-shaped frame was then driven until the top surfaces of the trimming guides coincided with the plane of the arch footings. Additional sand was placed until the surface was slightly above this plane. A flat stainless steel blade, spanning the horizontal distance between and resting on the trimming guides, then was used to cut the bedding surface for the arch footings. Small plate-bearing tests were conducted on the trimmed sand surface between the trimming guides as described in a subsequent section of this appendix.

Two H frames were used for the small arches and three were used for the large arches. The center H frame was removed and the arch was set into its predetermined position before the exterior H frames were carefully pulled from the sand. Sand was placed interior to the large arches, up to the elevation of the bottom of the floating plywood flooring, by pouring it from a canister attached to a 2-foot-long handle and painstakingly leveling the surface with a wooden screed.

The flooring was placed inside the arches, the instrumentation was connected, and the end walls, with seals to prevent the infiltration of sand, were attached to the arches before the backfilling operation was continued.

The primary concern in placing sand around and over the semicircular steel arches was that the sieved sand grains should not strike the metal arch, slide over its surface, and impact the sand surface at low velocity. Such an action would seriously alter the condition of the sand near the sand-arch interface. The operators carefully distributed sand from the sieving apparatus so that only the edge of the fall pattern struck the steel arch. This method of distribution produced a sand surface which was slightly concave downward toward the arch and its end walls during backfilling to the elevation of the crown of the arch. The density of the sand for a few mean sand grain diameters from the arch is probably somewhat less than that obtained during calibration of the sieving apparatus. Sand was placed over the arch to an elevation 2 inches below final grade, a plastic membrane was placed over the entire sand surface, and the backfill was brought up to grade.

Certain difficulties, mistakes, and mishaps occurred during the backfilling operations. Weather conditions at the Suffield Experimental Station presented one difficulty: the unseasonable rains, a hail storm, and the winds in particular. Figure B-7 is a plot of the mean hourly wind velocities recorded at a height of 2 meters above the ground for the month of May during the years from 1955 through 1958. The early morning hours, the time of least winds, were utilized for placement of the backfill sand because the trajectories and random distribution of the free falling sand grains from the sieving apparatus were biased by horizontal wind currents. Four-foot-high plywood windbreaks were erected windward of the pits being backfilled whenever wind-induced segregation effects were noted. The pit for arch CA-3 was overfilled 2 inches so the backfill had to be excavated 4 inches, a new plastic membrane installed, and the fill brought up to the proper elevation. The backfill sand in arch pits CA-10, 11, and 12 was wetted during a rainstorm and was replaced before these arches were positioned. The backfill over and around arch CA-2 contained a small portion of silt particles up to 6 mm, because it was obtained from a stockpile placed on the ground surface; the original stockpile had become wetted due to deterioration of the covering plastic sheeting. The funnel sieves were often plugged by these particles during the sieving operation around and over arch CA-2. The truck-mounted crane dropped the multiple-unit sieving apparatus on two occasions during transport, but there were no personnel injuries during the entire backfilling operation.

SMALL PLATE-BEARING TESTS

Plate-bearing tests were conducted on the trimmed backfill surface to determine the initial modulus of the sand at the footing elevation of arches CA-1, CA-2, and CA-3. A schematic representation of the small plate-bearing device fabricated at NCEL is shown in Figure B-8. Reference 5 indicates that the failure load of this footing would be slightly more than 5 psi for a friction angle of 36 degrees, so only 13 of the 28 available weights were needed to perform the tests.

Four tests were performed in each pit at a position in line with the major axis of the arch footings and about 9 inches from the ends of the footings. The dial gage support frame was anchored to the trimming guides and the plate-bearing plunger was positioned on the sand surface under the gage operating shaft. The gage was then firmly secured and a preload of 0.9 psi was applied to the plate by adding steel weights to the top of the plate. Load-settlement data were recorded as additional weights were added. A typical load-settlement plot for arch pit CA-3 is given in Figure B-9.

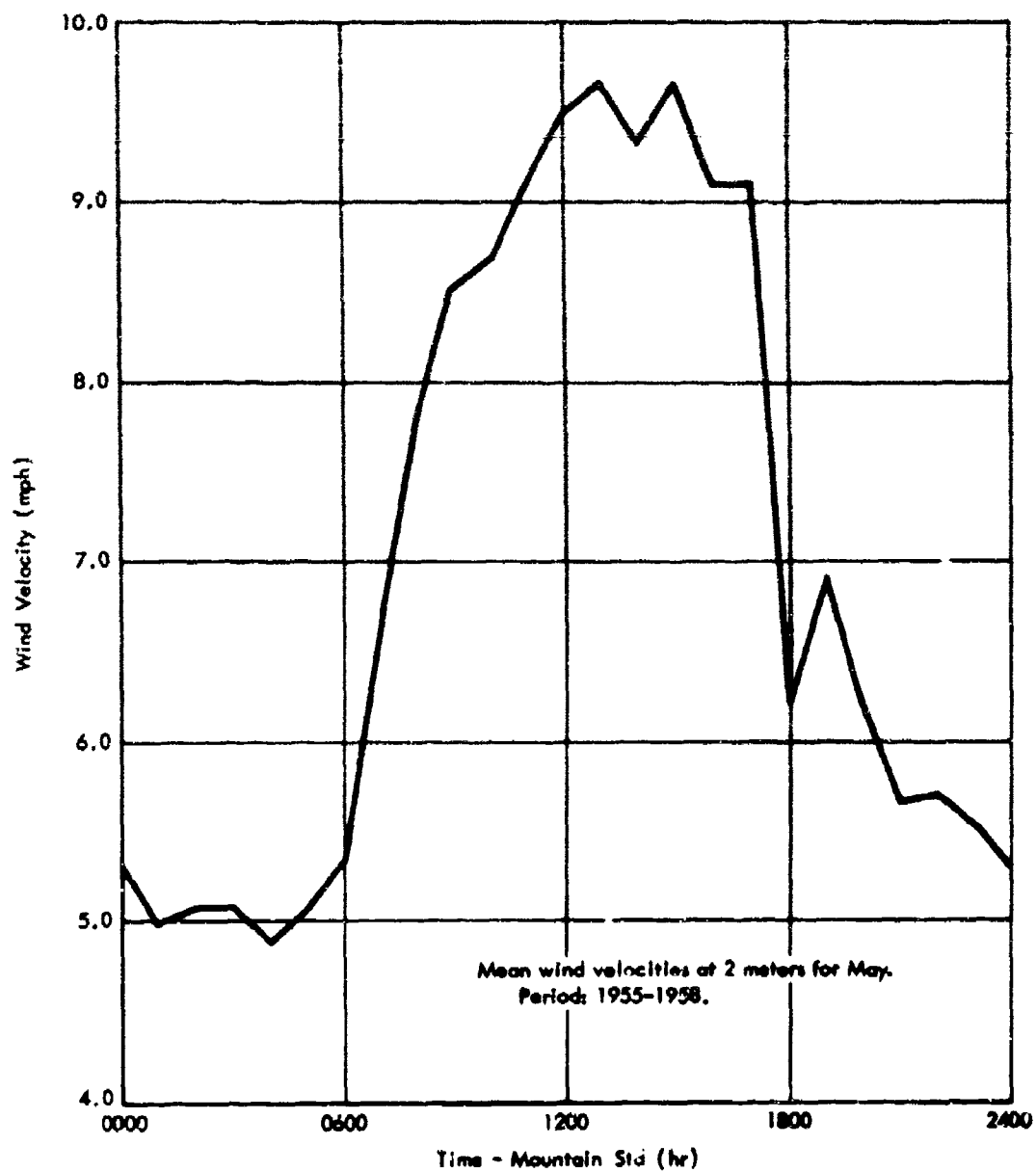


Figure B-7. Wind velocities at Suffield Experimental Station, Alberta, Canada

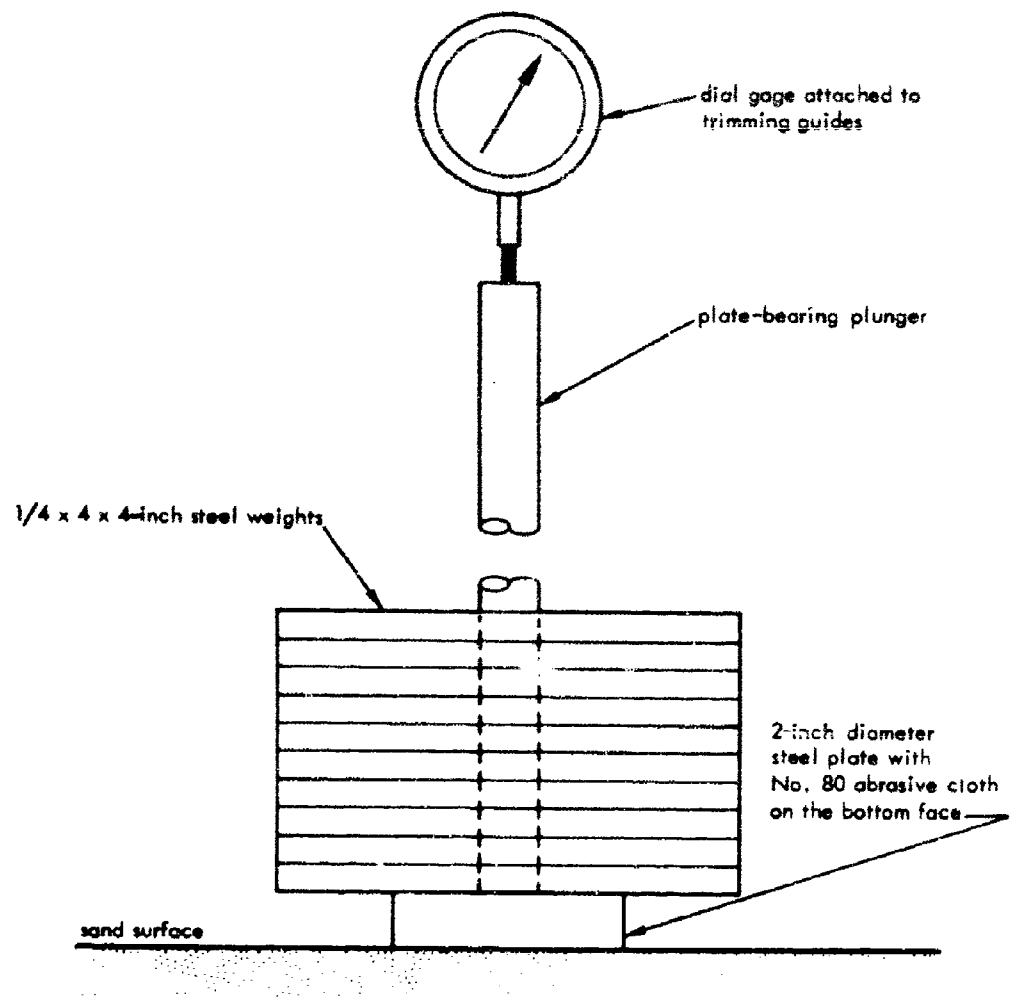


Figure B-8. Small plate-bearing device.

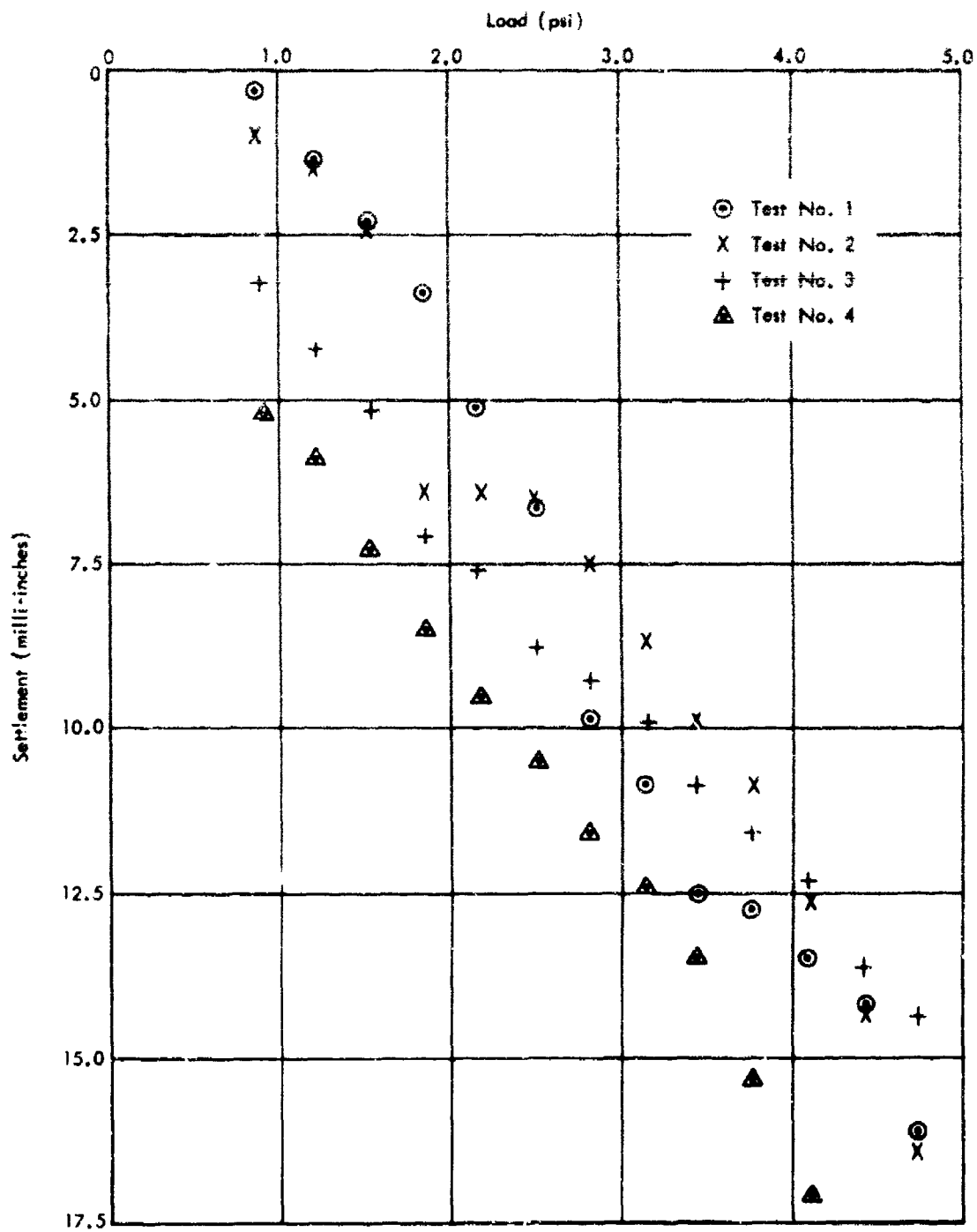


Figure B-9. Small plate-bearing tests on pit for arch CA-3.

Appendix C

INSTRUMENTATION

by

I. M. Derr and D. H. Johnson

INTRODUCTION

This appendix describes the electronic equipment and calibration procedures for Project 3.4. Thirty-six channels of instrumentation were provided to measure pressure, strain, deflection, velocity, and acceleration. The amplifying, recording, control, logic, and measuring systems are described, and the characteristics of the various transducers, their placement, and the method of calibration are outlined. Mechanical backup measurements were made wherever practicable and the nature of the backup measurements is explained. A schematic block diagram of the system is shown in Figure C-1.

RECORDING EQUIPMENT

Characteristics of Recording System

All electronic measurements were made with Consolidated Electrodynamic Corporation System D recording equipment with CEC Model 5-114-P4, 18-channel oscillographs. The components of System D, shown in Figure C-2, are: (1) a power supply to furnish DC and filament voltages to carrier amplifiers plus 3 kc, 10 volts rms for gage excitation, and (2) bridge amplifiers that provide uniform amplification of signals from the bridge, compensate for resistive and reactive unbalance in the pickup and its connecting cable, and demodulate the 3 kc carrier.

Specifications of the bridge amplifiers are:

1. Full-scale output: ± 5 ma into a 24-ohm load, corresponding to a 4-inch double amplitude galvanometer trace deflection using a CEC type 7-323 galvanometer.
2. Sensitivity for maximum output: 1 mv, with no attenuation; 1 v maximum, with full attenuation.
3. Input impedance: approximately 1,800 ohms.
4. Input attenuator: 20 steps, 1 to 1,000, and off.
5. The bridge balance system will accommodate:
 - a. A four-arm bridge composed of wire strain gages or other resistive elements - each element 120 to 500 ohms, with maximum bridge unbalance of 65 mv for 10 v across the bridge.
 - b. A two-arm variable reluctance pickup suitable for use at 3 kc.
6. Controls provide:
 - a. Phase balance.
 - b. Amplitude balance.
 - c. Reference voltage phase control.

- d. Galvanometer off-on switch.
 - e. Calibrate + and - switch.
 - f. Balance operate switch.
 - g. Attenuation.
7. Linearity: Output current is proportional to the input voltage within 2 percent of maximum output.
 8. Frequency response: Galvanometer trace amplitude \pm 2 percent for modulating frequencies from 0 to 600 cps, when connected to a CEC 7-323 galvanometer.
 9. Output impedance: 1,000 ohms.

CONTROL EQUIPMENT

Logic Units

The primary function of the logic units is to accept remote field timing relay closure commands to cycle the System D. Magnetic Research Company, Inc., Model 362-9 logic units were employed. These units are designed especially for use with CEC System D in conjunction with Magnetic Research Coupling Modules, Model 362-2.

The commands and responses for Project 3.4 were:

Command Closure

Response

- 30 minutes
- 15 minutes
(backup)
- 10 seconds
- 5 seconds
(backup)

Turn on power to system for warmup.

1. Start oscillograph drive.
2. 50-percent calibration step on.
3. 100-percent calibration step on.
4. Calibration off.
5. Data recording.
6. 50-percent calibration step on.
7. 100-percent calibration step on.
8. Calibration off.
9. Stop oscillograph.
10. Turn off warmup power.

Each calibration step is about 1 second long and the data run between preshot and postshot calibrations lasts about 20.67 seconds. Before the signal is received to start the paper drive, there is the possibility that the warmup power might be turned off by the removal of the -30 minute and -15 minute timing signal. This could result in the loss of a record; thus, to preclude such a possibility, latching relays were installed with each logic unit to provide continuous closure if the timing signals should fail. An advantage of using latching relays is the ability to cycle the logic units independently during preshot tests without removing cables.

Once the paper drive signal has been received, the unit is "locked" into a complete sequence cycle. This eliminates the possibility of shock opening a relay and turning the system off during the data recording period.

The logic units will operate on either 115-volt AC, 60-cps power, or 24- to 28-volt DC power. They will not respond, however, to the paper start command unless 115 volts AC is supplied. When the units are battery operated, the AC power is furnished by converters operating from 24-volt batteries.

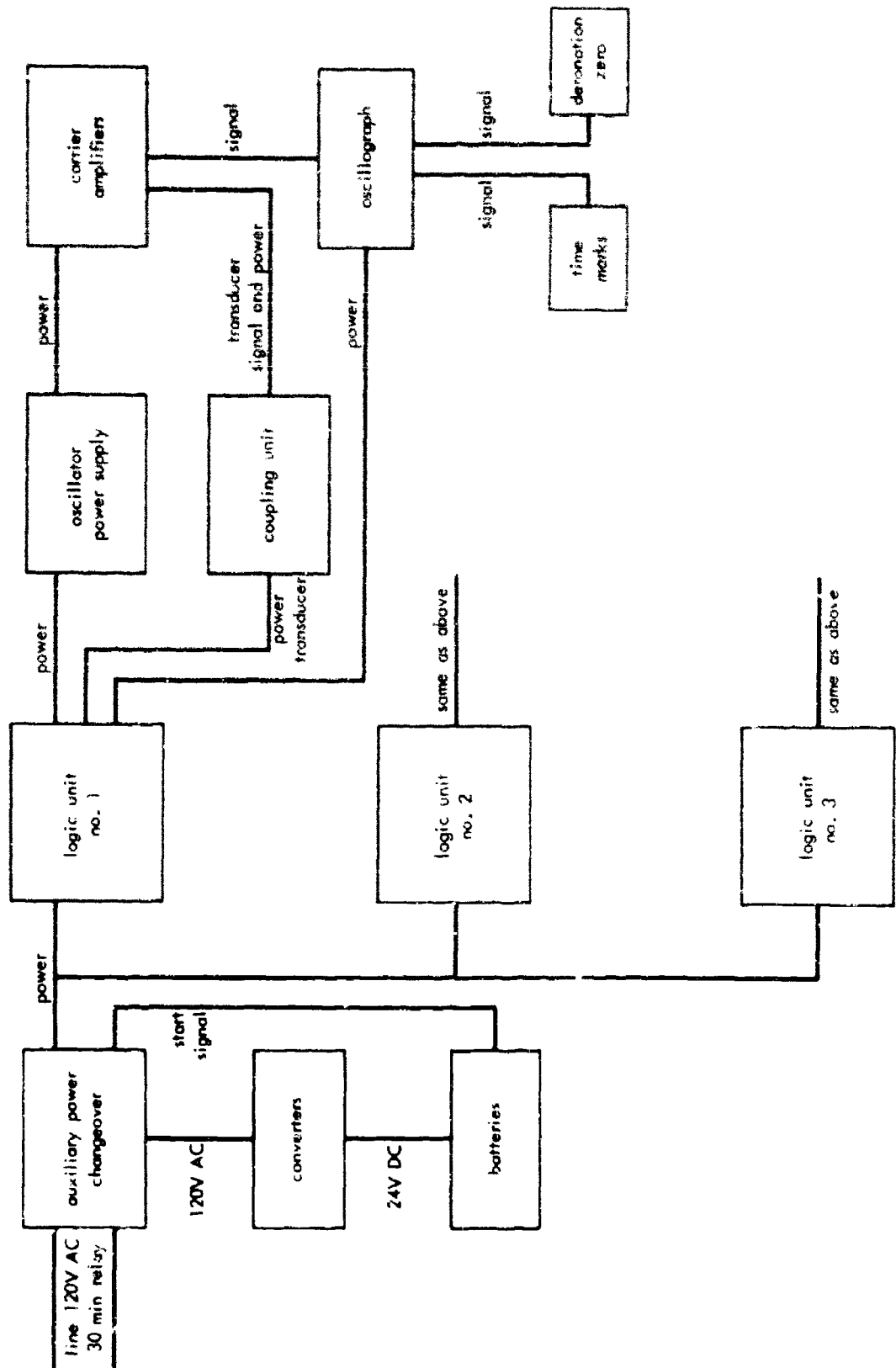


Figure C-1. Instrumentation system layout.



Figure C-2. View of electronic instrumentation.

Power Backup

If the 115-volt AC power should fail, an automatic switchover to 24-volt DC operation will occur. This is accomplished with an NCEL designed sensing and switching unit. When the AC from the power mains exceeds 125 volts or falls below 105 volts, the switchover to battery operated converters occurs. Sufficient batteries were installed for 1 hour of operation, with an auxiliary set on standby for quick connection, if they were needed.

The 24-volt DC to 115-volt AC converters used were Carter Model E 1050 CP. These devices are capable of continuously supplying 500 watts of AC power.

Timing Marks

Identical timing marks were placed on each oscillograph record with a timing generator designed and built at NCEL. A timing mark occurs each 1/100th of a second. The mark for each 1/10th of a second is twice the amplitude of the 1/100th second mark. This assures time correlation of the four oscillographs. An additional time correlation is provided by the application of a detonation zero time pulse which occurs at the time power is applied to detonate the explosive charge.

Phase Locking Carrier Power Supplies

When more than one carrier power supply is used in a common measurement system, there is the possibility of an undesirable sinusoidal pickup in the signal leads. The frequency of this pickup is the difference between carrier frequencies. The procedure recommended by CEC for eliminating such pickup is to use slaving connections between power supplies. By this method, only one oscillator generates the carrier frequency while the remaining units operate as "slave" amplifiers. The disadvantage of this method is that a failure of the master oscillator results in failure of all carrier voltages and consequent loss of data on all channels.

To overcome the latter problem, a 0.005 mfd capacitor was connected from a common buss to pin 1 of the slaving terminal of each oscillator power supply. With this method, there is sufficient coupling to obtain phase locking when all oscillators are allowed to operate. If one oscillator should fail, there would be a 20-percent decrease in carrier voltage with a resulting 20-percent decrease in data trace amplitude. There also would be a 20-percent decrease in calibration trace amplitude; therefore, the corresponding correction factor could be applied to obtain valid data.

Coupling Units

Effects measurements from high-explosive field tests often require long transducer cables and a variety of transducers with various electrical characteristics. These conditions create a requirement for a broad range of control for electrically phasing and balancing of transducer signals. In addition, with the CEC System D, a method is needed for remote calibration. The coupling unit used was designed by BRL to fulfill these requirements.

The functions of the coupling units are to provide:

1. Local and remote control of electrical calibration.
2. Auxiliary transducer zero balance control.
3. Controls for phase and, thus, deflection reversal of transducer and calibration signals.
4. Optional oscillator power supply isolation from the transducers.
5. Vernier signal attenuation.
6. Solderless mounting for phase altering and shunt calibration elements.
7. Carrier and signal monitoring points.

TRANSDUCERS

The deflection, strain, velocity, and acceleration gages discussed in the following paragraphs are shown in position, as they were mounted, in Figure C-3.

Pressure Gages

The overpressure gages employed were Wiancko Type 3PAD100. Specifications of the gages are:

1. Maximum pressure: 150 percent of range.
2. Linearity: 0.5 percent or less of pressure range.
3. Hysteresis: 0.5 percent of pressure.
4. Resolution: continuous.
5. Rise time: 100 to 300 microseconds.
6. Natural frequency: 1,000 to 4,000 cps.
7. Acceleration sensitivity: 0.01 percent to 0.05 percent of range per g of acceleration depending on application.
8. Compensated temperature range: -25 F to +180 F.
9. Zero drift with temperature: less than 2 percent of range over 100 F.
10. Sensitivity change with temperature: less than 2 percent of range over 100 F.

Deflection Transducers

The deflection transducers used were: one Bourns Alignopot Model 156, Part Number 15620-0-2.5-103, and two Bourns Model 108 Linear-Motion Potentiometers, Part Number 10820-0-131-103. Alignopot Model 156 has a total useful deflection range of 2.5 inches and has a ball and socket at the shaft entry point to prevent shaft binding, if the shaft and body should not be aligned due to a transverse movement of one with respect to the other. The Model 108 potentiometers have a useful measurement range of 1.31 inches. Both units, of 10,000 ohms resistance, were connected into a bridge circuit to make them compatible with the System D equipment. A sketch of the circuit is shown in Figure C-4. Resolution is limited only by the diameter of the wire used in winding the linear resistance element which, in these two models, is 17 mils.

Strain Gages

The strain gages used were "Denfoil" type, die-cut foil, manufactured by Dentronics, Incorporated. These gages have a resistance of 120 ohms with a tolerance of ± 0.2 ohm and a gage factor of 2.07 ± 1 percent. The gages are self-compensated for stainless steel to within 20 microinches indicated strain over the temperature range of 45 F to 125 F, and within 10 microinches from 60 F to 110 F. Gage factor variation with temperature is less than 0.01 percent per degree F. Overall dimensions of the gage, including backing, are 11/16 by 3/8 inch; dimensions of the active element are 0.25 by 0.29 inch.

The gages were cemented with Eastman 910 cement after first roughing the back of the gage with a small fiber glass brush. Subsequently, the gages were waterproofed with petrocene wax and a layer of electric tape, both of which then were covered with black Ten-X sealing compound, manufactured by Electro Cote Company.



Figure C-3. View of gages near footing.

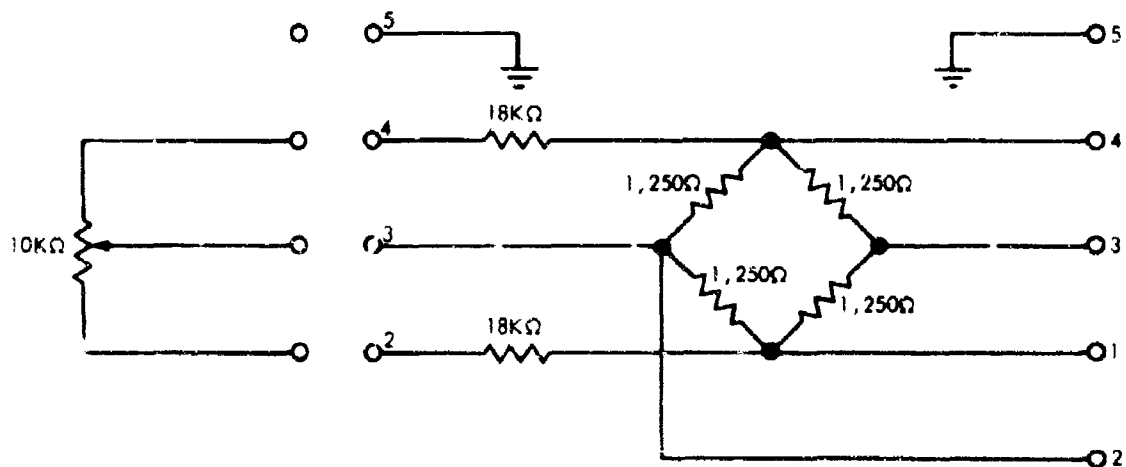


Figure C-4. Schematic of bridge circuit.

Velocity Gages

Measurement of velocity of the arch footings and of two points in the free field were made with Stanford Research Institute (SRI) Mark II velocity gages. These gages operate on the principle of an over-damped accelerometer. A hinged thin plate, suspended in oil, is forced through the oil by any acceleration in the vertical direction. A restoring spring compensates for the normal gravitational forces acting on the plate. The transducer element of the system is a Wiancko variable reluctance gage; brackets attached to the plate change the reluctance between two coil assemblies as the plate moves through the viscous oil.

The SRI velocity gage is designed to operate at velocities of 1 to 60 ft/sec where the pulse duration is 10 msec or more. Sensitivity changes 1 percent per degree F; therefore, a sensitivity check is necessary before each test.

The gage operates on a carrier of up to 20 volts at 5 kc. In the Project 3.4 test, a carrier of 10 volts at 3 kc was used. Dimensions of the velocity gage are 1.5 inches in diameter by 3.625 inches in length; the gage weight is 480 grams. Those gages in the free field were encased in 4- by 4- by 3.6-inch blocks of foamed cement to match the density and to approximate the stiffness of the gages to the density of the surrounding soil.

Accelerometers

The accelerometers employed were Endevco Corporation Model A-2260-250-10. The accelerometers have a four, active-arm, bridge-sensing element which uses piezoresistive strain gages. The rated range of the units is ± 250 g and they can withstand ± 750 g or 200-percent overload for limited periods. Frequency response is from 0 to 2,000 cps with ± 0.5 -percent deviation at 1,000 cps and ± 3.0 -percent deviation at 2,000 cps. Sensitivity is approximately 1.25 mv per g acceleration. Dimensions of the unit are 0.615 inch in diameter and 1.10 inches in height. Deviation of sensitivity with temperature is less than 1 percent from 32 F to 125 F. To obtain high accuracy at low accelerations, 5 minutes of warmup time should be allowed to permit thermal transients to disappear. Also, these gages should be operated at the rated 10 volts excitation. The weight of one accelerometer is 35 grams.

Measurement Errors

Errors associated with various components of the measurement system are as follows:

<u>Component or Function</u>	<u>Error (%)</u>
Amplifier	2
Galvanometer	2
Readout	1
Transducer:	
Pressure	0.5
Deflection	0.5
Strain	0.5
Velocity	3
Acceleration	0.5 at 1,000 cps
Calibration	1

These errors are, cumulatively, less than the variations expected from one experimental setup to the next for soil-structure systems. Thus, even under the most unfavorable circumstances, the precision of the measurements is quite satisfactory for the type of test involved.

Calibration of Transducers

Pressure Gages. The Wiancko pressure transducers were calibrated in 20-percent increments to 140 percent of the estimated maximum pressure by loading with a static pressure. A calibration resistor was used in the circuit to determine any change in system sensitivity between calibration and test.

Linear Deflection Gages. The Bourns linear potentiometers were calibrated in 20-percent increments to 140 percent of estimated maximum deflection by using a micrometer mounted in a specially designed rack. A calibration resistor was chosen to give a deflection equal to approximately the deflection expected at the time of test, and the ratios of calibration and test deflections were used to determine the system sensitivity.

Strain Gages. The Denfoil foil strain gages were calibrated by placing a 100,000-ohm precision resistor across one arm of each four-arm strain bridge, simulating a strain of 600 microinches per inch. A calibrating resistor was placed in the coupling unit and the trace relationship at time of calibration and test determined changes in system sensitivity.

Velocity Gages. Calibration of the velocity gages was achieved by pulling the hinged plates against spring tension with a solenoid and then letting the plate drop with both the restoring force of the spring and natural gravitational forces acting on it, thereby producing a combined force of 2 g's. A record was taken and sensitivity was determined as trace deflection during 1 second divided by 64.4 ft/sec^2 . A calibrating resistor also was placed in the coupling unit and a record was taken at the time of the test, thus giving the relationship of the sensitivities of the amplifier circuit.

To detect changes in viscosity of the damping oil, a record was made of the time it took for the plate to move from a point where it had maximum spring tension to its at-rest position. A record was taken at the time of calibration and just prior to the time of test. Log amplitude versus time from these traces were plotted and the relationship of their slopes determined the change of sensitivity of the gage.

Accelerometers. Endevco accelerometers were calibrated in 20-percent increments to 140 percent of the estimated maximum acceleration using a Schavitz rotary accelerator. A resistor was placed in the coupling unit that caused a trace deflection equal to the deflection of approximately 100 percent of the maximum acceleration. The ratio between the trace deflection at calibration and at the time of test, when this resistor was placed across one arm of the bridge, determined the change in the sensitivity of the amplifier.

Appendix D

OSCILLOGRAMS AND SCRATCH TRACES

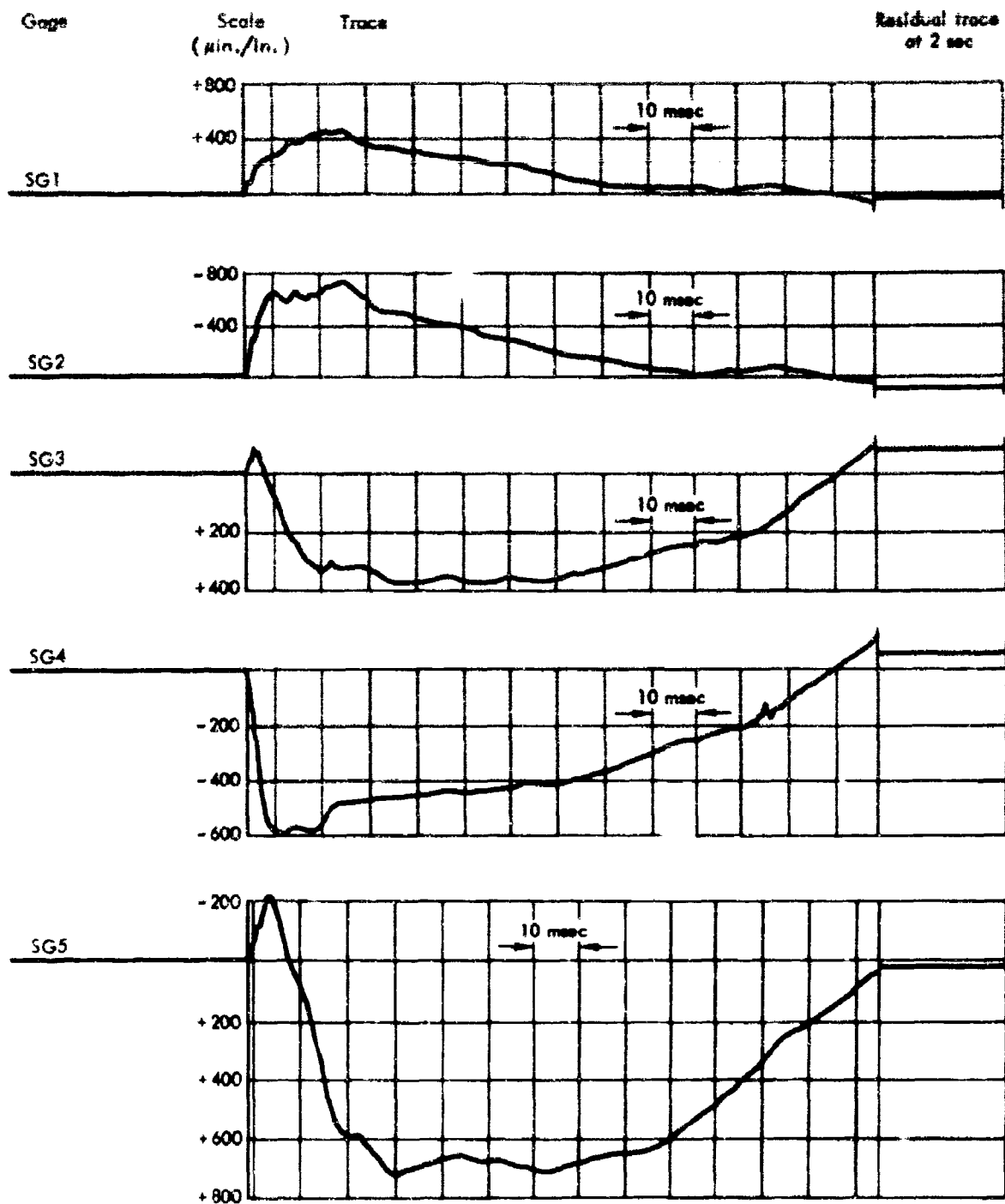


Figure D-1. Strain data from oscillogram.

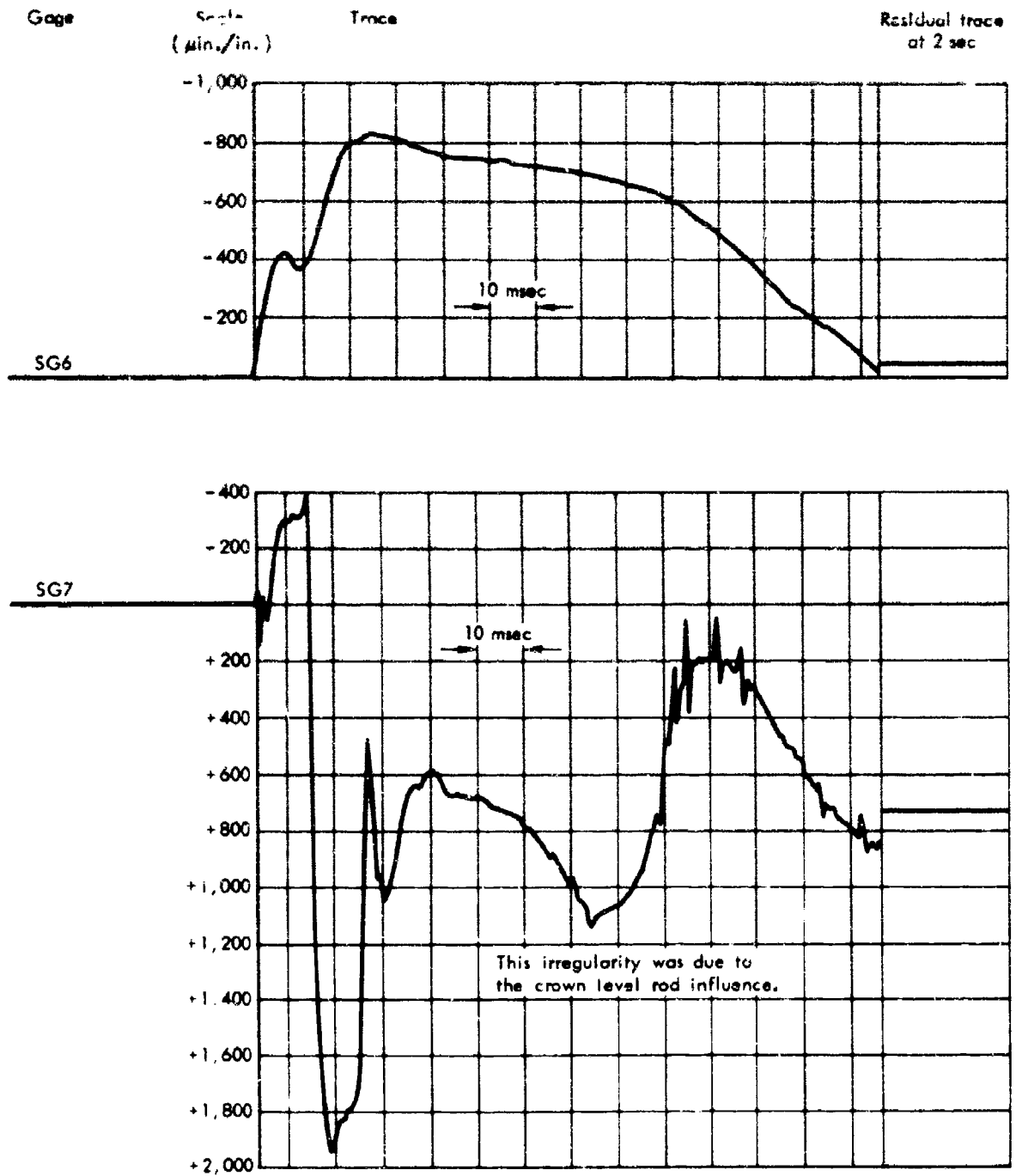


Figure D-2. Strain data from oscillogram.

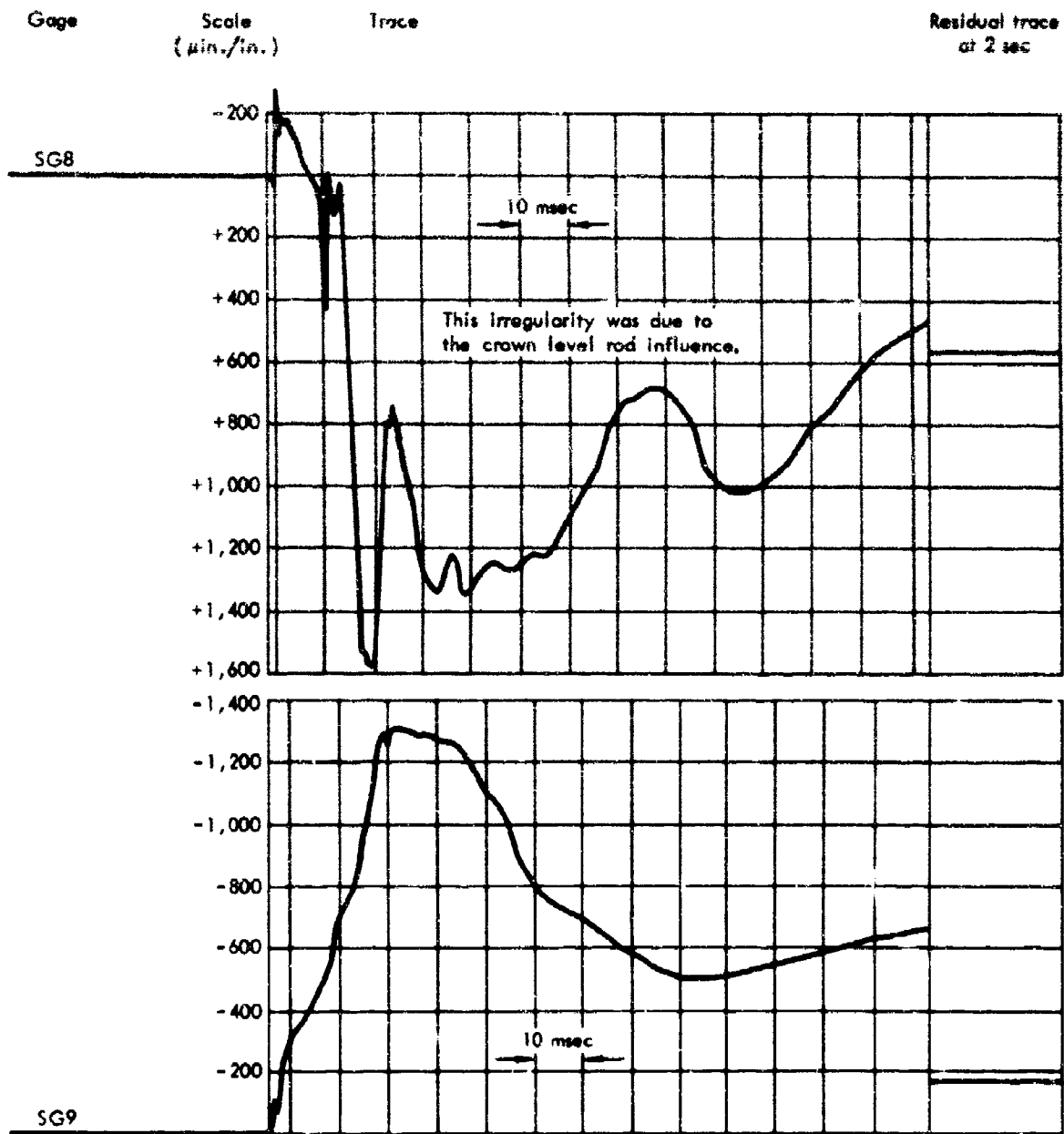


Figure D-3. Strain data from oscillogram.

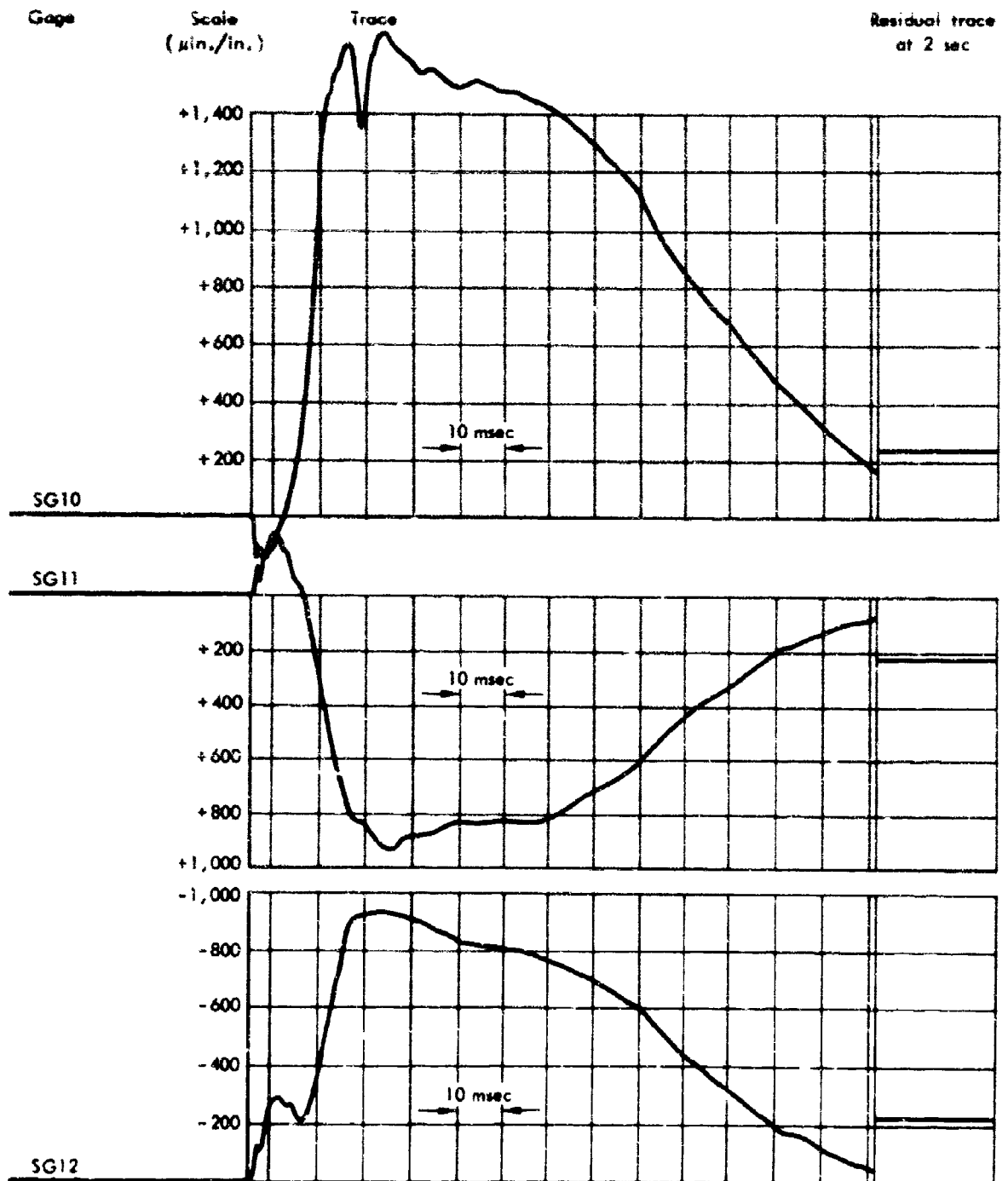


Figure D-4. Strain data from oscillogram.

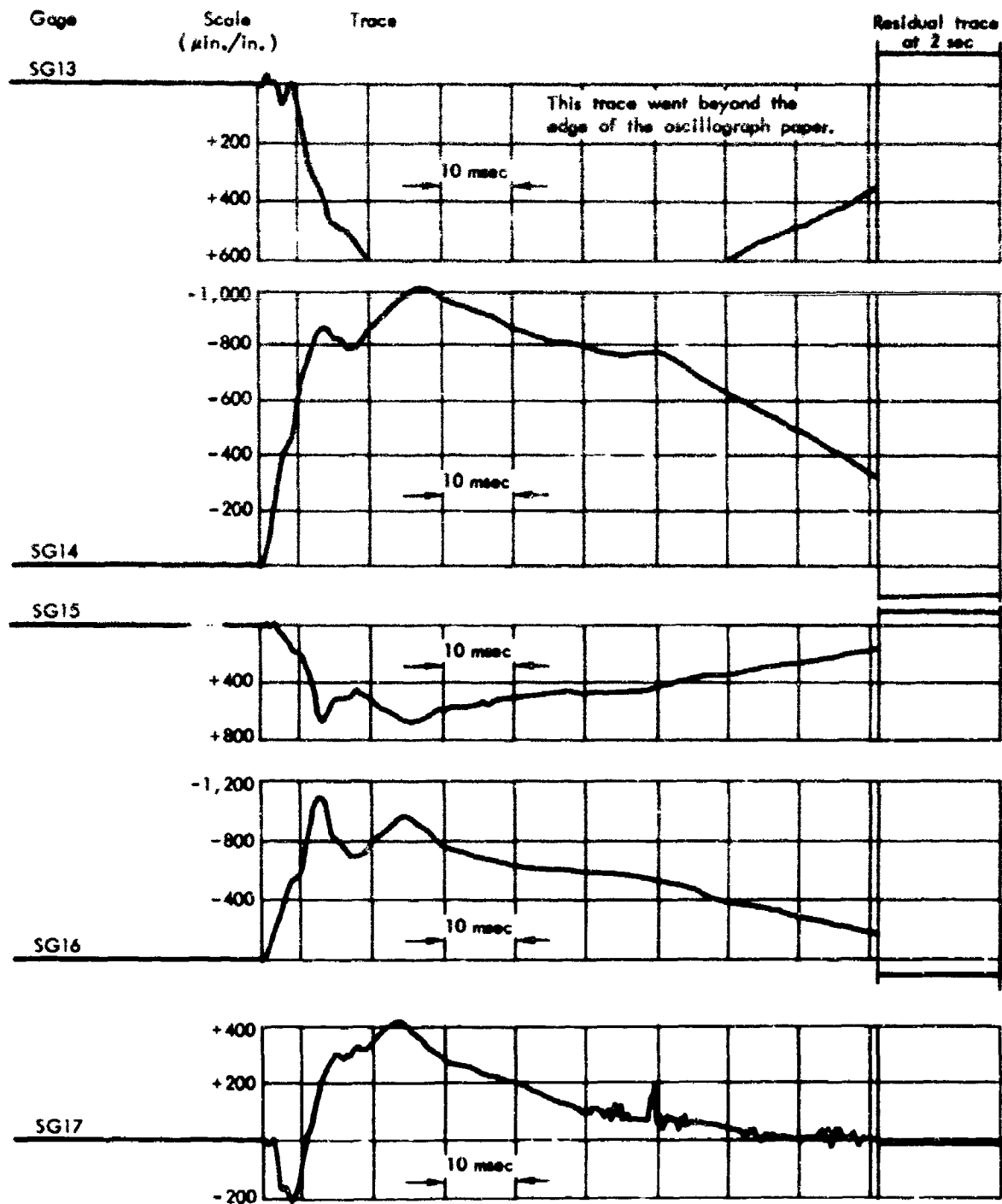


Figure D-5. Strain data from oscillogram.

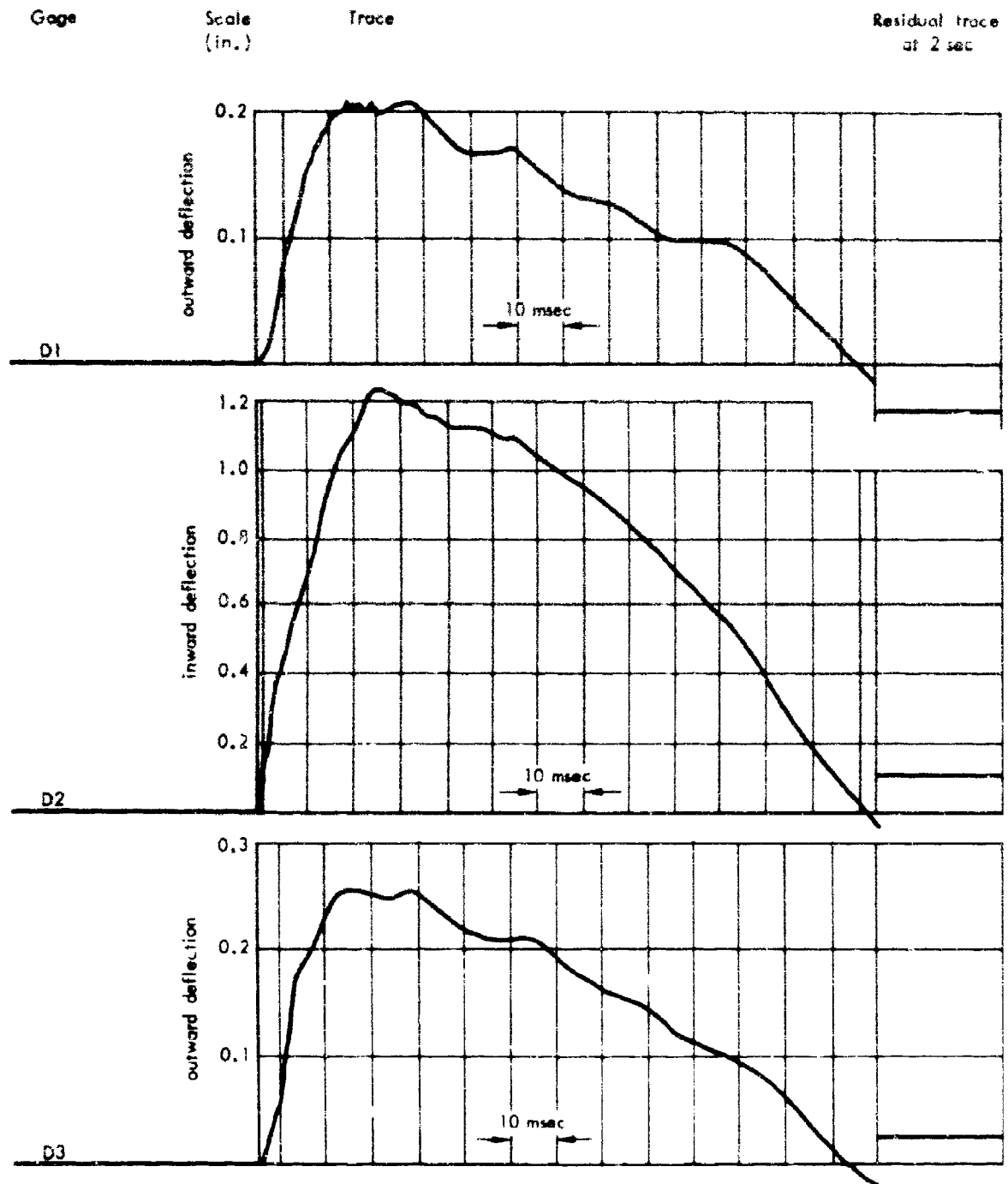


Figure D-6. Arch deflection data from oscillogram.

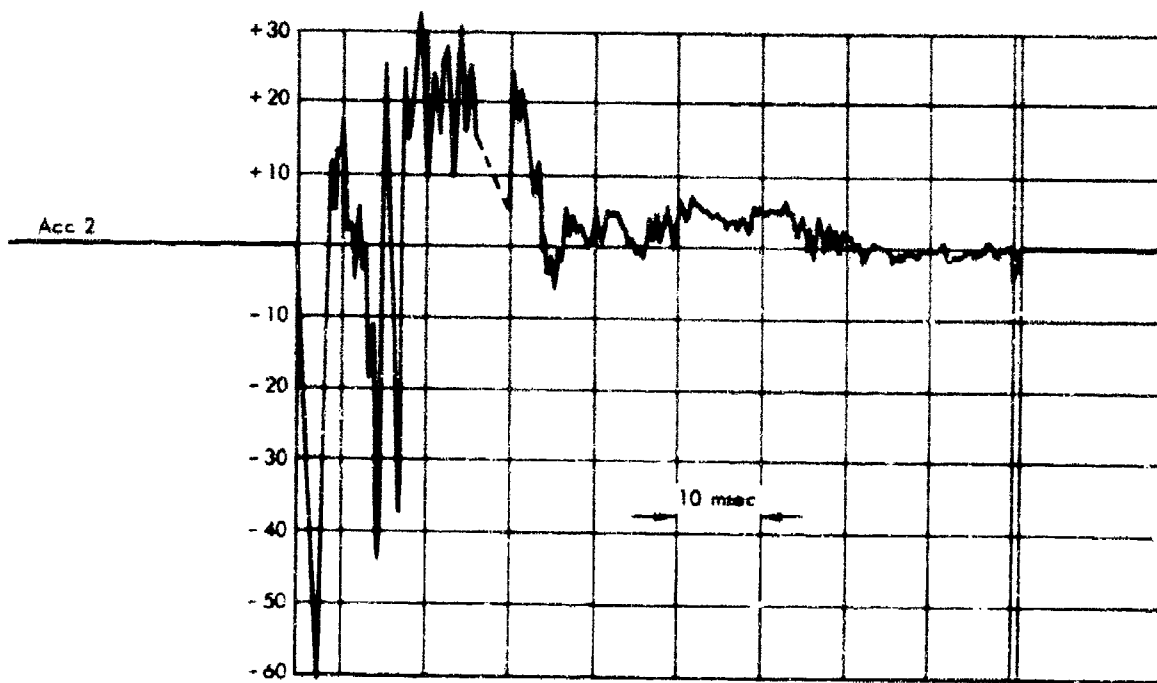
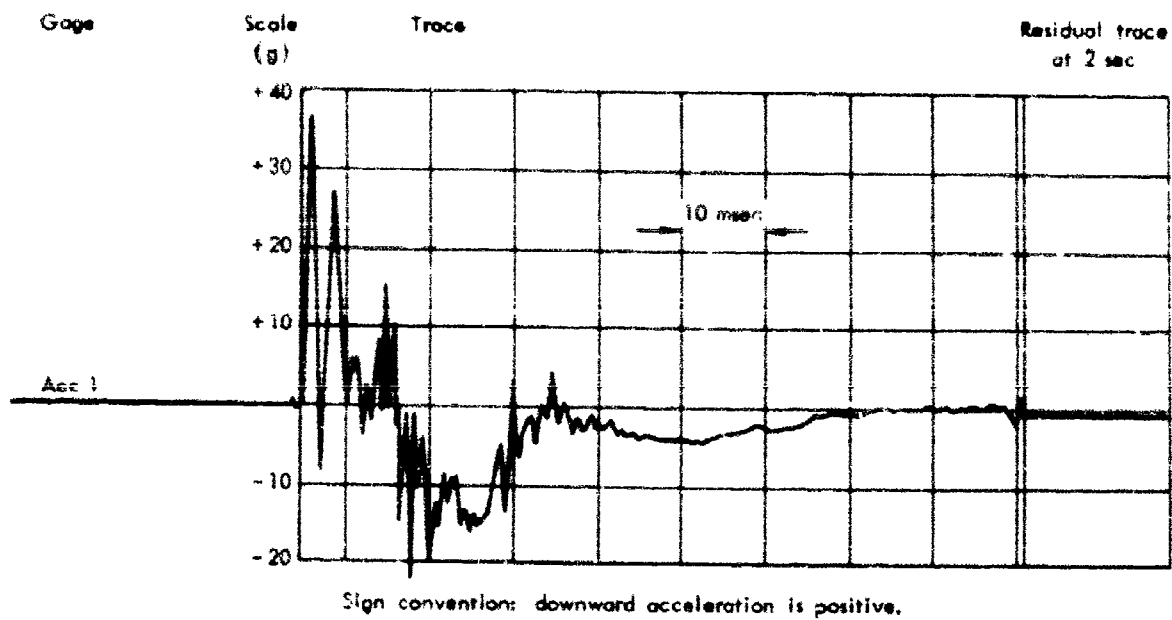


Figure D-7. Acceleration data from oscillogram.

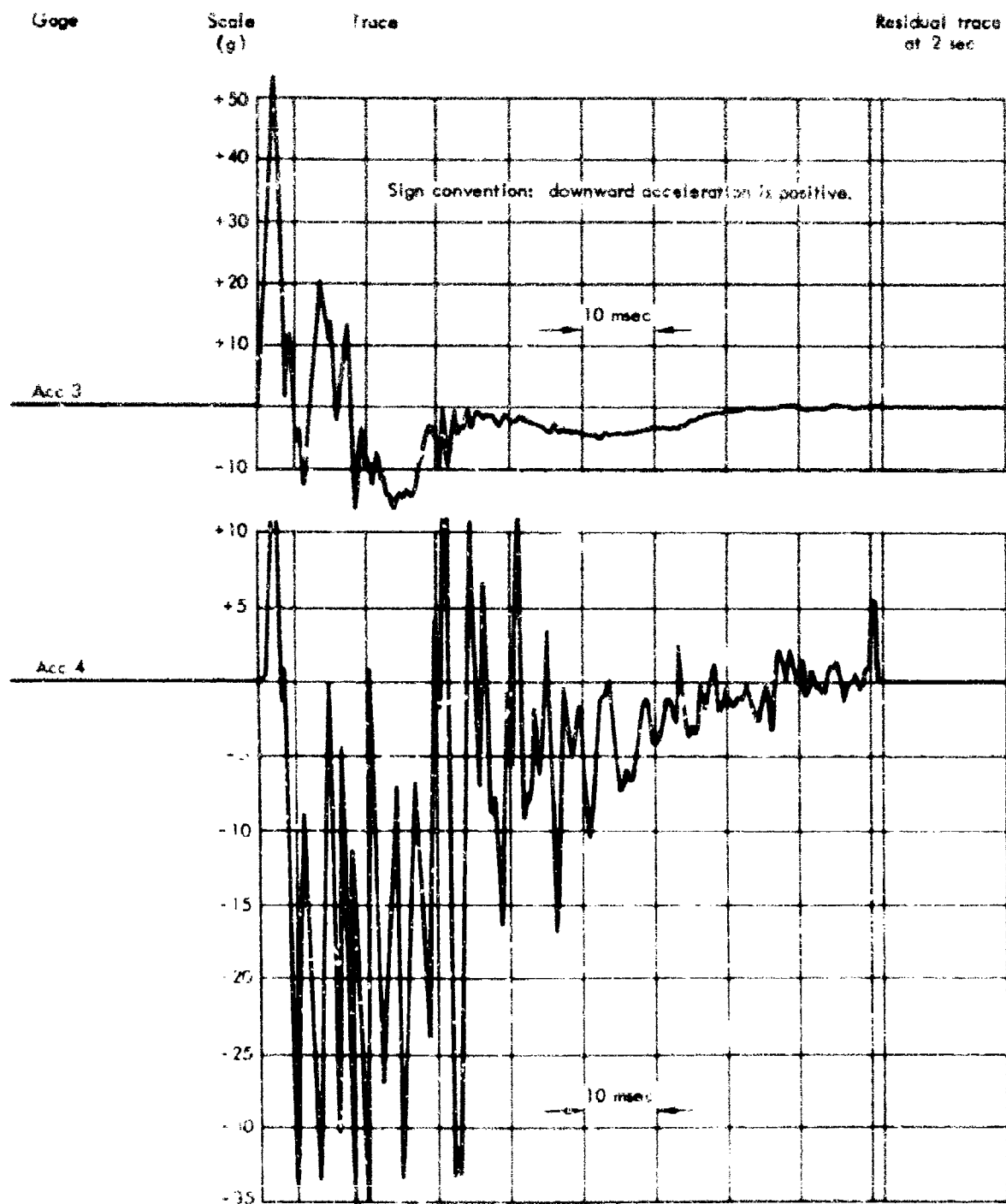


Figure D-3. Acceleration data from oscillogram.

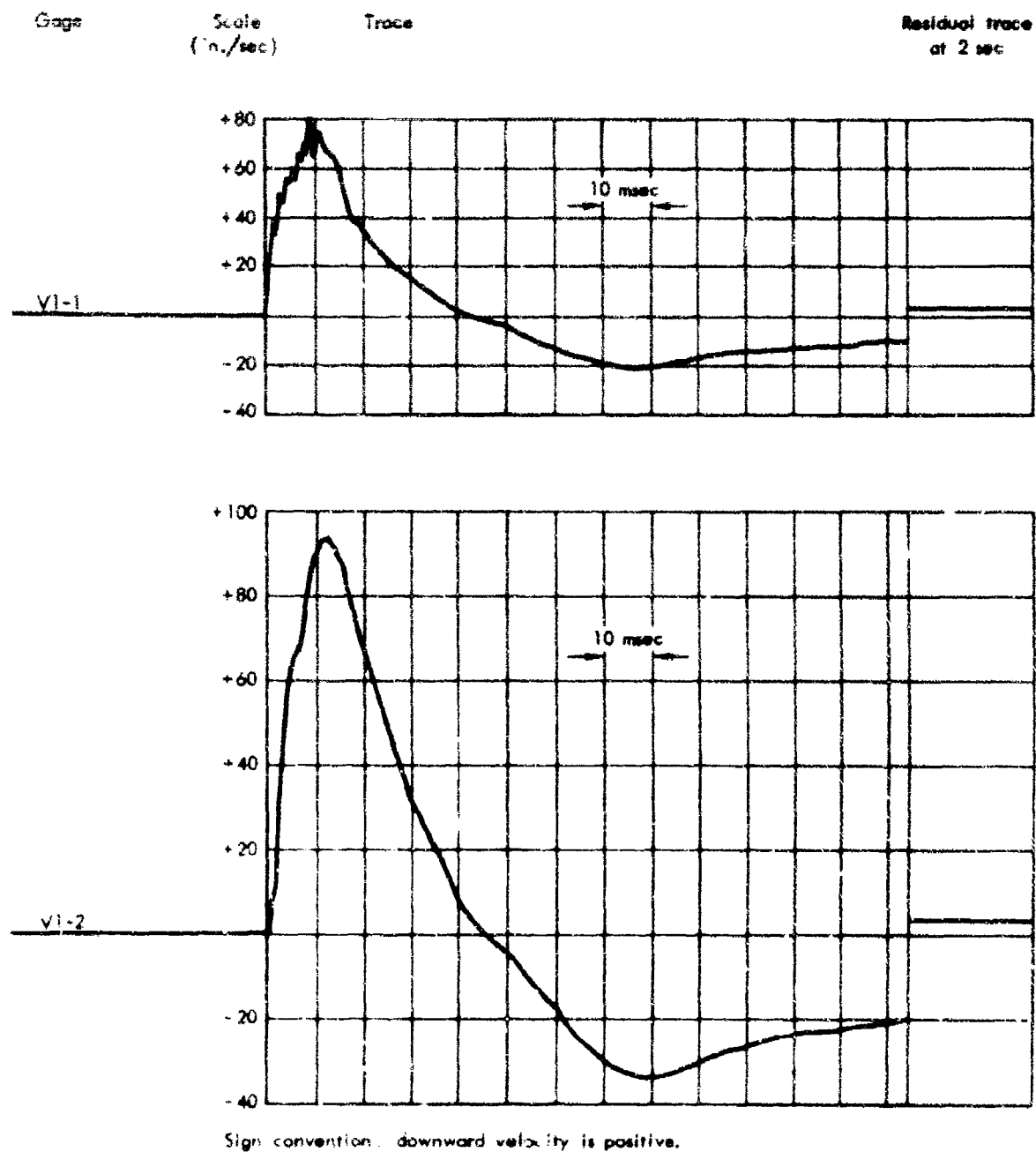


Figure D-9. Velocity data from oscillogram.

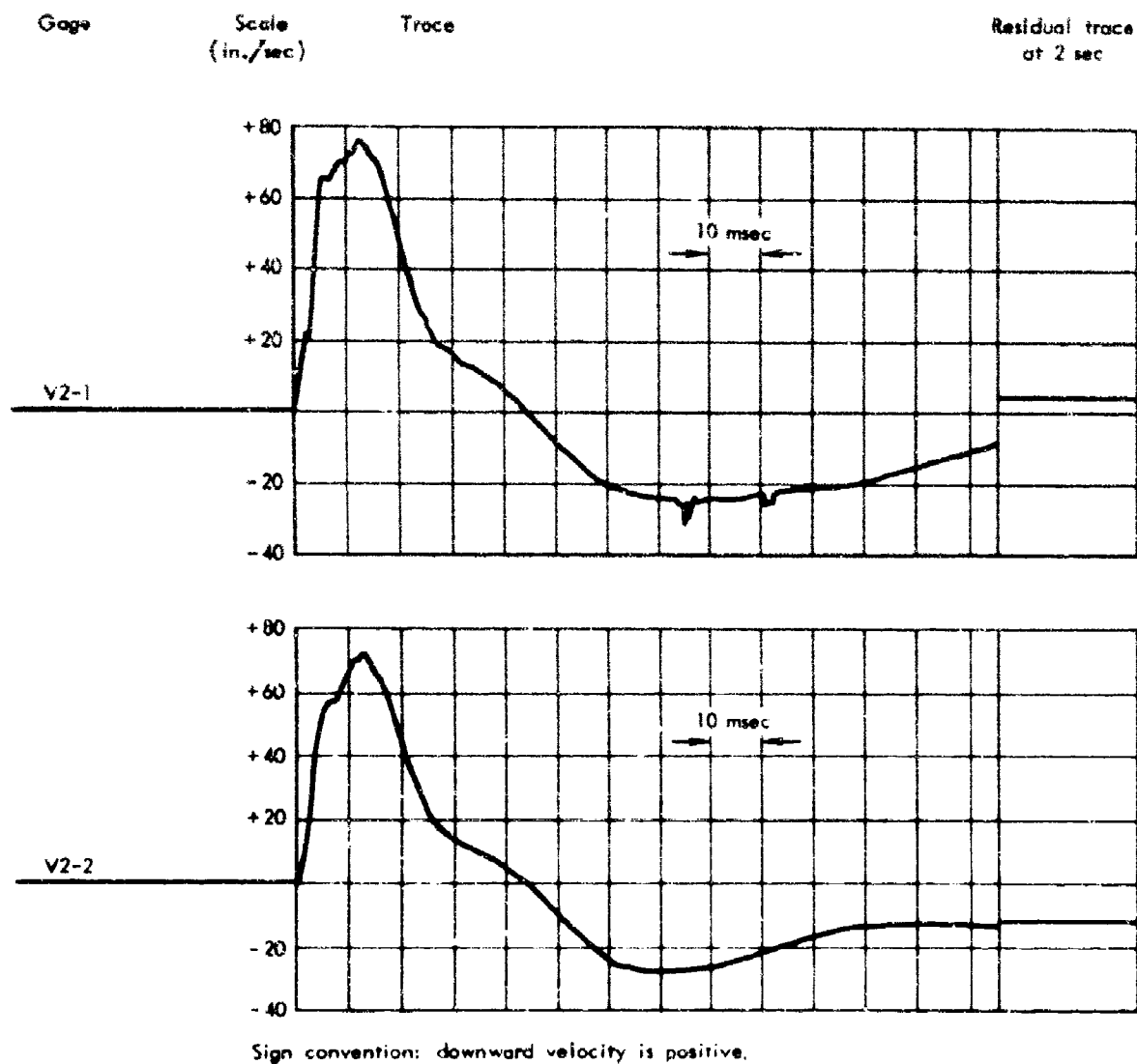


Figure D-10. Velocity data from oscillogram.

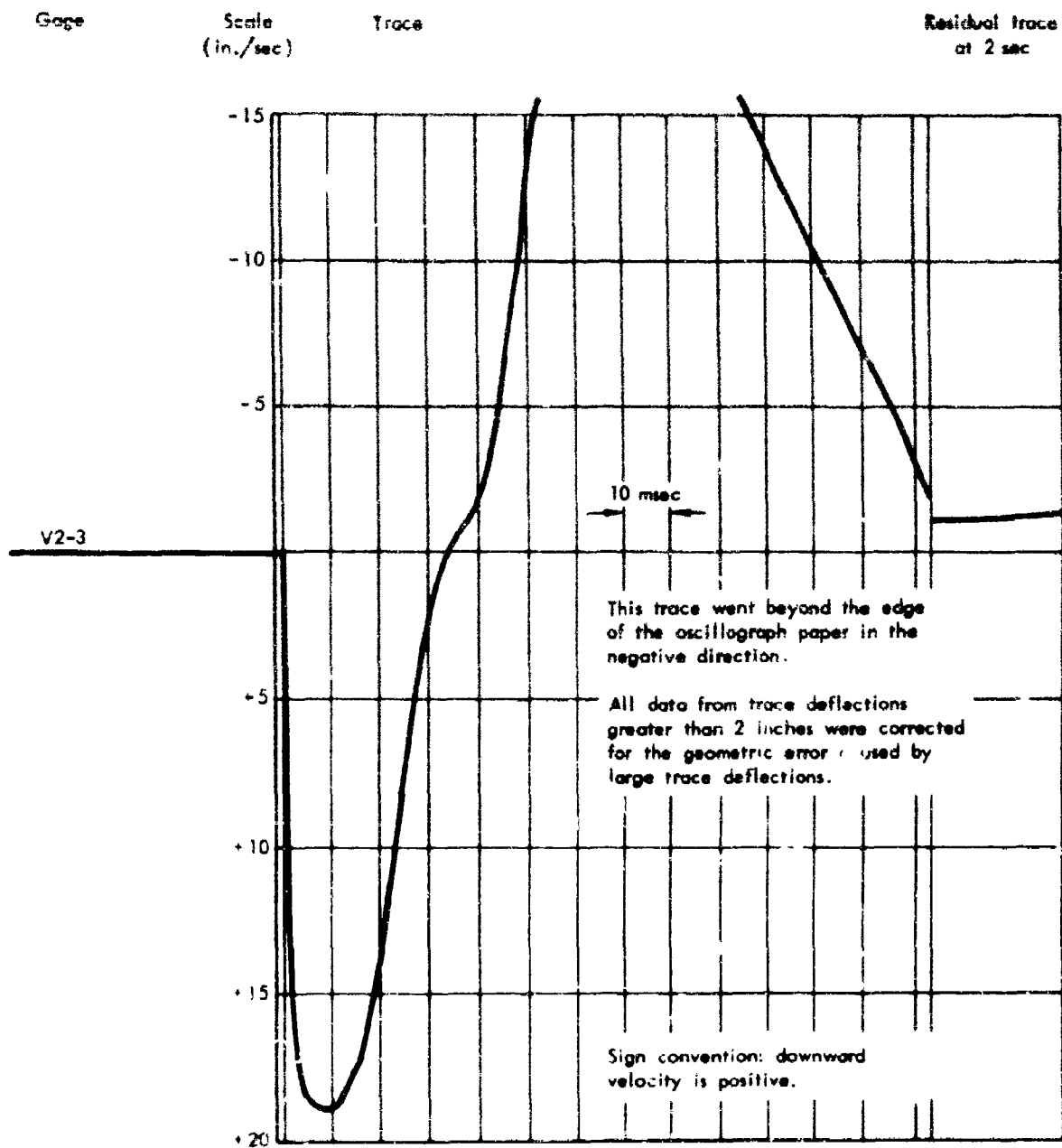


Figure D-11. Velocity data from oscillogram.

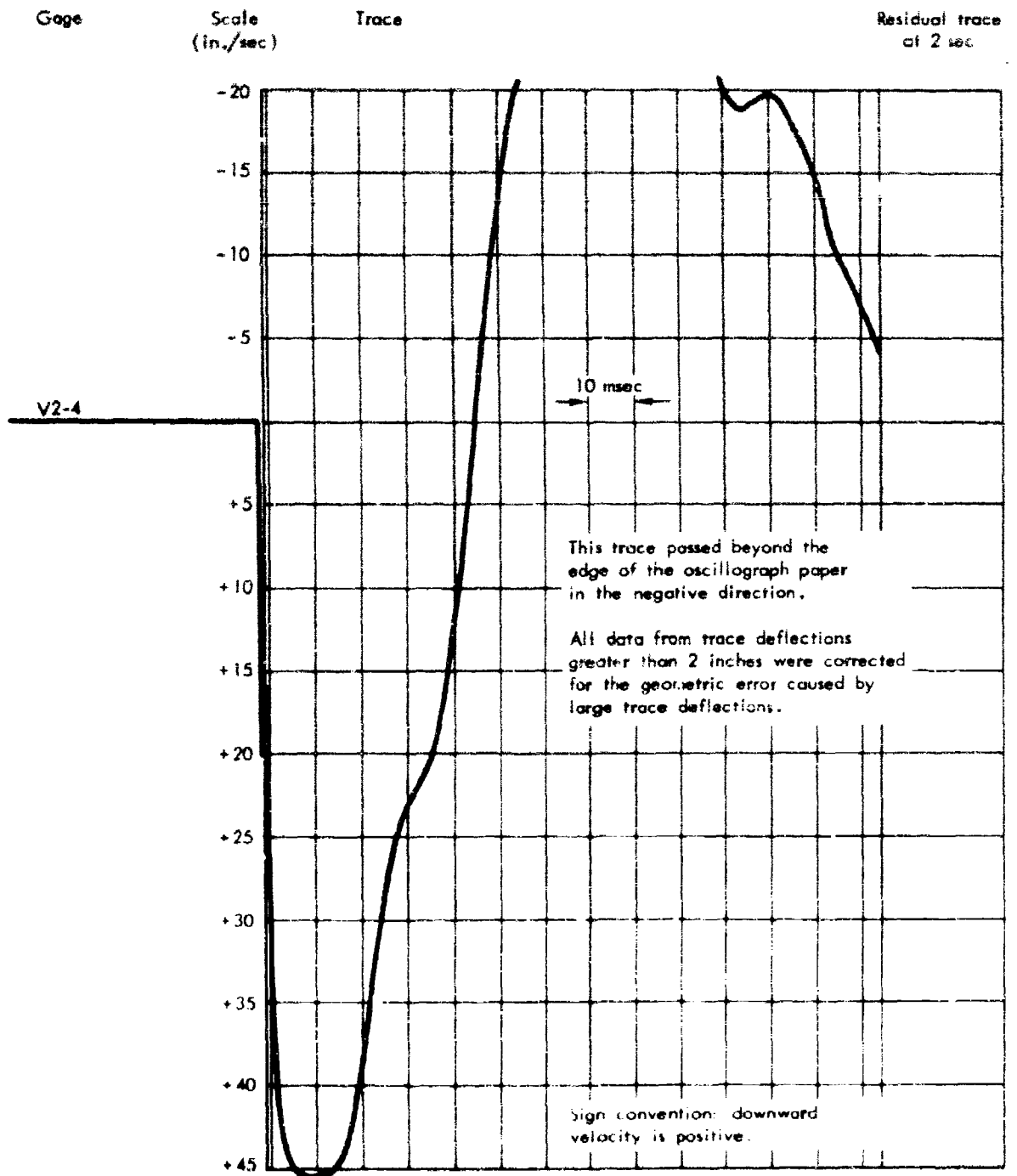
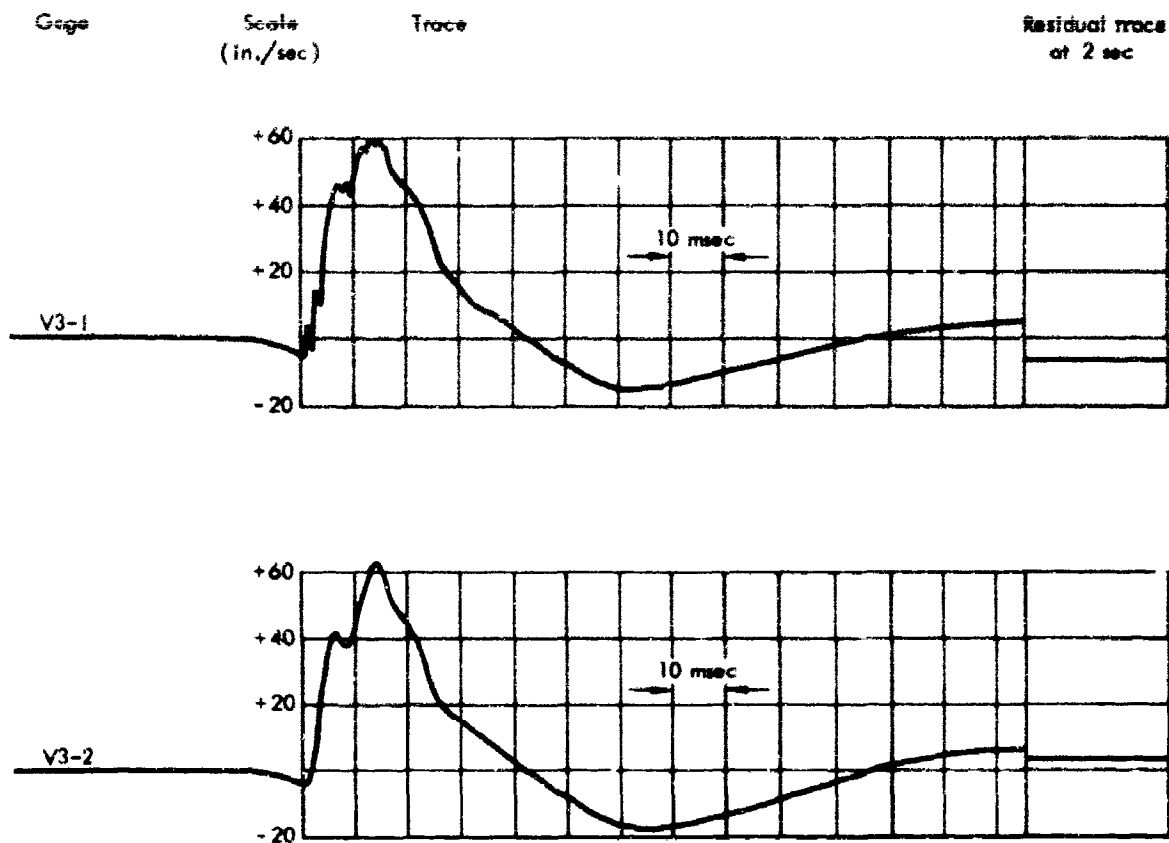


Figure D-12. Velocity data from oscillogram.



Sign convention: downward velocity is positive.

The runout condition existed at these stations causing small initial negative velocities.

Figure D-13. Velocity data from oscillogram.

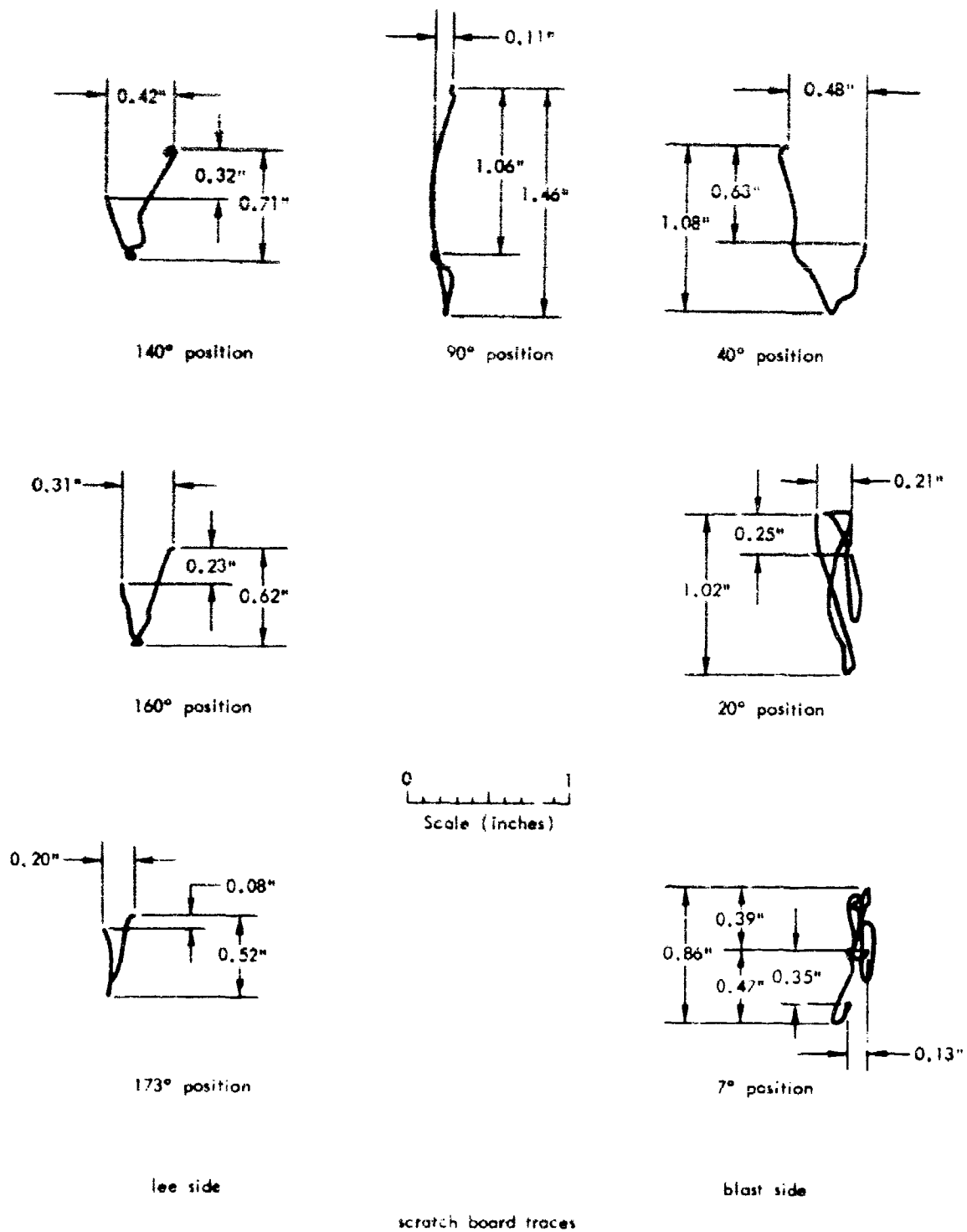


Figure D-14. Deflection of arch CA-1 with respect to the floor.

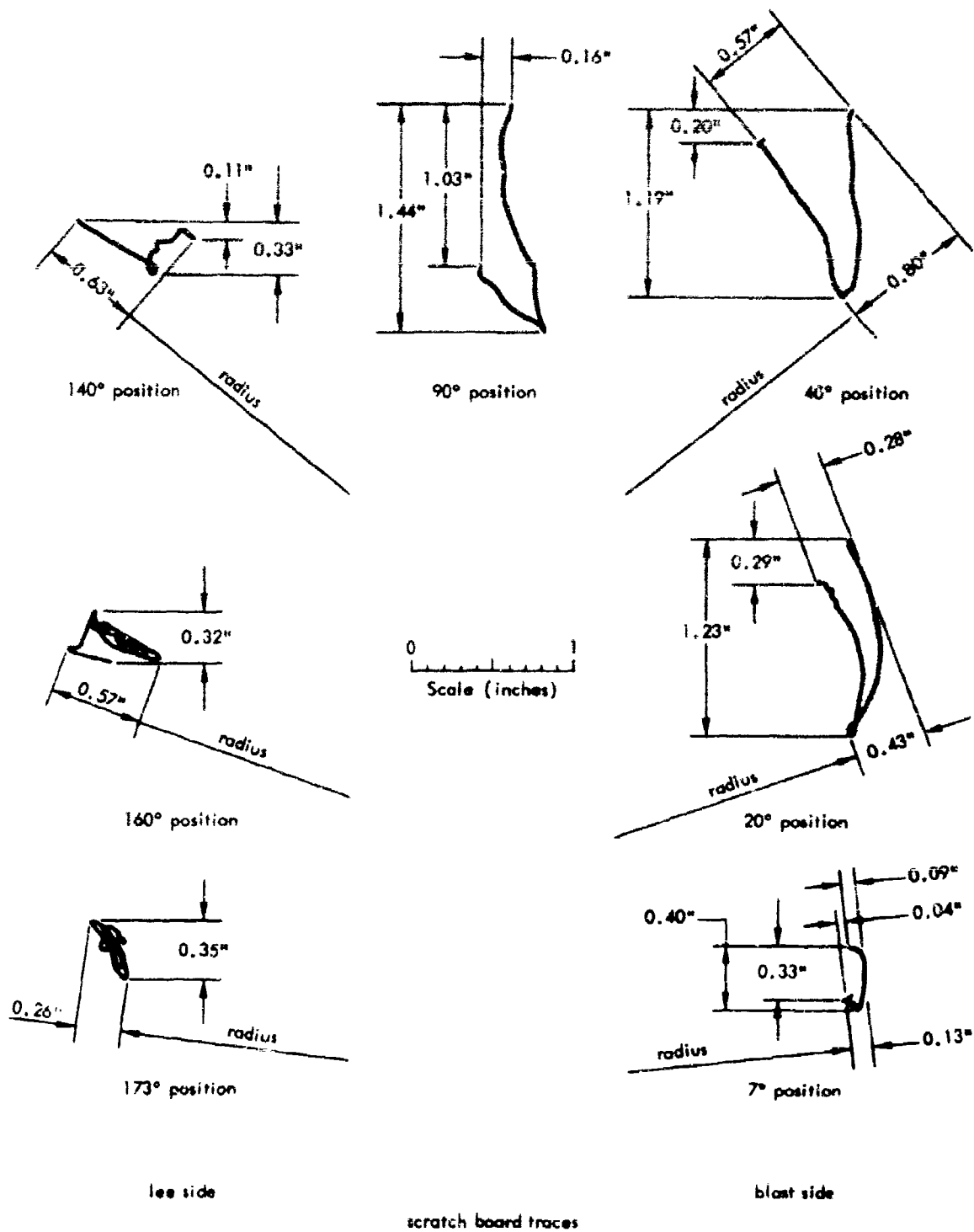


Figure D-15. Deflection of arch CA-1 with respect to the footing.

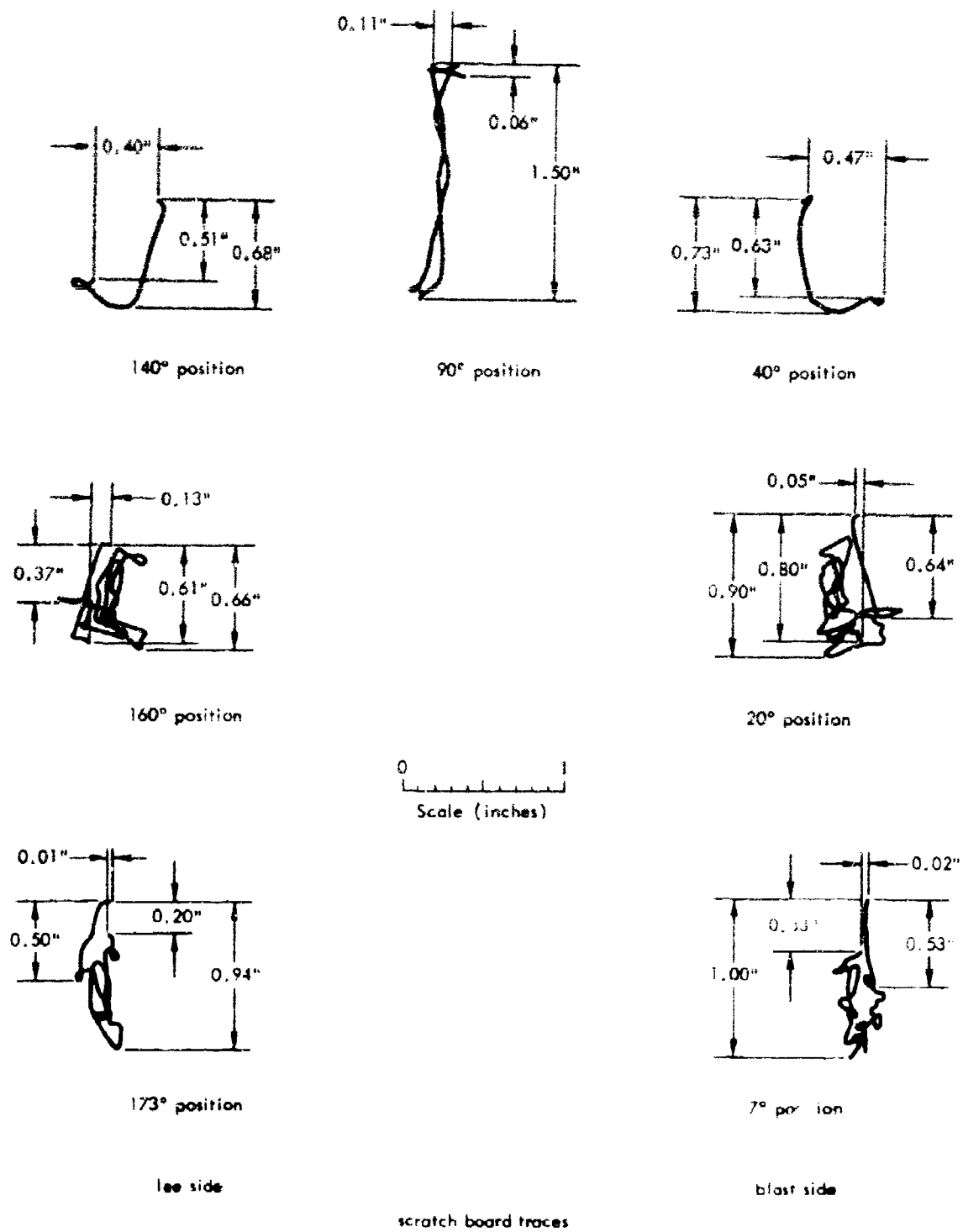


Figure D-16. Deflection of arch CA-2 with respect to the floor.

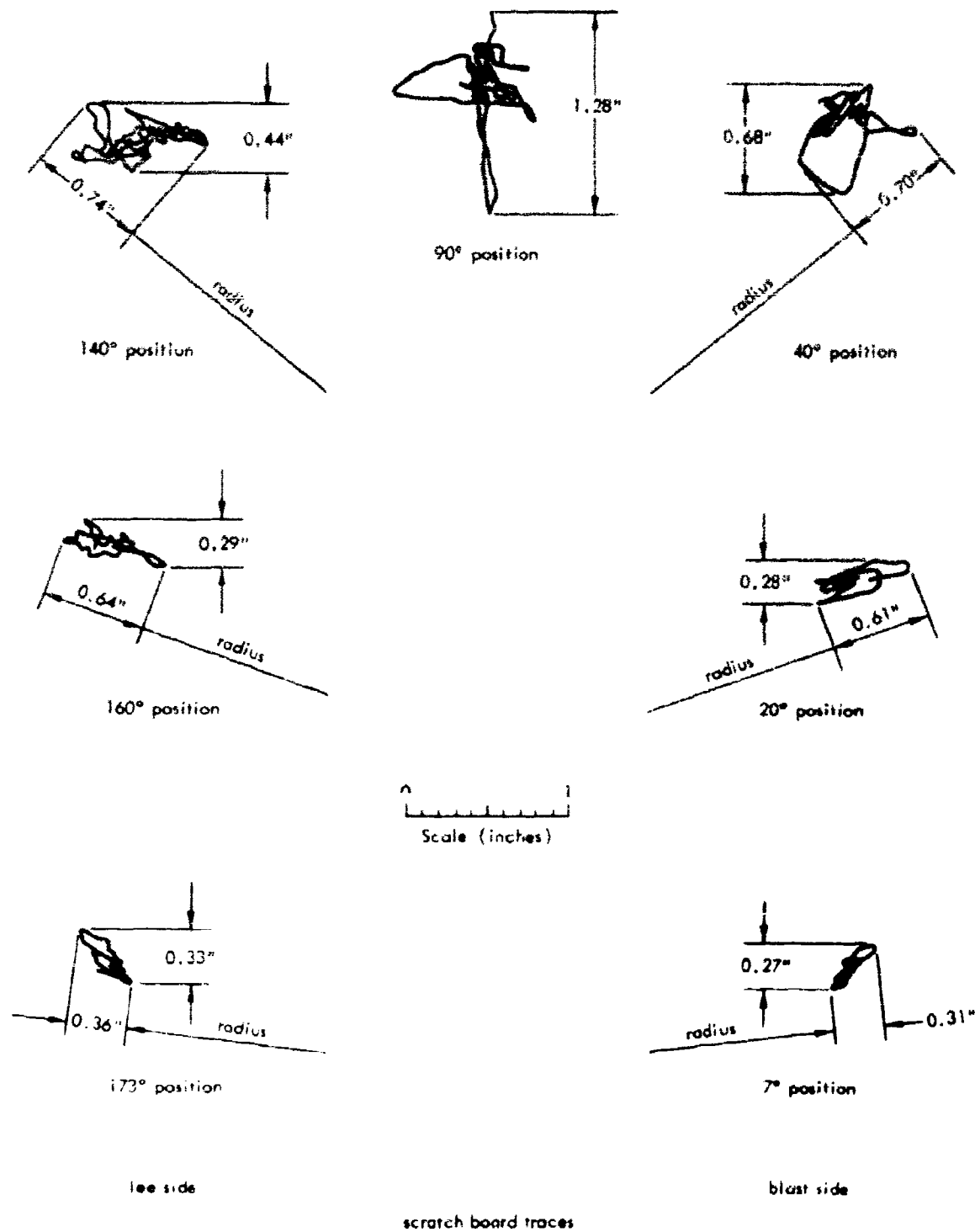


Figure D-17. Deflection of arch CA-2 with respect to the footing.

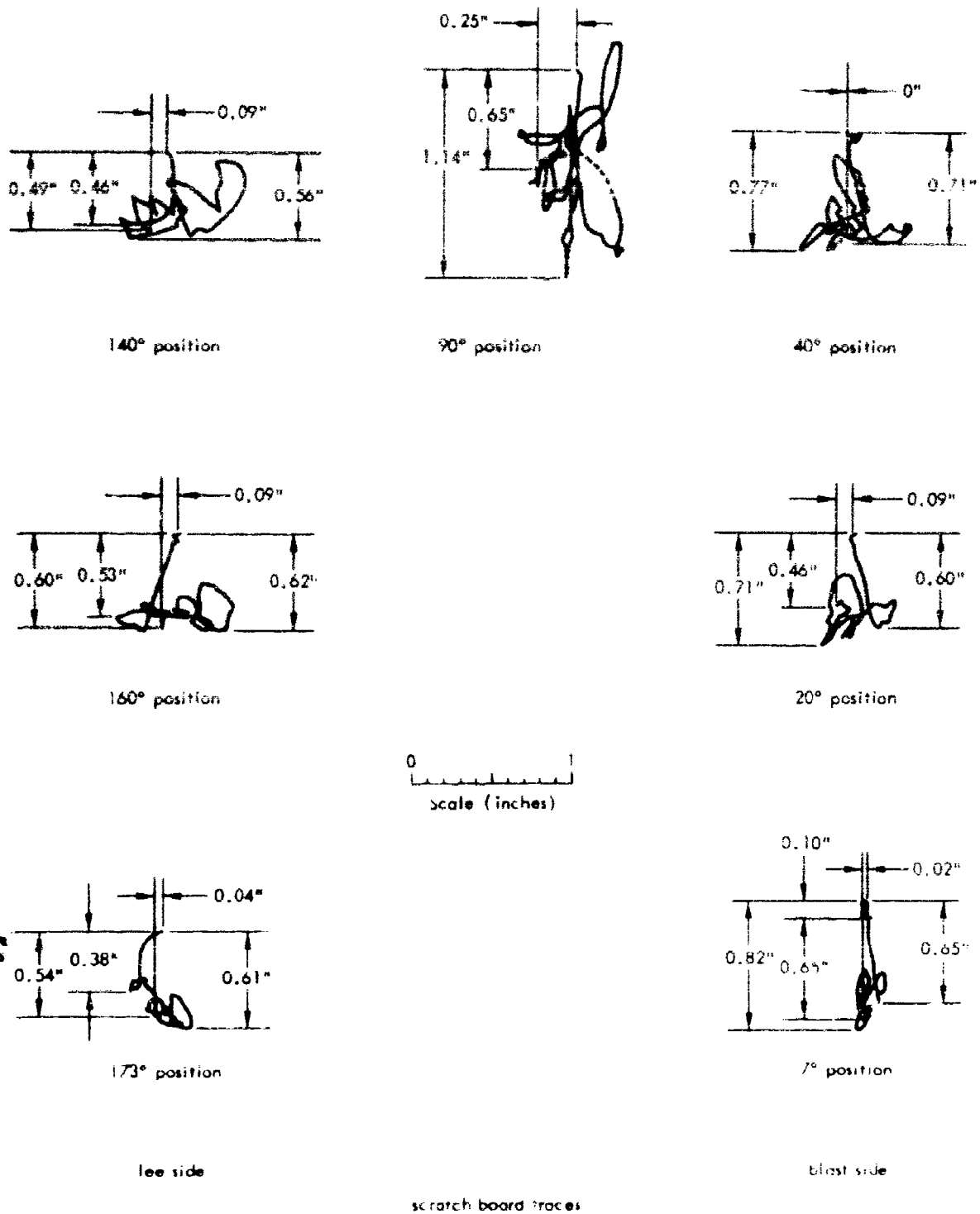


Figure D-18. Deflection of arch CA-3 with respect to the floor.

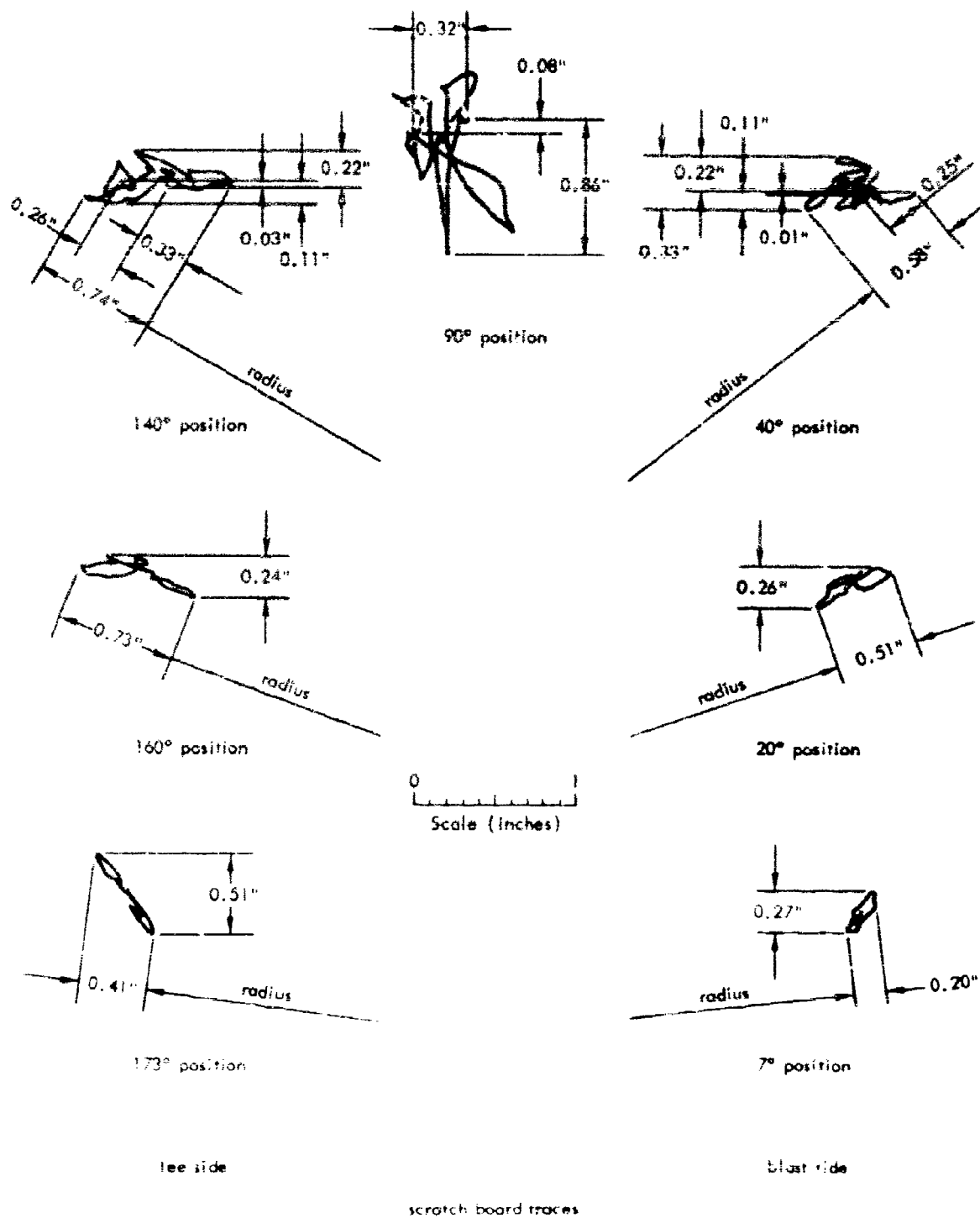
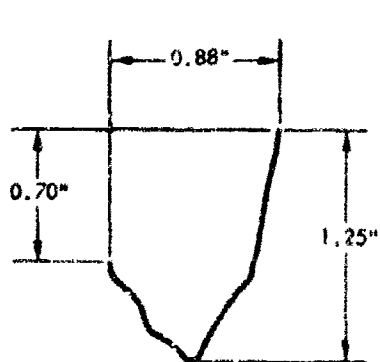
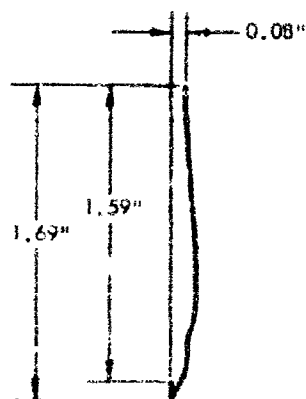


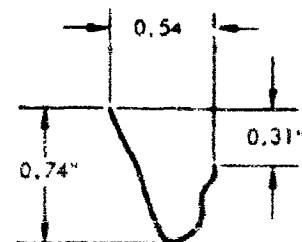
Figure D-19. Deflection of arch CA-3 with respect to the footing.



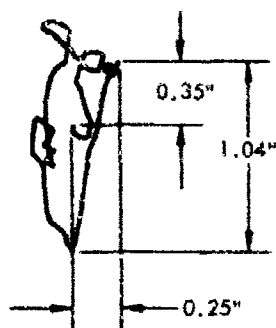
140° position



90° position



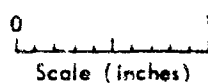
40° position



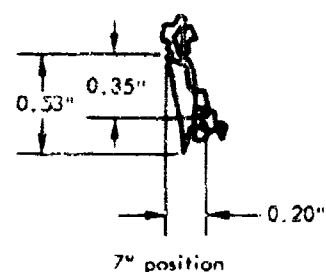
160° position

no record

20° position



no record



7° position

173° position

east side

west side

scratch board traces
facing ground zero

Figure D-20. Deflection of arch CA-4 with respect to the floor.

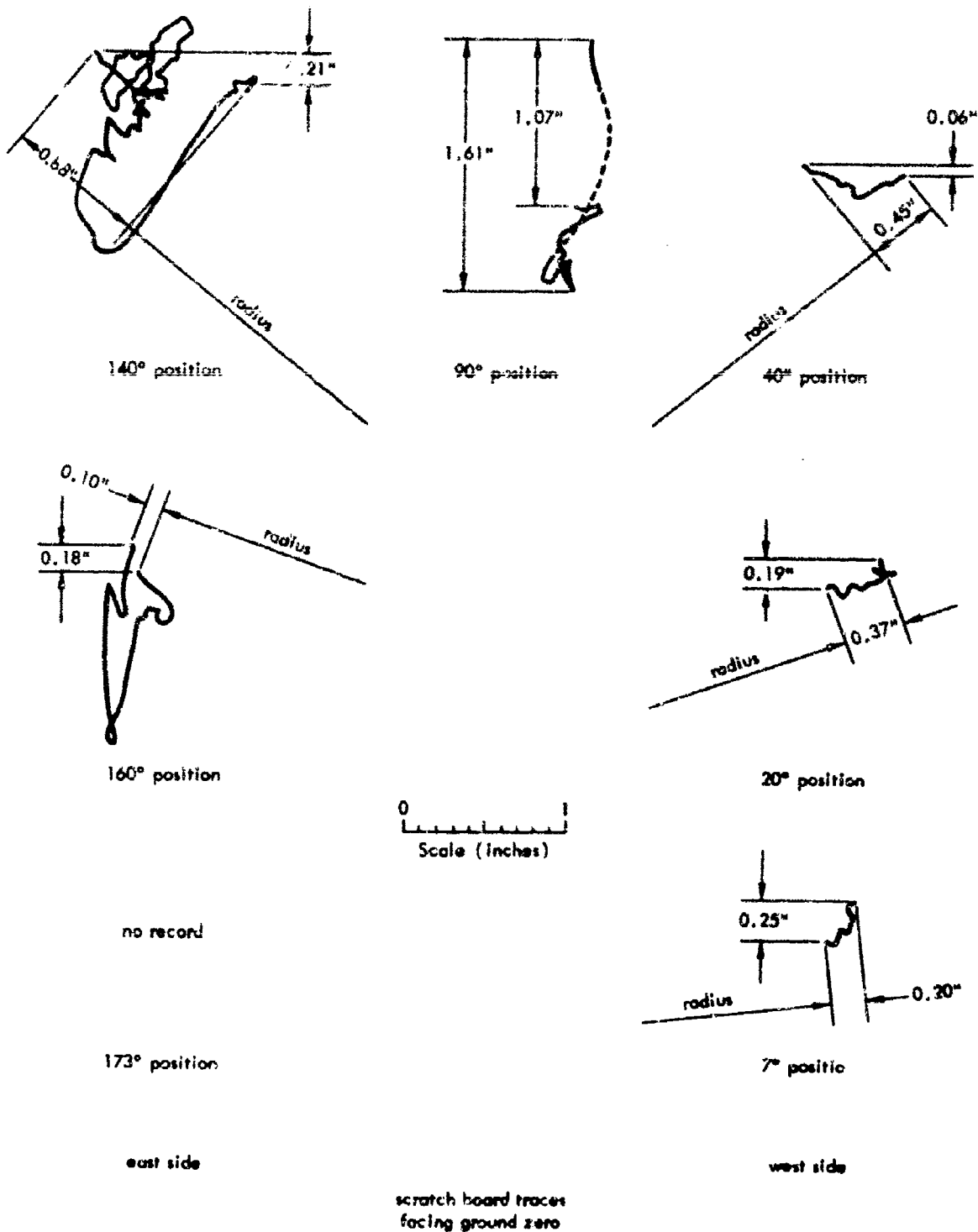


Figure D-21. Deflection of arch CA-4 with respect to the footing.

DISTRIBUTION LIST

SNDL Code	No of Activities	Total Copies	
	1	10	Chief, Bureau of Yards and Docks (Code 42)
23A	1	1	Naval Force Commanders (Korea only)
39B	2	2	Construction Battalions
39C	5	5	Mobile Construction Battalions
39E	3	3	Amphibious Construction Battalions
39F	1	2	Construction Battalion Base Units
A2A	1	1	Chief of Naval Research - Only
A3	2	2	Chief of Naval Operation (OP-07, OP-04)
A5	5	5	Bureaus
B3	2	2	Colleges
E4	1	2	Laboratory ONR (Washington, D. C. only)
E5	1	1	Research Office ONR (Pasadena only)
E16	1	1	Training Device Center
F9	7	7	Station - CNO (Boston; Key West; San Juan; Long Beach; San Diego; Treasure Island; and Rodman, C. Z. only)
F17	7	7	Communication Station (San Juan; Perth; Pearl Harbor; Adak, Alaska; Guam; Stockton; and Cheltenham only)
F41	1	1	Security Station
F42	1	1	Radio Station (Oso only)
F61	2	2	Naval Support Activities (London and Naples only)
F73	2	2	Fleet Activities - BuShips
F77	1	1	Submarine Base (Groton, Conn. only)
F81	2	2	Amphibious Bases
F87	1	1	Receiving Station (Brooklyn only)
H3	7	7	Hospital (Chelsea; St. Albans, Portsmouth, Va.; Beaufort, Great Lakes, San Diego; and Camp Pendleton only)
H6	1	1	Medical Center
J1	2	2	Administration Command and Unit - BuPers (Great Lakes and San Diego only)
J3	1	1	U. S. Fleet Anti-Air Warfare Training Center (Virginia Beach only)
J34	1	1	Station - BuPers (Annapolis, only)
J46	1	1	Personnel Center

DISTRIBUTION LIST (Contd)

SPOT Code	No. of Activities	Total Copies	
J48	1	1	Construction Training Unit
J66	1	1	School Academy
J65	1	1	School CEC Officers
J84	1	1	School Postgraduate
J90	1	1	School Supply Corps
J95	1	1	School War College
J99	1	1	Communication Training Center
L1	11	11	Shipyards
L7	4	4	Laboratory - BuShips (New London; Panama City; Carderock; and Annapolis only)
L26	4	4	Naval Facilities - BuShips (Antigua; Turks Island; Barbados; and Eleuthera only)
M27	4	4	Supply Center
M28	5	5	Supply Depot (except Guantanamo Bay; Subic Bay; and Yokosuka)
M61	2	2	Aviation Supply Office
N1	13	39	BuDocks Divisions
N5	3	9	Construction Battalion Center
N6	6	6	Construction Officer-in-Charge
N7	1	1	Construction Resident Officer-in-Charge
N9	6	12	Public Works Center
N14	1	1	Housing Activity
R9	2	2	Recruit Depots
P10	2	2	Supply Installations (Albany and Borstow only)
R20	1	1	Marine Corps Schools (Quantico)
R64	3	3	Marine Corps Base
P66	1	1	Marine Corps Camp Detachment (Tangan only)
W1A1	6	6	Air Station
W1A2	21	31	Air Station
W1B	7	7	Air Station Auxiliary
W1C	3	3	Air Facility (Phoenix; Naha; or Naples only)
W1D	6	6	Marine Corps Air Station (except Quantico)

DISTRIBUTION LIST (Contd)

SNDL Code	No. of Activities	Total Copies	
W1H	9	9	Station - BuWeps (except Rota)
W7Z	1	1	Missile Center
	1	1	Chief of Engineers, U. S. Army, Attn: ENGCW-E, Washington, D. C. 20315
	1	1	Chief of Engineers, U. S. Army, Attn: ENGMCE-E, Washington, D. C. 20315
	1	1	Headquarters, U. S. Air Force, Directorate of Civil Engineering, Attn: AFCECE-E5, Washington, D. C. 20330
	1	1	Commanding Officer, U. S. Naval Construction Battalion Center, Attn: Material Department, Code 140, Port Hueneme, Calif. 93041
	1	1	Director, Coast & Geodetic Survey, U. S. Department of Commerce, 6001 Executive Boulevard, Rockville, Md. 20852
	1	20	Defense Documentation Center, Building 5, Cameron Station, Alexandria, Va.
	1	1	Director of Defense Research and Engineering, Room 3C-128, The Pentagon, Attn: Technical Library, Washington, D. C. 20301
	1	1	U. S. Bureau of Reclamation, Department of Interior, Attn: Mr. T. W. Marmel, Washington, D. C. 20240
	1	1	Facilities Officer, Code 108, Office of Naval Research, Washington, D. C.
	1	1	Commander Naval Beach Group Two, Attn: Project Officer, U. S. Naval Amphibious Base, Little Creek, Norfolk, Va.
	1	1	U. S. Army Engineer Research and Development Laboratories, Attn: STINFO Branch, Fort Belvoir, Va.
	1	1	Air Force Weapons Laboratory, Kirtland Air Force Base, Albuquerque, N. M., Attn: Code WLRC
	1	1	Library, Department of Meteorology and Oceanography, U. S. Naval Postgraduate School, Monterey, Calif.
	1	1	Library of Congress, Washington, D. C.
	1	1	LCDR Charles W. Gelick, Jr., CEC, USN, CNABATRA Public Works, NAS Pensacola, Fla. 32508
	1	1	CDR J. F. Dobson, CEC, USN, Office of Civil Defense, Dept. of the Army, Washington, D. C.

DISTRIBUTION LIST (Contd)

No. of Activities	Total Copies	
1	1	Officer in Charge, CECOS, Attn: NDCE Course, Port Hueneme, Calif.
1	1	Defense Intelligence Agency, Attn: DIAAP-1K2, Washington, D. C. 20301
1	1	Space Systems Division, Los Angeles Air Force Station, Attn: SSSD, Los Angeles, Calif.
1	1	Commanding Officer, U. S. Army Engineer Research and Development Laboratories, Attn: Technical Documents Center, Fort Belvoir, Va. 22060
1	1	Director, U. S. Army Engineer Waterways Experiment Station, Attn: Mr. G. L. Arbutnot, Jr., P. O. Box 631, Vicksburg, Miss.
1	1	U. S. Army Nuclear Defense Laboratory, Attn: Librarian, Edgewood Arsenal, Md. 21010
1	5	Director, Defense Atomic Support Agency, Washington, D. C.
1	15	Defense Atomic Support Agency, Attn: Mr. J. R. Kelso, Blast and Shock Division - for TTCP, Washington, D. C.
1	1	U. S. Atomic Energy Commission, Division of Technical Information, P. O. Box 62, Oak Ridge, Tenn. 37831
1	1	Chief, Civil Effects Branch, Division of Biology and Medicine, U. S. Atomic Energy Commission, Washington, D. C.
1	1	Disaster Recovery Training Officer, U. S. Naval Construction Battalion Center, Code 700, Davisville, R. I.
1	1	Commanding Officer, Ballistics Research Laboratories, Attn: AMXBR-TB, Mr. William J. Taylor, Aberdeen Proving Ground, Md.
1	1	CDR P. A. Phelps, CEC, USN, U. S. Naval MCB Eight, C/o FPO, New York
1	1	CAPT W. M. McLellan, CEC, USN, Ret., 468 1st Street, Albany, N. Y.
1	1	CDR J. C. LeDoux, Bureau of Yards and Docks, Department of the Navy, Washington, D. C.
1	1	LT Edward S. Ferry, U. S. Naval Reserve Officers Training, Corps Unit, University of Illinois, Urbana, Ill.
1	1	CAPT L. N. Saunders, CEC, USN, Code C10, U. S. Naval Construction Battalion Center, Port Hueneme, Calif. 93041
1	1	CDR Edward M. Saunders, CEC, USN, Office of Naval Material (MAT 311), Requirements Analysis Branch, Washington, D. C.
1	1	CDR W. A. Walls, Director, Disaster Control Division, Code 30.700, Bureau of Yards and Docks, Washington, D. C.
1	1	LT COL C. D. Daniel, USA, Nuclear Branch Chief, Defense Atomic Support Agency, Washington, D. C.
1	1	CAPT W. J. Christensen, CEC, USN, Commanding Officer and Director, U. S. Naval Civil Engineering Laboratory, Port Hueneme, Calif. 93041

DISTRIBUTION LIST (Contd)

No of Activities	Total Copies	
1	1	CDR J. D. Andrews, CEC, USN, Executive Officer, U. S. Naval Civil Engineering Laboratory, Port Hueneme, Calif. 93041
1	1	CDR R. C. Vance, CEC, USN, Logistics Director, U. S. Naval Civil Engineering Laboratory, Port Hueneme, Calif. 93041
1	1	LCDR O. L. Dixon, CEC, USN, Assistant Officer-in-Charge, U. S. Naval School, CEC Officers, Port Hueneme, Calif. 93041
1	1	CDR C. Curione, CEC, USN, Resident Officer-in-Charge-of-Construction, Long Beach Area, P. O. Box XX, Seal Beach, Calif. 90740
1	1	LCDR George M. Gans, CEC, USN, U. S. Naval School, CEC Officers, Port Hueneme, Calif. 93041
1	1	CDR C. R. Whipple, CEC, USN, U. S. Navy Public Works Center, Box 6, FPO San Francisco, Calif. 96650
1	1	LCDR T. Yoshihara, CEC, USN, DOICC, Southeast Asia, APO 143, San Francisco
1	1	LT L. K. Donovan, CEC, USN, Disaster Control Officer, U. S. Naval Communication Station, Honolulu, FPO, San Francisco, Calif. 96613
1	1	LCDR Walter J. Eager, Jr., CEC, USN, Positive Ion Accelerator Branch, AFRLI-NNMC, Bethesda, Md.
1	1	CDR W. J. Francy, CEC, USN, Engineering Department, U. S. Naval Academy, Annapolis, Md. 21402
1	1	LCDR I. D. Crowley, Jr., Blast and Shock Division, Defense Atomic Support Agency, Washington, D. C.
1	1	LCDR W. H. Bannister, CEC, USN, Field Command, Defense Support Agency, Sandia Base, Albuquerque, N. Mex.
1	1	Major Robert E. Crawford, Air Force Weapons Laboratory (WLDC), Kirtland Air Force Base, N. Mex.
1	1	CDR Allen F. Dill, CEC, USNR, Public Works Officer, Headquarters Support Activity, Taipei, Box 25, APO, San Francisco, Calif. 96263
1	1	Mr. Neal FitzSimons, Director, Engineering Development Division, Office of Civil Defense, Department of Defense, Washington, D. C.
1	1	Mr. Benjamin C. Taylor, Special Assistant Technical Liaison, Room 1C529, Pentagon, Office of Civil Defense, Department of Army, Washington, D. C.
1	1	Mr. Charles M. Eisenhower, Radiation Physics Laboratory, National Bureau of Standards, Washington, D. C.
1	1	Dr. James O. Buchanan, Director, Shelter Research, Office of Civil Defense, Department of Defense, Washington, D. C. 20310
1	1	Mr. John A. Auxier, Oak Ridge National Laboratory, Oak Ridge, Tenn
1	1	Dr. William E. Kroger, Head, Nucleonics Division, U. S. Naval Radiological Defense Laboratory, San Francisco, Calif

DISTRIBUTION LIST (Contd)

No. of Activities	Total Copies	
1	1	Mr. Richard D. Cavanaugh, Barry Controls, Inc., 700 Pleasant Street, Watertown 72, Mass.
1	1	Mr. Kenneth Kaplan, URS Corporation, 1811 Trousdale Drive, Burlingame, Calif.
1	1	Mr. Walter D. Gunther, Government Consulting, The Mitre Corporation, P. O. Box 205, Lexington, Mass.
1	1	Mr. Lyndon Welch, Eberle M. Smith Associates, Inc., 153 East Elizabeth Street, Detroit 1, Mich.
1	1	Dr. Mevin P. White, Head, Department of Civil Engineering, University of Massachusetts, Amherst, Mass.
1	1	Dr. Robert J. Hansen, Department of Civil & Sanitary Engineering, Massachusetts Institute of Technology, Cambridge 39, Mass.
1	1	Mr. Luke J. Vortman, Division 3232, Sandia Corporation, Sandia Base, Albuquerque, N. Mex.
1	1	Dr. Eric T. Clarke, Vice President for Research and Development, Technical Operations, Inc., Burlington, Mass.
1	1	Dr. A. B. Chilton, Associate Professor of Civil and Nuclear Engineering, 207 Nuclear Engineering Laboratory, University of Illinois, Urbana, Ill.
1	1	Mrs. Shea Valley, CRTE, A. F. Cambridge Research Laboratories, L. G. Hanscom Field, Bedford, Mass. 01731
1	1	Dr. John T. Hanley, Associate Professor Of Civil Engineering, University of Minnesota, Minneapolis, Minn.
1	1	Professor Joseph Silverman, Department of Chemical Engineering, University of Maryland, College Park, Md.
1	1	Dr. F. T. Mavis, Dean and Professor, Dept. of Mechanical Engineering, University of Maryland, College Park, Md. 20742
1	1	Professor Mater L. P. Go, Professor of Civil Engineering, Department of Civil Engineering, University of Hawaii, Honolulu, Hawaii 96822
1	1	Dr. James P. Renualdi, Professor, Research in Structural Dynamics, Carnegie Institute of Technology, Pittsburg, Pa.
1	1	Dr. Aleksandar Sedmak Vesić, Professor of Civil Engineering, Duke University, Durham, N. C.
1	1	Mr. C. C. Mow, The Rand Corporation, 1700 Main Street, Santa Monica, Calif.
1	1	Dr. William L. White, Director, Civil Defense Technical Office, Stanford Research Institute, Menlo Park, Calif.
1	1	Dr. C. V. Chalapati, Assistant Professor of Engineering, California State College at Los Angeles, Los Angeles, Calif. 90032

DISTRIBUTION LIST (Contd)

No. of Activities	Total Copies	
1	1	Mr. George N. Sisson, Office of Civil Defense, Department of Defense, Washington, D. C.
1	1	Mr. F. J. Tomanini, A & E Services Division, Office of Civil Defense, Department of Defense, Washington, D. C.
1	1	Mr. Everett P. Blizzard, Director, Neutron Physics Division, Oak Ridge National Laboratory, P. O. Box X, Oak Ridge, Tenn.
1	1	Mr. William R. Perret, Sandia Laboratory, Division 5232, Sandia Corporation, Albuquerque, N. Mex.
1	1	Mr. Richard Park, Technical Director, Advisory Committee on Civil Defense, National Academy of Sciences, 2101 Constitution Avenue, N. W., Washington, D. C. 20418
1	1	Dr. E. E. Mashev, Defense Research Board, Office of Director of Atomic Research, Department of National Defense, Ottawa, Canada
1	1	Dr. Nicholas Perrone, Office of Naval Research, Code 439, Department of the Navy, Washington, D. C.
1	1	Mr. J. G. Jackson, Jr., Chief, Impulse Loads Section, Soil Dynamics Branch, U. S. Army Engineer Waterways Experiment Station, Vicksburg, Miss.
1	1	Library, Protective Structures Development Center, Building 2591, Fort Belvoir, Va. 22060
1	1	Librarian, National Resource Evaluation Center, Office of Emergency Planning, Room 011, Executive Office Building, Washington, D. C. 20504
1	1	Mr. G. H. Albright, Head, Department of Architectural Engineering, 101 Engineering "A" Building, The Pennsylvania State University, University Park, Pa.
1	1	Professor J. Neils Thompson, Education and Research, Civil Engineering Department, University of Texas, Austin, Tex.
1	1	Mr. Fred M. Sauer, Physics Department, Stanford Research Institute, Menlo Park, Calif.
1	1	Dr. Theodore Schiffman, Illinois Institute of Technology Research Institute, 10 W. 35th Street, Chicago, Ill. 60616
1	1	Dr. Robert M. Whitman, Room 1 346, Massachusetts Institute of Technology, Cambridge, Mass. 02139
1	1	Dr. Lewis V. Spencer, Physics Department, Ottawa University, Ottawa, Kansas
1	1	Mr. Erwin E. Shorowitz, Protective Construction, GSA Building, 19th and F Streets, N. W., Washington, D. C. 20405
1	1	Mr. Wendel Weber, Director of Research & Development, Public Security Building, State Office Building Campus, Albany, N. Y. 12226
1	1	Dr. H. J. Rose, The Plasma Corporation, 1100 Main Street, Santa Monica, Calif. 90401
1	1	Professor Ray J. F. ... Advisor, Nuclear Defense Engineering Courses, The George Washington University, Washington, D. C. 20006

DISTRIBUTION LIST (Contd)

No. of Activities	Total Copies	
1	1	Chief, Engineering Division, U. S. Army Engineer District, Omaha, Corps of Engineers, 6012 U. S. Post Office and Court House, Omaha, Neb. 68102
1	1	Dr. S. H. Levine, Head, Nuclear Sciences Laboratory, Northrop Space Laboratories, 3401 West Broadway, Hawthorne, Calif. 90250
1	1	Prof. Elmira Smyrl, School of Architecture, Montana State College, Bozeman, Montana
1	1	Chief Superintendent, Suffield Experimental Station, Reiston, Alberta, Canada
1	1	Library, Civil Engineering Dept., University of Hawaii, Honolulu
1	1	Library, Dept. of Meteorology and Oceanography, U. S. Naval Postgraduate School, Monterey, Calif.
1	1	Library, Public Documents Dept., Dulce University, Durham, N. C.
1	1	Prof. Carl H. Koonov, Civil Engineering Dept., Worcester Polytechnic Institute, Worcester, Mass.
1	1	Mr. Frank Keptonak, U. S. Navy Underwater Sound Laboratory, New London, Conn.
1	1	Dr. Armas Luupa, The Rand Corp; 1700 Main St., Santa Monica, Calif.
1	1	Commander, U. S. Naval Weapons Laboratory, Attn: Code TEV, Dahlgren, Va.